von Karman Institute for Fluid Dynamics

Lecture Series 2025-01

# MEASUREMENT, MODELLING AND SIMULATIONS TECHNIQUES FOR NOVEL AIRCRAFT ARCHITECTURES

November 4-6, 2024

## *PROPELLER NOISE: BODY FORCE MODELS ON OCTREE-CARTESIAN GRIDS AND FRPM-BASED BROADBAND PART*

R. Ewert & A. Franco
Institute of Aerodynamics and Flow Technology, Department of Technical Acoustics,
German Aerospace Center (DLR), Germany

# 1 Introduction

The last decade has seen an increased interest towards sustainable aircraft design concepts, motivated by the need to reduce the environmental impact of aviation. Future aircraft sustainability requirements were translated into an increased number of European and US projects, establishing challenging milestones to be achieved in terms of energy consumption reduction, diminishment in pollutant emissions and perceived noise abatement. To address these goals, aircraft manufacturers are re-evaluating available propulsion technologies and re-designing aircrafts by means of unconventional propulsion integration configurations. Among the most promising new configurations to achieve this goal are distributed electric propulsion systems and buried or semi-buried engine integrations on the airframe. Distributed propulsion concepts would include single or dual fan engines configurations with Boundary Layer Ingestion integrated on blended wing body aircrafts, engines configurations with a common core and multi-fans or propulsors, and more conventional aircraft design with wing-distributed engines arrangements. Buried or semi-buried engines concepts have been proposed for hybrid wing body or blended wing body aircrafts designs. Review contributions on distributed propulsion by Gohardani (Gohardani et al., 2011) and hybrid electric propulsion concepts by Wall and Meyer (Wall and Meyer, 2017) offer a good overview on the state of the art on sustainable aviation technologies.

Regardless of the configuration chosen, a requirement to fulfill for future aircraft concepts is a perceived reduction of between 50% and 65% in noise emissions by 2050, based on current technology development. Being new propulsion configurations one of the key aspects in achieving a more sustainable aircraft design, the demanding cut in noise pollution is driving aeroacoustics rotor noise research to provide manufacturers with new design methods, able to predict noise emissions with enough accuracy to be reliably used for new proposed aircrafts noise estimation. The existing propulsion system's components of these new configurations have been studied extensively in the past decades, and their tonal noise sources mechanisms are well understood. The origin of aerodynamic sound generated from a rotor in a subsonic flow has been identified to be originated from both the aerodynamic load on the blades and from the unsteady volume displacement by the blade movement in the flow.

The earliest work of Gutin (Gutin, 1948) provides the reference to estimate noise propagation for isolated rotors, treated as rigid devices rotating in a steady uniform flow. However, modern existing rotors during real flight conditions (e.g. forward and transitional flight) show a considerable deviation from the results obtained under such assumptions, due to the highly non-uniform flow and the consequent fluctuating loads during advancement and retreat of the blades. The results provided by Gutin's model show in general an accurate prediction of the fundamental tone, but the predicted higher harmonics differ substantially, due to the missing information about fluctuating loads under non-uniform flows. Lowson derived a more general analytical expression than Gutin's to evaluate the sound field of a point force singularity in motion, including retarded blade locations and numerical derivatives in the time domain (Lowson and Lighthill, 1965), showing that the motion of a fluctuating force will contribute with essentially two components to the sound field generated. One component, dependent on the time rate of change of the force, has a dipole radiation pattern, while the other component is dependent on the acceleration

of the system in which the force is acting. One of the widely used models in present times is the one introduced by Hanson (Hanson, 1980), who improved Gutin's model by including also the effects of blade thickness, forward flight, and blade sweep, maintaining the original formulation in the frequency domain. This model represents the state of the art of analytical prediction models for rotor noise.

All the aforementioned models can predict with enough accuracy far-field rotor noise emissions, but near-field noise prediction has revealed to be a complicated task, due to numerous physical phenomena influencing the noise generated. Nevertheless, noise estimation in the vicinity of the blades can be attempted with appropriate physical-based simplifications. In Ref. (Peake and Crighton, 1991) a near-field noise prediction model was presented, with an expression to evaluate the far-field thickness and steady loading noise. This model extends the radiation integrals by an asymptotic analysis for large number of blades. The formulae for the harmonic components of the near-field acoustic pressure show how subsonic blades noise generation results mainly dependent by blade tip aerodynamics, while for supersonic motion, the Ffowcs Williams & Hawkings sonic condition needs to be satisfied by the noise sources to obtain a good estimate.

In parallel to theoretical based models, empirical models to predict rotor noise have also been developed since the beginning of propeller driven aircraft usage. The aim of these methods is to simplify the prediction of far-field and near-field noise while retaining an adequate level of accuracy for aircraft certifications procedures. Various models have been developed until recently and are kept as part of aircraft certification procedures of related agencies such as European Union Aviation Safety Agency and Federal Aviation Administration. All these models are based on approximate equations involving, among the most important parameters, rotor power, RPM, number of blades, flight speed, and rotor diameter. Among the earliest empirical methods based on approximated equations is the one introduced by Smith (Smith, 1981), who proposed an empirical model developed using a regression test analysis from A-weighted sound level data obtained during certification tests of single and twin engines airplanes. In his contribution, Smith included, in addition to the aforementioned model parameters, also blade tip twist and blade thickness, accounting respectively for more correct spanwise loading distributions and thickness noise estimation, the latter being particularly important for high tip speed propellers. Subsequently, purely empirical models are derived or inspired on Smith's approach, which served as the initial reference for empirical models to be used in certification procedures.

Other possible rotor noise estimation approaches combine theoretical simplified results with empirical observations, producing semi-empirical models that serve certifications purposes as well. One such example is the model proposed by Lewy (Lewy, 2010) to predict tone noise for Contra Rotating Open Rotors. The model is intended for takeoff and approach conditions characterized by a low advancing Mach number, ensuring subsonic flow conditions at the blades tip. To represent the directivity of a tone, a Bessel function is used, and the overall sound pressure levels are approximated by means of a parabolic pattern.

Generally, each of the above mentioned models is able to generate a fairly accurate prediction of the fundamental tone, and provide an estimate of the near-field noise emissions in design-point conditions, but they lack the capability of capturing the correct sound field generated by non-uniform inflow conditions.

Furthermore, even in design-point conditions, an accurate prediction of the higher harmonics is seen as a complex task to be addressed by either analytical or empirical based calculations, and in particular empirical models would have a limited applicability only to existing rotors. In addition to that, future new propulsion configurations would introduce, besides the rotor self-noise contributions, a new type of noise source, arising from the interaction of propulsors with aircraft components. This type of noise source mechanism can be categorized as installation noise, and it is very particular with respect to the propulsion integration configuration chosen.

Earliest research on installation noise included investigations on the interaction of a propeller installed on a wing. In Ref. (Tanna et al., 1981), experiments on such configurations were conducted to investigate and quantify the difference in measured noise with respect to an isolated or uninstalled propeller operating under zero inflow angle conditions. The three main installation effects identified and analyzed were the influence of a non-zero inflow angle with respect to the flight path, the distortion of the propeller inflow conditions due to the upwash generated by the presence of wings and flaps behind the propeller, and the interaction of the swirling turbulent propeller slipstream with the wing considered. The combination of such effects was found to produce an increase of 5 to 10 perceived noise decibels compared to non-installed configurations.

In parallel to wing related installation configurations, research concerning the interaction of propellers with empennages, fuselage and pylons showed how the addition of a pylon upstream of the propeller could increase the rotor Blade Passage Frequencies (BPF) of approximately 10 dB, while interaction with fuselage and empennages could increase the BPFs by 3 dB (Shivashankara et al., 1990). The inclusion of blowing techniques at the pylon trailing edge could reduce the pylon wake and flow distortion, obtaining BPFs comparable to those of isolated propellers (Sinnige et al., 2017). If semi-buried engines configurations are considered, the engines stage was found to be characterized by predominantly azimuthal unsteady blade loading with a less periodic tangential velocity variation in the rotor wake. The resulting installation noise sources would present no distinct tonal components and increased broadband noise levels (Romani et al., 2020).

The particular flow conditions involving new unconventional propulsion configurations, therefore, require methods for noise estimation able to include not only far-field but also near-field prediction capabilities. Given the limitations of the existing-to-date models, due, either to physical modelling simplifications or limited data availability during their development, in this work a new rotor noise prediction method is introduced, which is both fast and physical principles-based. The concept proposed combines simplified approaches within a Computational Aeroacoustics (CAA) framework, considering rotor blades modelled with three-dimensionally Gaussian regularised line-distribu-ted input forces, rotating uniformly around the rotor axis. The line-distributed source values can be directly specified from Blade Element Theory (BET) input data, or indirectly from Actuator Disc (AD) Reynolds Averaged Navier-Stokes (RANS) solutions. Both options allow to solve for the perturbed variables on a background flow solution that includes the aerodynamic effect of a propulsor, resulting in a method that is developed on physical principles and is able to address newly designed and already existing propulsion configurations, without requiring a priori empirical knowledge. In addition to the simplicity of its formulation, the model proposed would represent a fast prediction tool to aid the designer in selecting the best aircraft component configuration satisfying the required noise emissions.

To successfully predict installation noise sources, the model under development would require appropriate underlying equations to describe the flow physics mechanisms giving rise to the previously mentioned excess noise. A suitable system of equations for this purpose would be the Linearised Euler Equations (LEE), containing acoustic and vortical modes, whose interaction is believed to be responsible for the generation of noise sources categorizable as installation noise sources. LEEs have been extensively studied for aeroacoustics analysis of turbomachinery noise and exterior noise, and they have been among the most important equations for CAA applications for decades. These equations have been successfully applied in a various range of applications using Finite Difference (FD) discretization. An overview of the state-of-the-art finite difference methods for CAA can be found in (Tam, 2004), where references to relevant successful applications are reported.

For this reason, the noise prediction model was implemented in DLR's PIANO code, in which the simulations are carried out on hierarchical Cartesian meshes that resolve geometries by means of an Immersed Boundary Condition (IBC) for the solid-wall surfaces. The 4th order Dispersion-Relation-Preserving (DRP) scheme is used with explicit fourth-order Runge-Kutta (RK) time integration to solve linear governing equations describing the dynamics of – not necessarily small – perturbations over a steady background flow field provided by precursor RANS simulations.

In these lecture notes, the proposed approach is described, including validation with experiments performed in the scope of the ENODISE project (ENODISE, 2024).

# 2 Rotor Source Noise Model Implementation

The rotor noise model is based on the approach introduced in Franco et al. (2022), in which the rotor sources are modeled as three-dimensionally Gaussian regularised line-distributed input forces, rotating uniformly around the rotor axis. The line-distributed source values can be directly specified from BET input data, or indirectly from AD RANS solutions. Both options allow to solve for the perturbed variables on a background flow solution that includes the aerodynamic effect of a propulsor.

## 2.1 Model Based on Actuator Disc Surface Solution

For the model option based on the prescription of sources derived from an AD surface solution, the rotor load values obtained from the RANS solver are required to be prescribed on a two-dimensional circular surface, as exemplified in Fig. (1).

To define the appropriate source distributions from the AD RANS solution, the line sources are defined on the computational grid based on a local cylindrical coordinate system centered at the rotor hub being modeled. The line-distributed sources can be defined as straight or piecewise linear curves, at an initial location $\boldsymbol{X_{init}} = (r_{init}, \phi_{init}, x_{init})^T$ and with an initial strength at each radial location on the lines which reads as $w = 1/N_{blade}$.

If the rotor being modeled consists of multiple blades $N_{blade}$, the initial location of each line-distributed source is determined assuming an equi-spaced circumferential offset $2\pi/N_{blade}$ applied to $\phi_{init}$. Figure (2) shows the geometrical quantities of interest.

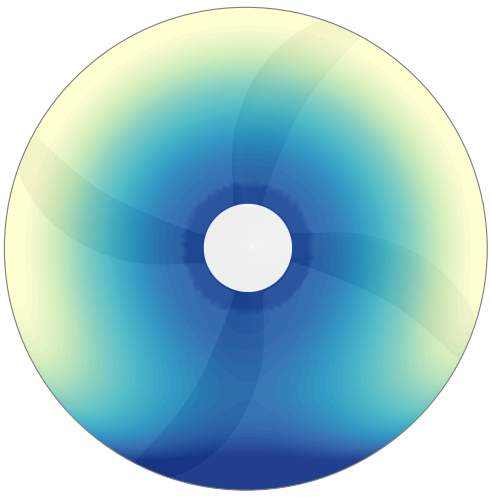


Figure 1: Actuator disc RANS solution example.

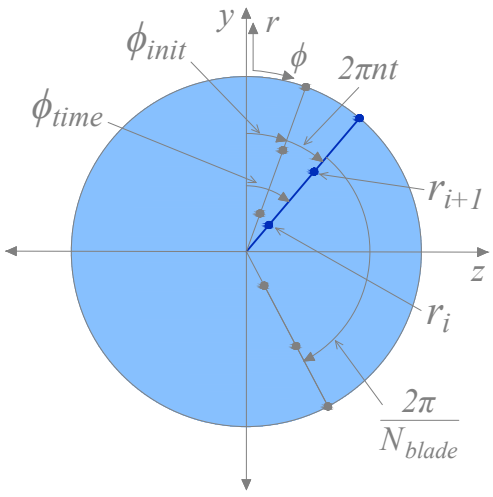



Figure 2: Rotor cylindrical coordinate system for a line-distributed source.

The preliminary defined line-distributed sources are then regularised with a two step-procedure, based on the consideration that for straight or piecewise linear curves the radial preliminary source strength value is already known. In the first step the value at a given radial grid location $r_{Grid}$ is obtained by linear interpolation of the initial strength value in the range $[r_i, r_{i+1}]$, resulting in $\boldsymbol{f_{Interp}} = (f_{Interp,r}, f_{Interp,\phi}, f_{Interp,x})^T$. The interpolation performed in the first step reduces the necessary dimensions over which regularising is

required, so that in the second step the regularisation of the preliminary line sources is obtained by convolution of $\boldsymbol{f_{Interp}}$ with the Gaussian kernel $K(\phi_{Src}, x_{Src}, \phi_{Grid}, x_{Grid})$, defined as:

$$K(\phi_{Src}, x_{Src}, \phi_{Grid}, x_{Grid}) = \left(\frac{ln(2)}{\pi}\right) \frac{1}{\varepsilon^2} \exp\left(\frac{-ln(2) d_{LineSrc}^2}{\varepsilon^2}\right) / \operatorname{erf}\left(\frac{\pi\sqrt{(ln(2))} r_{Src}}{\varepsilon}\right) \tag{1}$$

in which

$$d = \sqrt{r_{Src}^2(\phi_{Src} - \phi_{Grid})^2 + (x_{Src} - x_{Grid})^2} \tag{2}$$

is the distance measured on a cylindrical surface defined at a radius $r_{Src}$, where $\phi_{Src}$ is the line source azimuthal location, $\phi_{Grid}$ the grid point azimuthal coordinate, $x_{Src}$ the line source axial location, and $x_{Grid}$ the grid point axial coordinate. The variable $\varepsilon$ represents the half-width at half-maximum of the Gaussian kernel. The Gaussian kernel $K(\phi_{Src}, x_{Src}, \phi_{Grid}, x_{Grid})$ is derived from a 2D Gaussian Kernel independent of the $r$ coordinate, and averaged with an integration over the circumference, so that the resulting projected source, if integrated over the computational domain, would correspond to a unitary strength value. The error function term erf appearing at the denominator $K(\phi_{Src}, x_{Src}, \phi_{Grid}, x_{Grid})$ results from the integration, and for a given radius $r_{Src}$ represents a constant scale factor. Figure (3), Fig. (4), and Fig. (5) show a possible definition of line sources from a given rotor blades geometry, and its corresponding line source regularisation with the procedure described.

The regularised source values obtained from Eq. (1) are described as the sum of a steady mean and a fluctuating component, where only the fluctuating component is of interest for the system of perturbation equations considered. Hence, the perturbed regularised force values are calculated as $\boldsymbol{S'} = \boldsymbol{S} - \boldsymbol{S_{mean}}$, where the mean value $\boldsymbol{S_{mean}}$ is computed as the average source value over a rotor revolution, which in the case of constant rotational speed can be alternatively expressed as a spatial integral over a ring of given radius. After the regularisation of the preliminary sources of constant strength $w$, the related fluctuating sources' values $\boldsymbol{S'}$ are multiplicated with the load values on the AD surface, which is obtained through a Lagrangian high-order interpolator at a given radial and azimuthal coordinate on the circular surface. Figure (6) illustrates a possible line source distribution definition. The result of the multiplication is in the end scaled by the local circumference for a given radius, and assigned to the appropriate point of the FD discretization. The described procedure ensures that the integrated line-distributed sources values correspond to the original load values on the AD surface, and it is applied at each time dependent source location identified by the circumferential coordinate $\phi_{time}$, updated according to the sources revolutions per second $n$ prescribed in input.

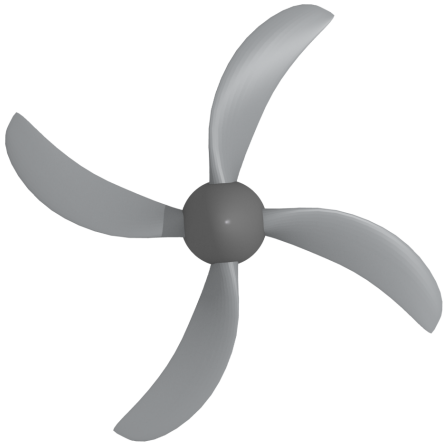


Figure 3: Original rotor blades to be modelled.

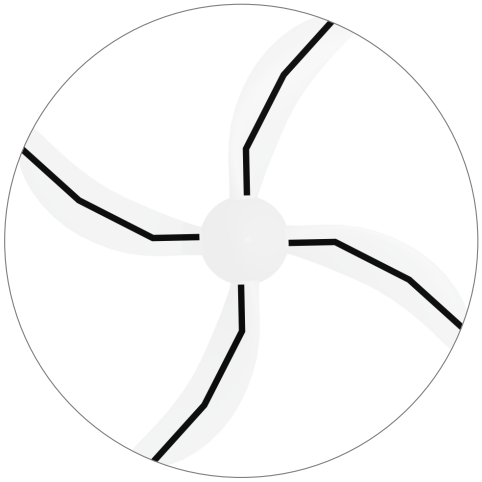


Figure 4: Line sources of constant strength $w$, defined from the original rotor blades.

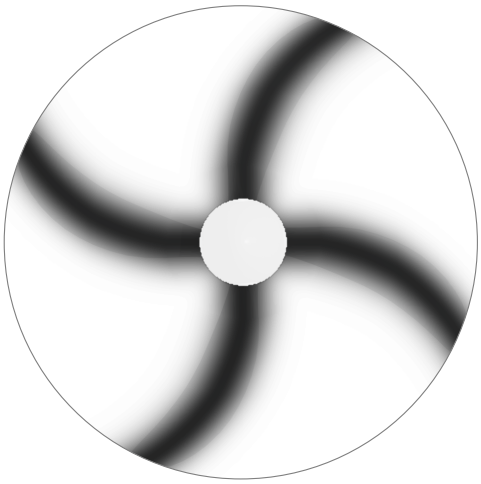


Figure 5: Regularisation of line sources of strength $w$.



Figure 6: Rotor sources from multiplication of interpolated AD sources with the line-distributed sources of preliminary strength.

## 2.2 Model Based on Blade Element Theory

The option included in the model that allows to prescribe noise sources from BET differs from the model described in Sec. (2.1) in the source values definition, but maintains the overall approach regarding the regularisation of line sources. The definition of the line-distributed sources is based on a local cylindrical coordinate system centered at the rotor hub being modelled, with sources that can be defined as straight or piecewise linear curves, at an initial location $\boldsymbol{X_{init}} = (r_{init}, \phi_{init}, x_{init})^T$. If multiple blades $N_{blade}$ are considered, the initial location of each line-distributed source is determined assuming an equi-spaced circumferential offset $2\pi/N_{blade}$ applied to $\phi_{init}$. Figure (2) is the reference for the geometrical quantities of interest. The source values to be regularised are based on the local sectional lift $L$ and sectional drag $D$ of the blade airfoil sections, determined from the flow kinematics in the sectional plane shown in Fig. (7), where $L$ and $D$ are defined in the aerodynamic coordinate system which is obtained by rotating the $-x$ and $-Azim$ axis by the angle $\phi$ of the vector of the inflow velocity $q$ at the airfoil.

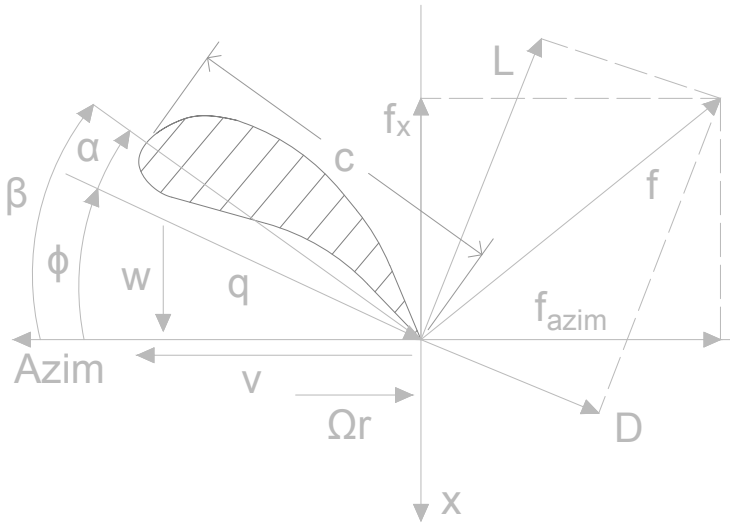



Figure 7: Flow kinematics reference for the BET-based model.

The angle of attack $\alpha$ of the chord relative to $q$ is obtained as:

$$\alpha = \beta - \phi \tag{3}$$

in which $\beta$ is the twist angle of the chord relative to the propeller plane. The angle $\phi$ and the inflow velocity $q$ depend on the rotational speed $\Omega r$ and the flow velocity of components $(w, v)$ in the local coordinate system $(x, Azim)$ of the sectional plane, and are obtained as:

$$\phi = atan2(\frac{w}{\text{sgn}(\Omega)(v - \Omega r)}) \tag{4}$$

and

$$q = -\sqrt{w^2 + (v - \Omega r)^2} \tag{5}$$

The local flow velocity is defined as the sum of the local mean flow and fluctuating velocity vector $(w, v) = (w_0, v_0) + (w', v')$, where $(w', v')$ is defined as the sum of the acoustic and hydrodynamic perturbed velocity vector defined in Sec. (2.5), to account for sound generation due to local flow disturbances.

For the sectional lift $L$ and sectional drag $D$ calculation, the necessary quantities are determined from tabulated values of airfoil chord length $c$, twist angle $\beta$, lift coefficient characteristic $c_L(\alpha)$ and drag coefficient characteristic $c_D(\alpha)$ for different blade sections. Lift coefficient and drag coefficient characteristics are typically obtained from 2D Computational Fluid Dynamics (CFD) simulations of the corresponding sectional blade airfoil profiles. For intermediate angles of attack $\alpha$ and blade radial sections locations $r$, the values of $c_L(\alpha)$ and $c_D(\alpha)$ are obtained performing bilinear interpolation of the tabulated values at the specified $r$ and $\alpha$, whereas values of chord $c$ and twist angle $\beta$ at the specified $r$ location are linearly interpolated from the tabulated values prescribed in input.

If the local angle of attack computed with Eq. (3) exceeds the limits of the values defined in the input table for a given radial location, the values of $c_L(\alpha)$ and $c_D(\alpha)$ are computed with a constant extrapolation of either the corresponding maximum or minimum aerodynamic coefficient value at the radial location considered. The lift $L$ and drag $D$ are then calculated from the interpolated values of $c(r)$, $\beta(r)$, $c_L(\alpha)$, $c_D(\alpha)$ as:

$$L = \frac{\rho}{2} q^2 c(r) c_L(\alpha) \tag{6}$$

$$D = \frac{\rho}{2} q^2 c(r) c_D(\alpha) \tag{7}$$

where $\rho$ denotes the density of the medium. To determine the source values to be regularised, in a first step the axial component $f_X$ and the azimuthal component $f_{Azim}$ of the resulting sectional load $f$ are computed as:

$$f_X = -Lcos(\phi) + Dsin(\phi) \tag{8}$$

$$f_{Azim} = -\operatorname{sgn}(\Omega)(Lsin(\phi) + Dcos(\phi)) \tag{9}$$

The sources to be prescribed in the rotor noise simulations need to be determined from the forces acting on the medium, therefore the final source values are determined as the opposite of the $f_X$ and $f_{Azim}$ values computed from Eq. (8) and Eq. (9) respectively. The source vector to be regularised is defined as $\boldsymbol{S} = (S_r, S_{Azim}, S_X) = (0, -f_{Azim}, -f_X)$.

The line-distributed sources are obtained with the same two step-procedure described in Sec. (2.1), considering Eq. (1) and Eq. (2) for the regularisation of $\boldsymbol{S}$. After the regularisation step, the fluctuating source values $\boldsymbol{S'}$ are determined as $\boldsymbol{S'} = \boldsymbol{S} - \boldsymbol{S_{mean}}$, where $\boldsymbol{S_{mean}}$ is defined as the average source value over a rotor revolution and computed as in Sec. (2.1), considering that for a constant rotational speed, $\boldsymbol{S_{mean}}$ can be alternatively expressed as a spatial integral over a ring of given radius. The source value to be averaged for determining $\boldsymbol{S_{mean}}$ is calculated based on the local load components obtained from Eq. (8) and Eq. (9), with the local mean flow velocity vector $(w_0, v_0)$.

The described procedure is applied at each time dependent source location identified by the circumferential coordinate $\phi_{time}$, updated according to the sources revolutions per second $n$ prescribed in input.

## 2.3 Thickness Noise Source Calculation

In addition to the prescription of regularised line-distributed loads, the rotor noise model includes the option of defining thickness noise sources for both the modeling options described in Sec. (2.1) and Sec. (2.2).

To prescribe thickness noise sources, the distribution of mass of medium displaced by the propeller blade is defined as $m(r_{Src}) = A_{airfoil}(r_{Src})\rho$, where $A_{airfoil}(r_{Src})$ is the area of the blade sectional airfoil profile at a given radial location along the blade span. In order to prescribe thickness noise source contributions, the calculation of the time derivative of the mass distribution $\dot{m}(r_{Src})$ has to be computed, which for a regularised source reads as:

$$\dot{m}_{Regularised}(r_{Src}) = \frac{\partial(m_{Regularised}(r_{Src}))}{\partial t} = \frac{\partial(m(r_{Src}) \cdot K(\phi_{Src}, x_{Src}, \phi_{Grid}, x_{Grid}))}{\partial t} \tag{10}$$

in which $K(\phi_{Src}, x_{Src}, \phi_{Grid}, x_{Grid})$ is the Gaussian kernel introduced in Eq. (1). Assuming a constant mass distribution $m(r_{Src})$, the calculation of the source $\dot{m}_{Regularised}(r_{Src})$ in Eq. (10) can be simplified further obtaining:

$$\dot{m}_{Regularised}(r_{Src}) = \frac{\partial(m(r_{Src}) \cdot K(\phi_{Src}, x_{Src}, \phi_{Grid}, x_{Grid}))}{\partial t} = \tag{11}$$
$$m(r_{Src}) \cdot \frac{\partial(K(\phi_{Src}, x_{Src}, \phi_{Grid}, x_{Grid}))}{\partial t} = m(r_{Src}) \cdot \frac{\partial(K(\phi_{Src}, x_{Src}, \phi_{Grid}, x_{Grid}))}{\partial \phi} \frac{\partial \phi}{\partial t}$$

The time derivative $\frac{\partial \phi}{\partial t}$ is the angular speed $\Omega = 2\pi n$ of the rotor. Since the Gaussian kernel $K(\phi_{Src}, x_{Src}, \phi_{Grid}, x_{Grid})$ has the property of zero mean for its angular derivative $\frac{\partial(K(\phi_{Src}, x_{Src}, \phi_{Grid}, x_{Grid}))}{\partial \phi}$, it can be obtained that $\dot{m}_{Regularised}(r_{Src}) = \dot{m}'_{Regularised}(r_{Src})$, and after computing the derivatives in Eq. (11) the regularised thickness source definition reads as:

$$\dot{m}'_{Regularised}(r_{Src}) = m(r_{Src}) \frac{\Delta\phi \cdot r_{Src}^2 \cdot \frac{2}{\varepsilon^4} \frac{(\ln(2))^2}{\pi} \cdot \exp\left(-\ln(2) \cdot \left(\frac{d}{\varepsilon}\right)^2\right)}{\operatorname{erf}\left(\pi \cdot \sqrt{\ln 2} \cdot \frac{r_{Src}}{\varepsilon}\right)} \Omega \tag{12}$$

with the angle difference $\Delta\phi = (\phi_{Src} - \phi_{Grid}) + n \cdot 2\pi$, normalized to have an angle in the range $[-\pi, \pi]$.

The distribution of mass of medium can be either prescribed on a circular surface, according to the source noise model described in Sec. (2.1), or it can be specified as an additional generic line source in addition to the load sources defined by the model option of Sec. (2.2). If the model option in Sec. (2.1) is considered, the thickness noise source value needs to be scaled by the local circumference for a given radius.

The resulting thickness noise source value obtained from Eq. (12) is the fluctuating thickness noise source $\dot{\theta}'$ to be assigned to the appropriate point of the FD discretization.

## 2.4 Broadband Noise Calculation

In addition to the tonal noise prediction, a rotor broadband noise prediction approach has been developed, based on Appel (2023). The toolchain is based on TAU (Gerhold, 2005) RANS simulations of multiple 2D airfoil sections, which provide the background meanflow for the Acoustic Perturbation Equations (APE) (Ewert and Schroeder, 2003), and also the necessary turbulence parameters to the FRPM method (Ewert et al., 2011) for the generation of a non-empiric source term in the APE. A 2D CAA simulation is then performed using the DLR code DISCO (Bauer et al., 2009), and the results obtained at given virtual microphones arranged in a circle in the 2D CAA domain are then corrected to account for the rotation of the rotor blade, the associated amplitude modulation and the variation of the distance to arbitrary evaluation points. In its current state, the toolchain uses the above approach only for the rotor trailing edge noise component, while the leading edge noise component is modelled via the semi-empirical Lowson model (Lowson, 1993), which reads as:

$$L_{p,1/3} = L_{p,1/3,HFC} + L_{p,1/3,LFC} = (10\log_{10}(HFC) + 58.4) + \left(10\log_{10}\left(\frac{LFC}{1+LFC}\right)\right) \tag{13}$$

with LFC and HFC indicating the low-frequency and high-frequency component, respectively:

$$HFC = \frac{\rho_\infty^2 c_0^2 \lambda d}{r^2} Ma^3 Turb_{Intens} K^3 (1+K^2)^{-\frac{7}{3}} \tag{14}$$

$$LFC = \frac{10 S^2 MaK^2}{\beta^2} \tag{15}$$

In Eq. 14 and Eq. 15, the terms appearing are defined:

$$D_L = \frac{\sin^2\theta \sin^2\phi}{(1.0 + Ma\cos\theta)^4} \tag{16}$$

as the low frequency directivity function,

$$K = \frac{\pi f c}{U_\infty} \tag{17}$$

as the wave number based on the chord length and the local flow velocity,

$$\beta^2 = 1 - Ma^2 \tag{18}$$

as the term based on the Prandtl-Glauert factor for the effects of compressibility at higher Mach number, and

$$S^2 = \left[\frac{2\pi K}{\beta^2} + \frac{1}{1 + 2.4\frac{K}{\beta^2}}\right]^{-1} \tag{19}$$

as the Sears function. In future, the APE-FRPM method will be considered for rotor leading edge noise as well.

The SPL correction factors used for the rotor trailing edge noise predictions are:

$$L_{p,Span} = 10\log_{10}\left(\frac{d_{Section}}{d_{Section,Ref.}}\right) \tag{20}$$

with $d_{Section}$ the section span, and $d_{Section,Ref.} = 1$

$$L_{p,Distance} = 10\log_{10}\left(\frac{r_{SectionCircleMics}}{r_{TrailingEdgeToFarfieldMic}}\right) \tag{21}$$

with $r_{SectionCircleMics}$ the radius of the 2D CAA virtual microphone circle, and $r_{TrailingEdgeToFarfieldMic}$ the distance from a 2D CAA virtual microphone to the farfield microphone for evaluation.

$$L_{p,2D-3D} = 10\log_{10}\left(\frac{1.4}{\pi}\frac{d_{Section}}{r_{SectionCircleMics}}Ma_{Section}\right) \tag{22}$$

with $Ma_{Section}$ the local section Mach number

$$L_{p,Amplitude} = 10\log_{10}\left(\frac{\sin(\phi)}{(1-|Ma_{Section}|\cos(\xi))^4}\right) \tag{23}$$

with $\phi$ the polar angle identifying the farfield microphone in a plane perpendicular to the 2D sectional trailing directivity, and $\xi$ the angle between the vector of blade leading edge flow and the line connecting the trailing edge to the observer.

The correction factors are applied as:

$$L_{p,Corrected} = L_{p,Span} + L_{p,Distance} + L_{p,2D-3D} + L_{p,Amplitude} \tag{24}$$

Figure 8, summarises the 2D CFD-CAA toolchain for trailing edge broadband noise prediction, while Fig. 9 shows the reference frame considered for the propagation to the farfield of the 2D CAA trailing edge noise data generated by the toolchain, using Eq. 24.

## 2.5 System Of Perturbation Equations

In combination with the rotor noise model, the system of perturbation equations considered is the LEE in the primitive variables form, presented here in vector notation:

$$\frac{\partial \rho'}{\partial t} + \nabla\cdot(\rho_0\boldsymbol{u'} + \rho'\boldsymbol{u_0}) = \dot{\theta}' \tag{25}$$

$$\frac{\partial \boldsymbol{u'}}{\partial t} + (\boldsymbol{u_0}\cdot\nabla)\boldsymbol{u'} + (\boldsymbol{u'}\cdot\nabla)\boldsymbol{u_0} + \frac{\nabla p'}{\rho_0} - \rho'\frac{\nabla p_0}{\rho_0^2} = \frac{\boldsymbol{f'}}{\rho_0} \tag{26}$$

$$\frac{\partial p'}{\partial t} + \boldsymbol{u_0}\cdot\nabla p' + \boldsymbol{u'}\cdot\nabla p_0 + \gamma p_0\nabla\cdot\boldsymbol{u'} + \gamma p'\nabla\cdot\boldsymbol{u_0} = \frac{c_0^2}{\gamma}\dot{\theta}' \tag{27}$$

where $\rho$, $\boldsymbol{u}$, $p$, $t$, and $\gamma$ are respectively the density, velocity, pressure, time, and specific heat ratio of air, with subscript 0 indicating mean flow quantities and primed symbols indicating perturbation quantities. $\dot{\theta}'$ represents rotor air displacement type of sources, and $\boldsymbol{f'}$ externally prescribed rotor fluctuating forces of the LEE.

A system of equations like the LEEs is the appropriate choice for the modelled rotor sources because the sources derived in Sec. 2.1 and Sec. 2.2 would require a system of

equations in which both acoustic and non-acoustic eigenmodes are present. In a first attempt, the rotor sources were considered applied to the APEs, but the results initially obtained proved that the rotor sources cannot be applied directly to this system of equations, due to the assumptions made on its derivation. An additional source filtering would be required in order to use the APE as perturbation equations, which has no known closed form solution at the moment for a regularised source. If the APEs are combined with a system of equations describing the non-acoustic eigenmodes, then the application of the rotor sources is possible, as done in (Franco et al., 2021), in which a velocity split approach was applied to the LEEs, in a similar manner as done in Sec. 3.11.

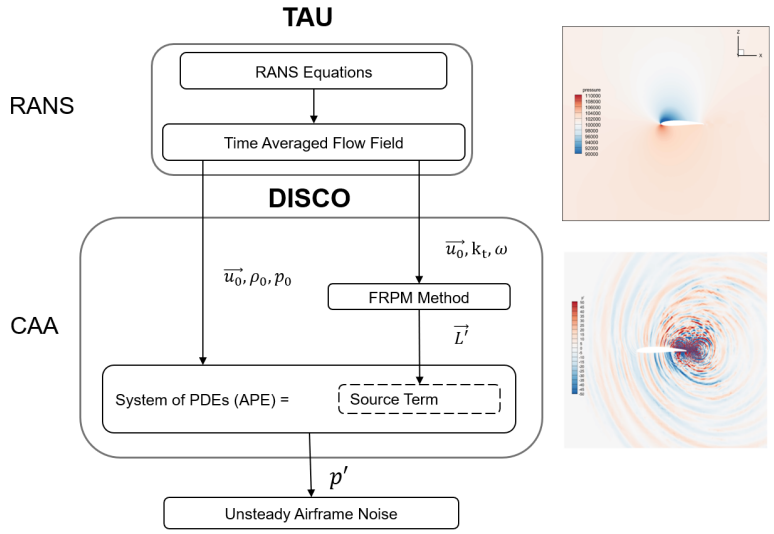



Figure 8: 2D CFD-CAA trailing edge broadband noise toolchain summary.

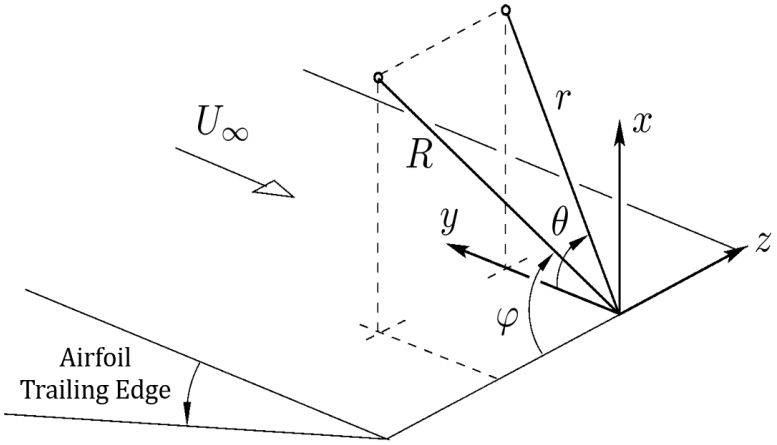



Figure 9: Reference frame for propagation to farfield of broadband noise data.

# 3 FRPM

## 3.1 Statistical noise modeling

Stochastic sound source modeling could be understood as a way to solve statistical noise models (also referred to as 'semi-empirical noise modeling' (Goldstein, 2003)) with state-of-the-art CAA methods. In the following a brief introduction to the theoretical background of statistical noise modeling will be given that highlights the relationship to stochastic methods. In Section 3.6 numerical results will be presented showing the agreement between noise spectra simulated with stochastic source terms and noise spectra obtained directly from statistical noise theory, thus confirming the solution of statistical noise models with CAA and stochastic sound sources.

Statistical noise source modeling is very closely related to the acoustic analogy concept ((Lighthill, 1952)), in which the sound generated by turbulent flow is reformulated as an acoustic wave equation forced by a source, which is a function of fluctuating turbulent quantities.

In all acoustic analogy approaches the acoustic problem is given in form of a forced linear acoustic wave equation with wave operator $\mathcal{L}$, acoustic variable $p$, and source $q_s$, which reads in the time domain,

$$\mathcal{L}p(\boldsymbol{x},t) = q_s(\boldsymbol{x},t). \tag{28}$$

For example, in Lighthill's acoustic the far-field acoustic pressure fluctuations are defined by

$$\left\{\frac{1}{c_\infty^2}\frac{\partial^2}{\partial t^2} - \boldsymbol{\nabla}^2\right\} p' = \frac{1}{c_\infty^2}\frac{\partial^2 T_{ij}}{\partial x_i \partial x_j}, \quad T_{ij} = \rho v_i v_j - \tau_{ij} + \left(p - c_\infty^2\rho\right)\delta_{ij}. \tag{29}$$

Hence, in that case

$$\mathcal{L} = \left\{\frac{1}{c_\infty^2}\frac{\partial^2}{\partial t^2} - \boldsymbol{\nabla}^2\right\}, \quad \text{and} \quad q_s = \frac{1}{c_\infty^2}\frac{\partial^2 T_{ij}}{\partial x_i \partial x_j}. \tag{30}$$

The far-field noise caused by the source term $q_s$ is

$$p_(\boldsymbol{x},t) = \frac{1}{2\pi}\int_{V_s}\iint_{-\infty}^{\infty}\hat{G}(\boldsymbol{x},\boldsymbol{y},\omega) q_s\left(\boldsymbol{y},t'\right)\exp\left[-i\omega(t-t')\right]\mathrm{d}t'\mathrm{d}\omega\mathrm{d}\boldsymbol{y}. \tag{31}$$

Here $\hat{G}(\boldsymbol{x},\boldsymbol{y},\omega)$ denotes the exact Green's function associated to wave operator $\mathcal{L}$ in Eq. (28), expressed in the frequency domain. The $t'$ integration transforms the spatiotemporal source term $q_s\left(\boldsymbol{y},t'\right)$ into frequency space, the second $\omega$ integration transforms the product of Green's function $\hat{G}$ and Fourier transform of the source back into time $t$. Here the transformation convention

$$\hat{p}(\boldsymbol{x},\omega) = \int_{-\infty}^{\infty} p'(\boldsymbol{x},t)e^{i\omega t}\mathrm{d}t \qquad p'(\boldsymbol{x},t) = \frac{1}{2\pi}\int_{-\infty}^{\infty}\hat{p}(\boldsymbol{x},\omega)e^{-i\omega t}d\omega$$

is applied. With the help of Eq. (31) an expression for the far-field spectrum $\hat{S}$ related to variable $p$ can be derived, i.e.

$$\begin{aligned}\hat{S}(\boldsymbol{x},\omega) = \quad & \iint_{V_s}\int_{-\infty}^{\infty}\hat{G}^*(\boldsymbol{x},\boldsymbol{y},\omega)\hat{G}(\boldsymbol{y}+\boldsymbol{r},\omega) \\ & \times\left\langle q_s\left(\boldsymbol{y},t'\right) q_s\left(\boldsymbol{y}+\boldsymbol{r},t'+\tau\right)\right\rangle\exp\left[i\omega\tau\right]\ \mathrm{d}\tau\ \mathrm{d}\boldsymbol{y}\ \mathrm{d}\boldsymbol{r}.\end{aligned} \tag{32}$$

The brackets $\langle \cdots \rangle$ denote an ensemble average. Since we consider ergodic problems, the ensemble and time averages are interchangeable. Note, this result follows for any acoustic analogy that formally can be expressed by Eq. (28).

The previous result is the formally derived mathematical statement that the far-field spectrum is unambiguously defined by the two-point cross-correlation of the source between points $\boldsymbol{y}$ and $\boldsymbol{y}+\boldsymbol{r}$ and times $t'$ and $t'+\tau$, i.e.

$$R(\boldsymbol{y},\boldsymbol{r},\tau) = \langle q_s\left(\boldsymbol{y},t'\right) q_s\left(\boldsymbol{y}+\boldsymbol{r},t'+\tau\right)\rangle\,. \tag{33}$$

In other words, time-averaged two-point statistics alone are necessary and sufficient to specify the acoustic far-field spectrum. Statistical noise theories rest upon mathematical models derived from experimental findings to express the cross-correlation Eq. (33).

In general the source $q_s$ is a function of other turbulent quantities. For example, applying Lighthill's acoustic analogy for jet mixing noise, the major contribution of the Lighthill tensor $T_{ij}$ to the source is given by $q_s = \partial^2 \rho_0 v_i v_j / \partial x_i \partial x_j$.

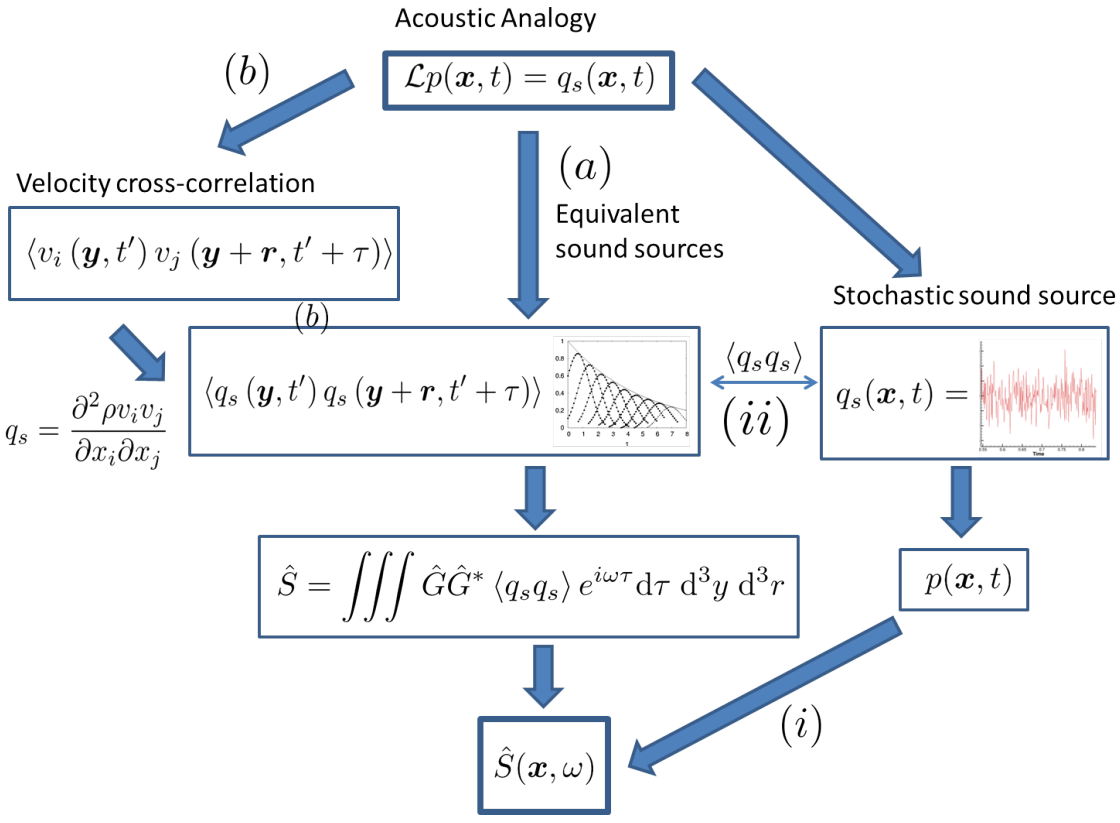



Figure 10: Solution to statistical noise theory via stochastic sound sources.

In the CAA-based approach presented in this paper the problem defined by Eq. (28) is solved directly in the time-domain. The sound source on the right-hand side is modeled with a stochastic approach that provides synthetic fluctuations possessing a two-point cross-correlation of the same type as being used in statistical noise theory. Furthermore, the modeling approach allows to specify the local source variance as well as its length- and time-scales exactly as prescribed e.g. by RANS statistics. Note, the derivation of Eq. (32) from Eq. (28) is still valid also in case of a synthetic source. Hence, the acoustic spectrum

that follows from Eq. (32) for a specific statistical noise theory will be reproduced by a time-domain CAA method if (i) the propagation equations correspond to the Green's function used in the statistical noise model and (ii) if the stochastically generated source realizes the same two-point cross-correlation. In other words, the time-domain CAA approach provides an alternative way to solve the integral Eq. (32) by computing far-field pressure fluctuations and by deducing the spectrum from them, refer to Fig. 10.

Based on the previous discussion two main approaches can be identified for statistical source modeling. Either (a) a statistical model is formulated for the full source term $q_s$, Eq. (33), or (b) a statistical model for a fluctuating turbulent sub-quantity, e.g. turbulent velocity, is realized. From this the full source term $q_s$ is eventually computed by means of an explicit source description given by acoustic analogy. The equivalent noise source model of(Tam and Auriault, 1999) could be regarded to belong to the first, i.e. full source term, approach. The second approach not necessarily provides better prediction capabilities. In fact, the statement provided by Eq. (32) that just the two-point cross-correlations have to be prescribed for a prediction of the far-field spectrum holds only for approach (a). If the source is derived as a function of other turbulent sub-quantities a cross-correlation model for the turbulent sub-quantity alone might not be sufficient to specify the source cross-correlation. For example, for a source determined by the Lighthill tensor, a correlation model for turbulent velocity specifies the source correlation only if the quasi-normality hypothesis holds(Bassetti, 2009). In general, however, more features have to be included in the statistical model of the sub-quantities in order to give the proper correlations for the complete source term. On the other hand, approach (b) provides a direct link of the modeled source quantities (e.g. turbulent velocity) to RANS statistics (e.g. turbulence kinetic energy). The statistics of the complete source used in approach (a), in general, are not directly provided and have to be linked to the RANS statistics e.g. on the basis of ad hoc models or dimensional reasoning.

## 3.2 Mathematical framework of (F)RPM

(F)RPM is a stochastic method to generate 4-D synthetic turbulence with locally prescribed one- and two-point statistics, with special focus on an applicability for CAA(Ewert and Edmunds, 2005; Ewert, 2006, 2008, 2007). In(Dieste and Gabal, 2009) a (F)RPM derived approach was adopted to simulate trailing edge noise and to compare it with theoretical results. In an Eulerian frame it provides a statistically stationary fluctuating sound source, which combines source convection with a temporal cross-correlation model. Due to the interconnection of temporal and spatial properties the method is considered a 4-D synthetic turbulence model.

In the following section the current status of the random particle-mesh method is briefly reviewed. Fig. 11 gives a general overview of its theoretical background. From the theoretical framework (top box) the features of the realized cross-correlation model can be derived (left branch in Fig. 11). The theoretical framework rests upon the newly introduced concept of convective white noise. A consistent numerical discretization leads to a numerical realization with random particles (right branch in Fig. 11). Hence, within the limits of accuracy of the numerical approach the particle model provides fluctuations which possess the derived cross-correlations (horizontal arrow in Fig. 11). A study concerning the numerical extent of validity can be found in Ref. (Ewert, 2007). Two different

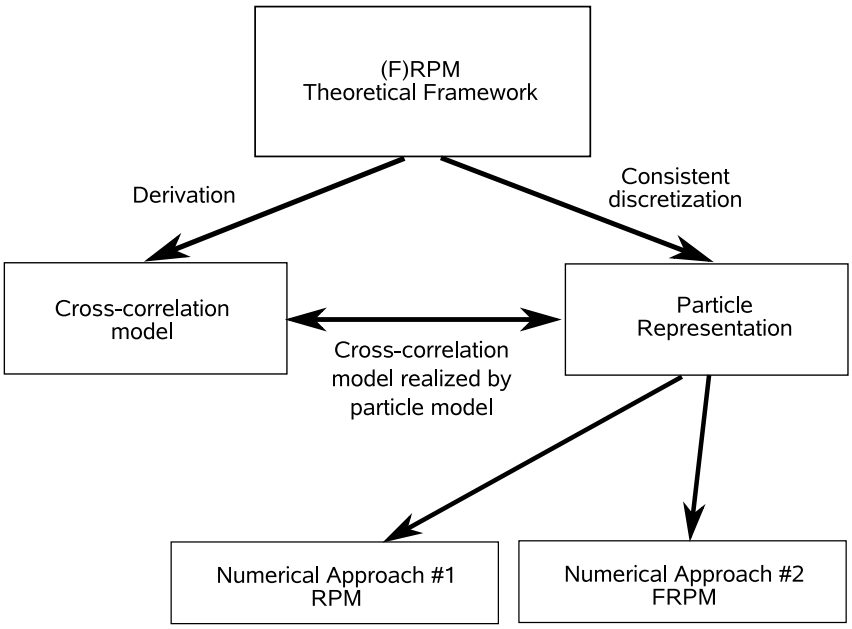



Figure 11: Theoretical background of the Random Particle Mesh method.

numerical procedures have been proposed to realize the particle model, namely RPM and FRPM.

In the Appendix the theoretical framework and the resulting cross-correlation model are presented. Section A.1.1 provides the general theoretical background. Section A.1.2 discusses the particle representation. The practical realization of the method will be discussed in the subsequent sections.

## 3.3 Generation of synthetic turbulence

In the framework of Random Particle-Mesh methods synthetic turbulence is generated by means of Lagrangian particles distributed over a limited spatial domain where sound sources ought to be realized. The Lagrangian particles are convected by a given steady (or unsteady) background flow. Each particle that crosses an outflow boundary of the source domain will be re-injected at an inflow boundary into the source domain such that the local particle density in the source domain is conserved. Further details of this process will be discussed further in Section 3.5.2.

Furthermore, each particle has associated a set of $i = 1 \dots m$ random variables; the actual value depends on the type of source term and spatial dimension of the considered problem. The actual random values attached to each particle will be modified over time by means of a stochastic partial differential equation. The cloud of random particles represents a numerical approximation to spatially delta-correlated white-noise. A fluctuating source component $q_i$ is obtained by distributing the $ith$ random deviate $r_{ik}$ of particle $k$ at (variable) position $x\ {}^{c}_{k}(t)$ with a mollifier kernel onto a computational mesh. The numerical approach realizes a weighted sum over all $N$ random particles,(Ewert, 2008),

defined by

$$q_i\left(\boldsymbol{x},t\right)=\sum_{k=1}^{N}\hat{A}G\left(\boldsymbol{x}-\boldsymbol{x}_k^c(t)\right)\frac{r_{ik}(t)}{\rho_0(\boldsymbol{x}_k^c)}. \tag{34}$$

The quantitiy $\rho_0$ denotes the mean-flow density ($\boldsymbol{\nabla}\cdot\rho_0\boldsymbol{u}_0=0$). In general, the approach is applicable to compressible fluids of considerable density variation. The amplitude scaling function $\hat{A}$ can be either a function of $\boldsymbol{x}$ (i.e. depending on the receiver position) or a function of the particle position $\boldsymbol{x}_k^c$. The Gaussian filter kernel is defined by

$$G(\boldsymbol{x}-\boldsymbol{x}_k^c)=\exp\left(-\frac{\pi}{2}\frac{|\boldsymbol{x}-\boldsymbol{x}_k^c|^2}{l_{\mathrm{s}}^2}\right), \tag{35}$$

where $l_s$ is the (local) integral length scale of turbulence, correspondent to the amplitude scaling function taken either at position $\boldsymbol{x}$ or $\boldsymbol{x}_k^c$. The properties of the random variables $r_{ik}$ are derived in the Appendix. To summarize the result, for frozen turbulence, i.e. in the absence of turbulence decay, the random variables satisfy

$$\langle r_{ik}(t)\rangle = 0 \tag{36}$$

$$\langle r_{ik}(t)r_{jl}(t)\rangle = \delta_{ij}\delta_{kl}\ \delta m_k \tag{37}$$

$$\dot{r}_{ik} = 0. \tag{38}$$

To summarize the meaning of these equations, $r_{ik}$ represent mutually un-correlated random variables, Eq. (37), with vanishing mean, Eq. (36), and a constant variance proportional to $\delta m_k$, which is an average fluid mass fraction related to each particle, defined by the fluid mass in the source domain divided by the number of particles used in that domain. Furthermore, the particles move with a convection velocity related to the convection velocity field value (typically, the time-averaged mean flow is used to prescribe the convection velocity field) at the actual particle position, i.e.

$$\dot{\boldsymbol{x}}_k^c=\boldsymbol{u}_0\left(\boldsymbol{x}_k^c\right). \tag{39}$$

For frozen turbulence the random variables of each particle remain constant. In case of an exponential decay the properties of the random variable $r_{ik}$ are prescribed by an individual Langevin equation for each random variable and particle, i.e.

$$\dot{r}_{ik}=-\frac{1}{\tau_s}r_{ik}+\sqrt{\frac{2}{\tau_s}}s_{ik}. \tag{40}$$

A (temporal) white-noise source term $s_{ik}$ appears on the right-hand side, with properties (refer to the Appendix)

$$\langle s_{ik}(t)\rangle = 0 \tag{41}$$

$$\langle s_{ik}(t)s_{jl}(t+\tau)\rangle = \delta m_k\delta(\tau)\delta_{ij}\delta_{kl}. \tag{42}$$

In other words, $s_{ik}$ represents (temporal) white-noise scaled with a factor of magnitude $\delta m_k$. The solution of the Langevin equation (40) with a source having correlation Eq. (42) yields a correlation of variable $r_{ik}$

$$\langle r_{ik}(t)r_{jl}(t+\tau)\rangle=\delta m_k\delta_{ij}\delta_{kl}\exp\left(-\frac{|\tau|}{\tau_s}\right). \tag{43}$$

The Langevin equation (40) can be solved numerically by the finite-difference equation, see e.g. Pope(Pope, 2000) pp. 484,

$$r_{ik}(t+\Delta t) = \left(1 - \frac{\Delta t}{\tau_s}\right) r_{ik}(t) + \left(\frac{2\delta m_k \Delta t}{\tau_s}\right)^{1/2} \sigma_{ik}(t), \tag{44}$$

where $\sigma_{ik}(t)$ are $m \times N_p$ mutually uncorrelated standardized Gaussian random variables ($\langle\sigma_{ik}(t)\rangle = 0$, $\langle\sigma_{ik}(t)\sigma_{jl}(t)\rangle = \delta_{ij}\delta_{kl}$) which are independent of themselves at different times ($\langle\sigma_{ik}(t)\sigma_{ik}(t')\rangle = 0$, for $t' \neq t$), and which are independent of $r_{ik}(t)$ at past times (e.g., $\langle\sigma_{ik}(t)r_{ik}(t')\rangle = 0$ for $t' \leq t$.

The random-particle mesh method with exponential time decay provides two-point cross-correlations of the form

$$R(\boldsymbol{x}, \boldsymbol{r}, \tau) = \exp\left(-\frac{|\tau|}{\tau_s} - \frac{\pi|\boldsymbol{r} - \boldsymbol{u}_0\tau|^2}{4l_s^2}\right). \tag{45}$$

Length scales and time scales can be locally prescribed e.g. from RANS solutions. The amplitude $\hat{A}$ allows to realize locally prescribed variances the actual value of which depends on the realized source term model. Alternative turbulence decay models using second order Langevin equations have been also proposed(Siefert and Ewert, 2009; Ewert et al., 2012; Dieste and Gabard, 2012; Neifeld et al., 2013).

## 3.4 Stochastic sources

Different aeroacoustic source terms can be realized from the FRPM method. Here we restrict ourselves to the generation of fluctuating vorticity and fluctuating turbulent velocities. Fluctuating vorticity is obtained by directly relating the generated synthetic turbulence field with one or more components of fluctuating vorticity, i.e.

$$\Omega_i' = q_i. \tag{46}$$

Fluctuating velocity in 2D and 3D can be obtained by defining the outcome of the stochastic procedure to represent a fluctuating stream function $\psi$ (2D), hence

$$v_i' = \epsilon_{ij}\frac{\partial\psi}{\partial x_j}, \tag{47}$$

or a vector potential $\psi_i$ (3D),

$$v_i' = \epsilon_{ijk}\frac{\partial\psi_k}{\partial x_j}, \tag{48}$$

refer to the discussion in the Appendix. The velocity fluctuations will be strictly divergence-free (solenoidal). Furthermore, the generated fluctuating velocity provides an exact realization of isotropic turbulence in 2D and 3D (based on a Gaussian cross-correlation model) since the realized cross-correlation tensor has the general shape

$$\mathcal{R}_{ij} = \frac{\left\langle v_i'(\boldsymbol{x})v_j'(\boldsymbol{x}+\boldsymbol{r})\right\rangle}{\left\langle v'^2_i\right\rangle} = [f(r) - g(r)]\,\frac{r_i r_j}{r^2} + g(r)\delta_{ij}, \tag{49}$$

with the longitudinal correlation function $f(r)$ defined by

$$f(r) = \exp\left(-\frac{\pi}{4}\frac{r^2}{l_s^2}\right), \tag{50}$$

and the 2D lateral correlation function related to it given by

$$g(r) = f + r\frac{Df}{Dr}, \tag{51}$$

respectively in 3D by

$$g(r) = f + \frac{r}{2}\frac{Df}{Dr}, \tag{52}$$

refer to the discussion in the Appendix. Based on this procedure, for the 3D velocity model the derived velocity fluctuation realized with (F)RPM reads

$$v_i'(\boldsymbol{x}, t) = \sum_{k=1}^{N} \epsilon_{ijk} \frac{\partial}{\partial x_j} \left[\hat{A} G\left(\boldsymbol{x} - \boldsymbol{x}_k^c(t)\right)\right] \frac{r_{ik}(t)}{\rho_0(\boldsymbol{x}_k^c)}. \tag{53}$$

## 3.5 Discretization

### 3.5.1 FRPM discretization

The second approach, named 'Fast RPM' (FRPM), makes use of a Cartesian background mesh. The synthetic fluctuating sound sources are computed in the cell vertices of the background mesh. The random field $\mathcal{U}$ is approximated by a cloud of $N$ particles that are evenly distributed over the mesh. The source amplitude $\hat{A}(\boldsymbol{x})$, as well as length and time scales together with the mean flow velocity and the mean-flow density are stored on the background mesh. The velocity at a specific particle location $\boldsymbol{x}_k^c$ is computed by linearly interpolating the values of $\boldsymbol{u}_0$ from the vertices of the cell occupied by the particle to the particle position itself. The random particles are convected according to the local flow velocity, Fig. 12(a). If $\boldsymbol{x}_{mn}$ denotes the coordinate of vertex $(m, n)$, the filtering integral Eq. (34) becomes

$$q_i(\boldsymbol{x}_{mn}, t) = \hat{A}(\boldsymbol{x}_{mn}) \sum_{k=1}^{N} G\left(\boldsymbol{x}_{mn} - \boldsymbol{x}_k^c(t)\right) \frac{r_{ik}(t)}{\rho_0(\boldsymbol{x}_k^c)}. \tag{54}$$

The background mesh could represent a subdomain of a Cartesian CAA mesh. Then the task to compute a source variable on the CAA mesh already is accomplished. If a body fitted CAA mesh is used, whose vertices do not coincide with those of the background mesh, an additional high-order interpolation is necessary to copy the source data from the background mesh to the CAA mesh at each time step.

Note, no special treatment has to be applied if solid bodies are present in the domain resolved by the background mesh, since the boundary condition is already considered in the mean flow delivered by RANS. In other words, convecting particles will not penetrate the area of the background mesh which represents a solid body.

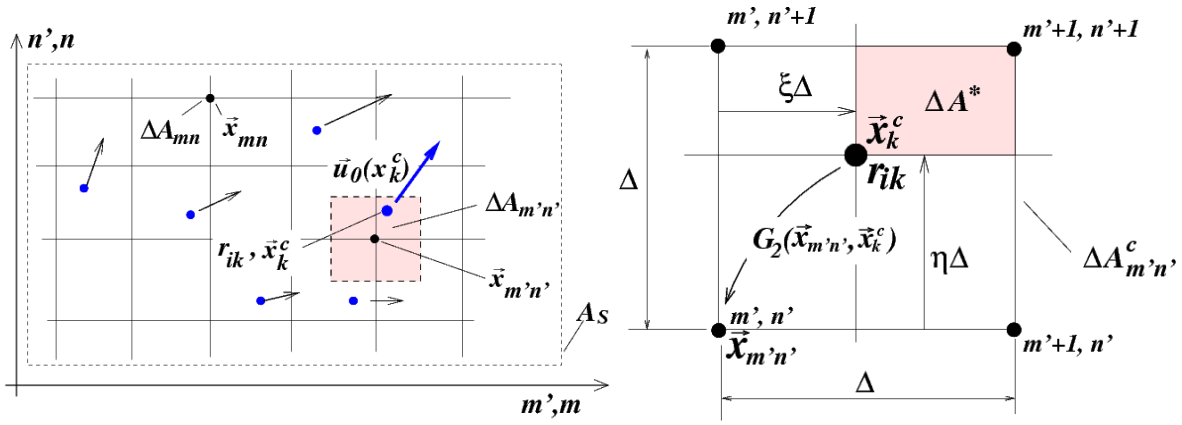



Figure 12: Random particles and notations for a 2-D background FRPM mesh. (a), node centered control volume $\Delta A_{m'n'}$ around vertex $(m', n')$. (b), area-weighting from particle to mesh point, $\Delta A^c_{m'n'}$ denotes the cell centered area related to the lower left point $(m', n')$. $G_2(\xi\Delta, \eta\Delta) = g(\xi)g(\eta) = \Delta A^*/\Delta A^c_{m'n'}$, the function $g(\xi)$ is defined by Eq. (57).

In the following the approach is discussed for 2-D. The extension to 3-D goes without saying. The spatial filter in Eq. (54) is split into the convolution of two filter kernels of length scale $l_1$ and $l_2$,

$$G(\boldsymbol{x}_{mn}, \boldsymbol{x}^{\,c}_{k}, l_s) = \int G_1(\boldsymbol{x}_{mn} - \boldsymbol{x}\,', l_1)\; G_2(\boldsymbol{x}\,', \boldsymbol{x}^{\,c}_{k}, l_2)\; \mathrm{d}\boldsymbol{x}\,' = G_1 \star G_2. \tag{55}$$

The resulting length scale $l_s$ is a function of scales $l_1$ and $l_2$. For example, if the second kernel is the Dirac delta function, i.e. $G_2(\boldsymbol{x}\,', \boldsymbol{x}^{\,c}_{k}, l_2 \to 0) = \delta(\boldsymbol{x}' - \boldsymbol{x}^{\,c}_{k})$, the resulting kernel is $G = G_1$ with length scale $l_s = l_1$. In the FRPM approach we apply a multi-dimensional filter kernel

$$G_2(\boldsymbol{x}, \boldsymbol{x}\,') = \frac{1}{\Delta^2} g\left(\frac{x - x\,'}{\Delta}\right) g\left(\frac{y - y'}{\Delta}\right) \tag{56}$$

together with a Gaussian filter $G_1$ on the background mesh. Here $\Delta$ denotes the cell spacing of the background mesh. The filter kernel $G_2$ is composed with the help of the function

$$g(\xi) = \begin{cases} 1 - |\xi| & \text{for} \quad |\xi| \le 1 \\ 0 & \text{for} \quad |\xi| > 1 \end{cases} \tag{57}$$

As discussed in Section A.1.1, the realized correlation function is defined by the self convolution of the applied filter kernel. Hence, from Eq. (56),

$$\mathcal{R} = G \star G = \underbrace{(G_1 \star G_1)}_{=:R_1} \star \underbrace{(G_2 \star G_2)}_{=:R_2}. \tag{58}$$

If $G_1$ is a Gaussian defined by Eq. (110) with length scale $l_1$, the function $R_1$ maintains Gaussian shape of integral length scale $l_1$. Furthermore, the convolution $R_2 = G_2 \star G_2$ reads

$$R_2\,(\boldsymbol{x}, \boldsymbol{x}') = \frac{1}{\Delta^2} r\left(\frac{x - x'}{\Delta}\right) r\left(\frac{y - y'}{\Delta}\right) \tag{59}$$

with $r = g \star g$. It was discussed in Ref. (Ewert, 2007) that the self-convolution of Eq. (57) provides the cubic spline function of the form

$$r(\xi) = \begin{cases} \frac{2}{3}\left(1 - \frac{3}{2}\xi^2 + \frac{3}{4}\xi^3\right) & \text{for} \quad |\xi| < 1 \\ \frac{1}{6}(2-\xi)^3 & \text{for} \quad 1 \le |\xi| < 2 \\ 0 & \text{for} \quad 2 \le |\xi| \end{cases}, \tag{60}$$

which closely resembles a normal distribution of standard deviation $\sigma = 3/2\sqrt{2\pi}$, i.e. $r \simeq 2/3 \exp(-4\pi\xi^2/9)$. The standard deviation corresponds to an integral length scale $L_i = 3/4$ related to the Gaussian $\exp(-\pi\xi^2/4L_i^2)$. Consequently, the definition Eq. (56) yields a function $R_2$ which closely resembles a normal distribution based on a Gaussian of integral length scale $l_2 = 3/4\Delta$. Finally, the spatial correlation function $\mathcal{R} = R_1 \star R_2$ that results from the filter kernel Eq. (55) approximately becomes a Gaussian realizing a combined integral length scale $\sqrt{l_1^2 + l_2^2}$.

The convolution integral Eq. (55) is approximated by the discrete convolution

$$G(\boldsymbol{x}_{mn}, \boldsymbol{x}_k^c) = \sum_{m'} \sum_{n'} G_1(\boldsymbol{x}_{mn} - \boldsymbol{x}_{m'n'}) G_2(\boldsymbol{x}_{m'n'} - \boldsymbol{x}_k^c) \Delta A_{m'n'}, \tag{61}$$

where $\Delta A_{m'n'} = \Delta^2$ represents a node centered control area of the background mesh, refer to Fig. 12.

By combining Eq. (54) and Eq. (61) and changing the order of summation, the procedure becomes

$$q_i(\boldsymbol{x}_{mn}, t) = \hat{A}(\boldsymbol{x}_{mn}) \sum_{m'} \sum_{n'} G_1(\boldsymbol{x}_{mn} - \boldsymbol{x}_{m'n'}) \underbrace{\sum_{k=1}^{N} g\left(\left(\frac{x_{m'n'} - x_k^c}{\Delta}\right) g\left(\frac{y_{m'n'} - y_k^c}{\Delta}\right) \frac{r_{ik}(t)}{\rho_0(\boldsymbol{x}_k^c)}\right.}_{=: w_{m'n'}}. \tag{62}$$

Practically, the rightmost summation over all $N$ particles with filter

$$G_2(\boldsymbol{x}_{m'n'} - \boldsymbol{x}_k^c) = g\left(\frac{x_{m'n'} - x_k^c}{\Delta}\right) g\left(\frac{y_{m'n'} - y_k^c}{\Delta}\right) \tag{63}$$

means to run over all cells of the background mesh and to interpolate via area weighting the random deviates of all particles contained in that particular cell onto the surrounding four cell vertices, refer to Fig. 12(b). Let $w_{m'n'}$ define the sum of all contributions from interpolation to vertex $(m', n')$. Then, for a given cell vertex all particles in the nearest four cells that share this vertex will provide a contribution to $w_{m'n'}$. The summation of $w_{m'n'}$ times the second filter kernel over all $m'$ and $n'$ is a procedure carried out on the background mesh alone. That is, the first filter interpolates the random values of the particles onto the vertices of the background mesh. The second filter $G_1$ with length scale $l_1$ accomplishes a filtered field on the background mesh.

By comparing the definition of $w_{m'n'}$ in Eq. (62) with the sum in Eq. (34), it becomes evident that the generation of the field $w_{m'n'}$ can be understood as the filtering of convective white-noise with the spatial filter $G_2\ \Delta^2$, refer to Eq. (56) for the definition of $G_2$. In other words, $w_{m'n'}$ represents a field with an integral length scale $l_2 = 3/4\Delta$ that follows from the application of filter kernel $G_2$. In wave-number space, a good approximation

to white-noise might be expected to be realized up to a wave-number corresponding to a wave-length of order given by the integral length scale, i.e. $2\pi/l_2$. Indeed, a very close agreement with the expected behavior was demonstrated numerically in(Ewert, 2007). If $\Delta$ is sufficiently smaller than $l_1$ it almost has no impact on the realized length scale, i.e. $l_s \approx l_1$. For smaller $l_1$, e.g. if a RANS length scales drops below $\Delta$, the resulting length scale is automatically limited to $3\Delta/4$.

Note, the filtering of convective white-noise with $G_2$ applied in the FRPM method realizes, besides a cut-off in wave-number space, also the removal of the non-resolved scales from the energy budget of the finally achieved variance of the fluctuations. In other words, the FRPM method automatically accounts for the truncation of the spectrum and an explicit additional reduction of the amplitude $\hat{A}$, Eq. (113), is unnecessary. The cut-off wave-number is implicitly defined by the mesh spacing of the background mesh. Theoretically, the effective amplitude reduction implicitly provided by FRPM approximately is $l_1/\sqrt{l_1^2 + l_2^2}$.

### 3.5.2 Distribution of particles on background mesh

At first some notations are introduced that will be used in the subsequent discussion. Fig. 13 presents a typical source set up for the FRPM background mesh, involving regions occupied by a solid body and in- and outflow boundaries. A cell located completely inside a solid body is termed a solid cell. Otherwise it is termed a fluid cell. Each fluid cell is assigned one integer index. The total number of fluid cells is $M$ and the total number of particles to be distributed is denoted by $N$.

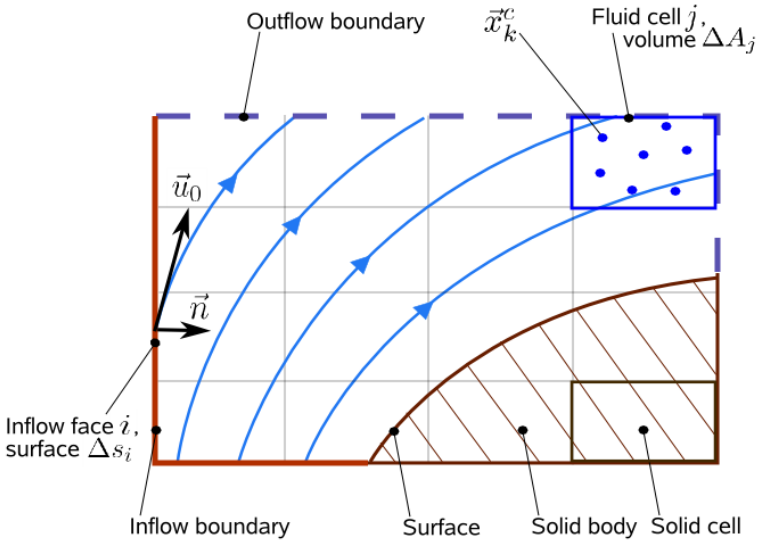



Figure 13: FRPM background mesh and nomenclature.

The variance of the random variables used in Eq. (34) is proportional to the fluid mass of the volume occupied by each particle, Eq. (116). Hence, the scaling of the random values carried by each particle is closely related to the distribution of particles on the background mesh. Next the distribution of particles is explained assuming a constant and equal mass for all particles, i.e. $\delta m_k = \delta m = const$. A constant mass $\delta m$ attributed

to all particles implies that the particles are distributed over the background mesh such that the mean particle density, which is defined by time averaging the number of particles contained in a fluid cell, corresponds to $\Delta m_i/\delta m$, where

$$\Delta m_i = \int_{\Delta A_i} \rho_0 \mathrm{d}^2 x, \tag{64}$$

is the mass of fluid cell $i$ and $\Delta A_i$ denotes its area. The (variable) particle density of a fluid cell is defined by

$$n_i(t) = \sum_{k=1}^{N} \int_{\Delta A_i} \delta\left(\boldsymbol{x} - \boldsymbol{x}_k^c(t)\right)\ \mathrm{d}^2 x. \tag{65}$$

From the particle density the mean particle density infers

$$\overline{n_i} = \lim_{T\to\infty} \frac{1}{T} \int_0^T n_i(t)\mathrm{d}t. \tag{66}$$

Hence,

$$\overline{n_i}\ \delta m \to \Delta m_i \tag{67}$$

This relation is achieved in two steps. First, an initial particle distribution is generated by distributing $N$ particles over all $M$ fluid cells. The cumulated mass of all fluid cells is given by $m = \sum_{i=1}^{M} \Delta m_i$ and the effective particle mass realized with $N$ particles is $\delta m = m/N$.

The probability to find a particle in cell $i$ is given by $\Delta m_i/m$. Hence, a discrete cumulative distribution function (CDF) can be attributed to all cells $CDF_j := \sum_{i=1}^{j} \Delta m_i/m$, with $CDF_0 = 0$ and $CDF_N = 1$, where $CDF_j - CDF_{j-1}$ defines the probability to find a particle in cell $j$. The initial distribution is accomplished by using standard algorithms to invert the cumulative distribution function. Next, uniformly distributed random numbers in the range between 0 and 1 are realized for all $N$ particles. The inverted CDF provides the link between the random number and the fluid cell where a particle actually is seeded. In the limit $N \to \infty$ this procedure generates the desired particle density (while the particle mass $\delta m$ would simultaneously tend to zero).

### 3.5.3 Inflow particle seeding

During run time particles move out of the computational source domain. To maintain the appropriate particle density each particle that leaves the domain is reinserted at the inflow boundary, refer to Fig. 13. Akin to the algorithms to initially distribute the particles, a discrete cumulative distribution function is associated to the inflow surface, which is defined by all cell faces on the inflow boundary. The flux over inflow face $i$ is given by

$$\dot{m}_i = \int_{\Delta s_i} \rho_0 \left(\boldsymbol{u}_0 \cdot \boldsymbol{n}\right) \mathrm{d}s. \tag{68}$$

Here $s$ denotes a coordinate along the inflow surface (in 2-D a line), and $\Delta s_i$ is the inflow cell face $i$. The discrete CDF is $CDF_j = \dot{m}_i / \sum \dot{m}_i$, where $CDF_j - CDF_{j-1}$ defines the probability that a particle enters the domain via face $i$. For each particle due to

be redistributed an uniform random number is generated which, via the inverted CDF, provides the inflow face to be used.

The random distribution of particles means that the volume occupied by each particle slightly fluctuates around the targeted value $\delta V_k = \delta m/\rho_0$. Such deviations from the theoretical model give rise to numerical errors as the difference between the theoretically derived and numerically realized statistical features of the fluctuating source. Currently, some preliminary best-practice experience has been obtained for the application of the FRPM method, which indicates a relatively robust realization of the desired source statistics with small numerical errors. Numerical experiments (Ewert, 2007) reveal an averaged particle density of 5 particles per cell needed in 2-D to generate statistical features (cross-correlation function, variance of fluctuations, Gaussian probability density function of fluctuations) in very close agreement with the theoretically deduced properties. Hence, the overall number of particles needed becomes $N \geq 5M$. Theoretical considerations for 2-D predict a particle density threshold in the same range and an even reduced particle density of half that value for a 3-D problem.

Another concern is the possibility of a temporal drift in the local particle density, e.g. due to accumulated errors in the numerically integrated particle positions, potentially giving rise to a rarefication or concentration of particles in different areas of the source region.

Deviations from the expected particle density would generate an erroneous source variance. However, numerical tests confirm that the mean particle density can be conserved over typical computational times needed for unsteady aeroacoustic simulations based on a second order accurate integration of the particle convection.

In addition to the previously described particle seeding procedure, a modified procedure was also tested, where an actual particle density was computed for all cell vertices at each time step to locally correct the random deviates for possible drift effects. It was found that this procedure completely avoids the occurrence of a drift in the source amplitude, albeit needs higher local particle densities to accomplish the theoretical statistics.

## 3.6 Validation of stochastic method

The intention of the stochastic method used herein is to realize a fluctuating source with prescribed cross-correlation and variance for a time marching CAA method to obtain the sound spectrum otherwise prescribed by Eq. (32). In other words, a time marching method with stochastic sound sources is deemed an alternative way to predict the far-field spectra of statistical noise theory, refer to Fig. 10. Subsequently we will show numerically that indeed equal spectra are numerically obtained. The 2-D test problem is shown in Fig. 14.

A Gaussian distributed source region is considered by choosing a source variance distribution

$$\hat{R}(\boldsymbol{x}) = \langle q_s \rangle = \exp\left( -\frac{|x_1 - a_1|^2}{2b_1^2} - \frac{|x_2 - a_2|^2}{2b_2^2} \right), \tag{69}$$

where $\boldsymbol{a} = (a_1, a_2)^T$ is the center point of the Gaussian distribution, and $\boldsymbol{b} = (b_1, b_2)^T$ is the Gaussian half-width. Non-dimensionalized quantities are used for this test problem. The center of the source and the Gaussian half-width are chosen as $\boldsymbol{a} = (1.0, 1.0)^T$, and $\boldsymbol{b} = (0.2, 0.1)^T$, respectively. The integration domain for the analytical solution has the

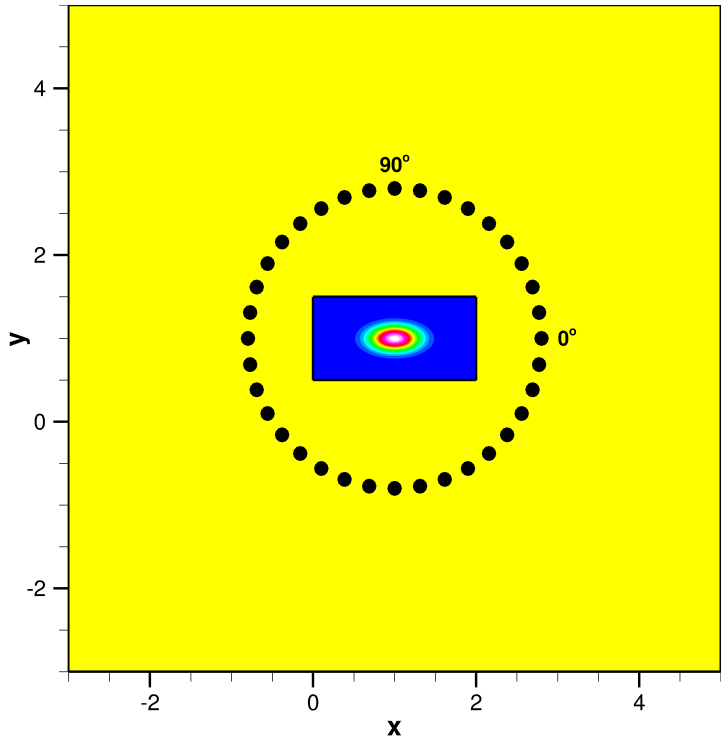



Figure 14: Setup for the CAA-computation with synthetic sources. Red: CAA-domain, Blue: source-domain with gauss-distributed variance, Black dots: Microphone positions at radius $R = 1.8$.

same size as the source domain for the numerical solution, i.e. two length units in flow-direction and one length unit in direction perpendicular to the flow. The observer points are located equidistantly on a circle of radius $R = 1.8$ around the center of the Gaussian source distribution. The rectangular CAA domain is much bigger (8 length units per side) to minimize boundary effects. The source domain and the CAA-domain are resolved with the same cell size.

The cross-correlation model used for the source term is given by

$$\langle q_s(\boldsymbol{x}_1, t_1) q_s(\boldsymbol{x}_1 + \boldsymbol{r}, t_1 + \tau) \rangle = \hat{R}(\boldsymbol{x}_1) \times \exp\left\{ -\frac{|\tau|}{\tau_s} - \frac{\ln(2)}{l_s^2} \left[ (r_1 - u_c)^2 + r_2^2 \right] \right\}. \quad (70)$$

To facilitate the derivation of the analytical solution for the sound spectrum, we consider a non-zero convection velocity $u_c$ in the source model, but compute sound propagation in a medium at rest. For sound propagation in 2-D, the LEE for a medium at rest with a source term $q_s$ on the right-hand side of the pressure equation read

$$\frac{\partial \boldsymbol{u}'}{\partial t} + \frac{1}{\rho_0} \boldsymbol{\nabla} p' = 0 \quad (71)$$

$$\frac{\partial p'}{\partial t} + \gamma p_0 \boldsymbol{\nabla} \cdot \boldsymbol{u}' = q_s. \quad (72)$$

The analytic solution to the sound spectrum is derived as an integral over the source

volume

$$\hat{S}(\boldsymbol{x},\omega) = 2\left(\frac{\pi}{\ln(2)}\right)\int_{V_s} \hat{R}\tau_s l_s^2 \left|\hat{p}_a(\boldsymbol{x}_1,\boldsymbol{x},\omega)\right|^2 \frac{\exp\left[-\frac{\omega^2 l_s^2}{4\ln(2)c_0^2}\right]}{1+\omega^2\tau_s^2\left(1-M_0\cos\theta\right)^2}\mathrm{d}^2\boldsymbol{x}_1, \tag{73}$$

refer to the discussion in Appendix A.2.2. The polar angle $\theta$ is measured from the positive x-axis, as indicated in Fig. 14. $M_0 = u_c/c_0$ indicates the source convection velocity. An analytical expression for the square of the Green's function that appears in this formula can be derived based on the simplified propagation model considered here,

$$\left|\hat{p}_a(\boldsymbol{x}_1,\boldsymbol{x},\omega)\right|^2 = \frac{\omega^2}{16c_0^4}\left[J_0^2\left(\frac{\omega}{c_0}\left|\boldsymbol{x}-\boldsymbol{x}_1\right|\right) + Y_0^2\left(\frac{\omega}{c_0}\left|\boldsymbol{x}-\boldsymbol{x}_1\right|\right)\right], \tag{74}$$

refer to the discussion in Appendix A.2.3.

The time and length scale parameter used for the test problem are taken constant over the source region. Fig. 15 shows a snapshot of the radiated pressure field of a RPM-CAA simulation with parameters $M_0 = 0.7$, $l_s = 0.05$, and $\tau_s = 0.29$. The PIANO code of DLR is applied with a fourth order Runge-Kutta scheme for time integration and the 7-point DRP scheme of Tam and Webb(Tam and Webb, 1993) for spatial discretization. The mesh resolution is 10 points-per-wavelength (PPW) for a non-dimensional frequency $f = 10^1$. At the far-field boundaries a radiation condition is used. Note, a first-order Langevin model is applied in the RPM realization to exactly reproduce an exponential time decorrelation model. No numerical problems are observed in its application. The stochastic source is updated every full Runge-Kutta step. For substeps an appropriate combination of the source term at earlier completed time levels is used. Due to the source convection from left to right, sound radiation in convection direction is enhanced in Fig. 15.

Figs. 16 and 17 presents detailed spectra for three selected combinations of the source parameters (solid lines). For these test simulations, the non-dimensional parameter combinations shown in Table 1 are considered. The spectra are juxtaposed to the analytical solution based on Eq. (73) with Eq. (74) (Eq. (73) is finally integrated numerically). Eq. (74) is the square of the analytical Green's function whose asymptotic limit is also provided in Appendix A.2.3 by Eq. (194), which gives a proportionality with frequency $\omega$. With the denominator of Eq. (73) a functional dependence is obtained, which provides an increasing power spectral density $\propto \omega$ for small frequencies, whereas for larger frequencies a decay $\propto \omega^{-1}$ follows. The frequency of the spectral maximum obtained for these to contributions is proportional to $\tau_s^{-1}$. For larger frequencies the exponential function in the nominator causes a successively increasing decay of the spectrum.

This general trend is confirmed by the analytical spectra in Figs. 16 and 17 (dashed lines). Fig. 16 shows results for a downstream observer location at polar angle $\theta = 0°$.

| $M_0$ | $l_s$ | $\tau_s$ |
|---|---|---|
| 0.3 | 0.05 | 0.67 |
| 0.3 | 0.10 | 0.67 |
| 0.3 | 0.05 | 0.29 |

Table 1: Non-dimensional convection velocity, length- and time-scales used for the test problem.

Fig. 17 is related to $\theta = 90°$. With decreasing $\tau_s$ the spectral maximum shifts to higher frequencies. This effect is more pronounced at $\theta = 0°$. If only the length scale is varied a uniform shift in level over the entire spectrum is caused. Despite some deviations in the low frequency regime, in total a very good agreement of analytical and RPM-CAA solution in terms of absolute levels and spectral shape can be observed. The wiggles seen in the simulated spectrum would decrease further with increasing simulation/sampling time. The low-frequency deviations perhaps could be caused by the far-field approximation involved in the derivation of the analytical result, refer to Appendix A.2.1.

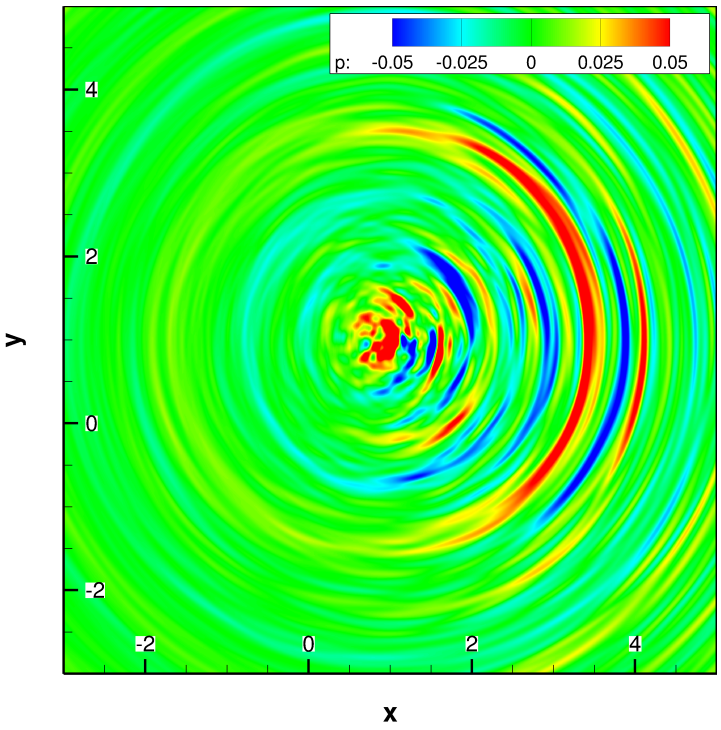



Figure 15: Instantanious contour plot of the pressure fluctiations from the CAA-computation with synthetic sources at time $t = 400$, $M_0 = 0.7$, $l_s = 0.05$ and $\tau_s = 0.29$.

## 3.7 Governing equations

The acoustic simulations are based on the APE-4 system (for their formulations refer e.g. to(Ewert et al., 2009)) with dominating vortex sound source, which reads

$$\begin{aligned} \frac{\partial p'}{\partial t} + c_0^2 \nabla \cdot \left( \rho^0 \boldsymbol{v'} + \boldsymbol{v}_0 \frac{p'}{c_0^2} \right) &= 0 \\ \frac{\partial \boldsymbol{v'}}{\partial t} + \nabla(\boldsymbol{v}_0 \cdot \boldsymbol{v'}) + \nabla \left( \frac{p'}{\rho_0} \right) &= \boldsymbol{q_m}. \end{aligned} \tag{75}$$

Quantities with superscript 0 denote steady mean-flow variables, the prime indicates fluctuating quantities. The Favre averaged squared sound speed is defined by the steady mean-flow, i.e. $\widetilde{c^2} = \gamma p^0/\rho^0$, where $\gamma = 1.40$. The fluctuating acoustic pressure is linked to $\rho'$ via

$$p' = \widetilde{c^2} \rho'. \tag{76}$$

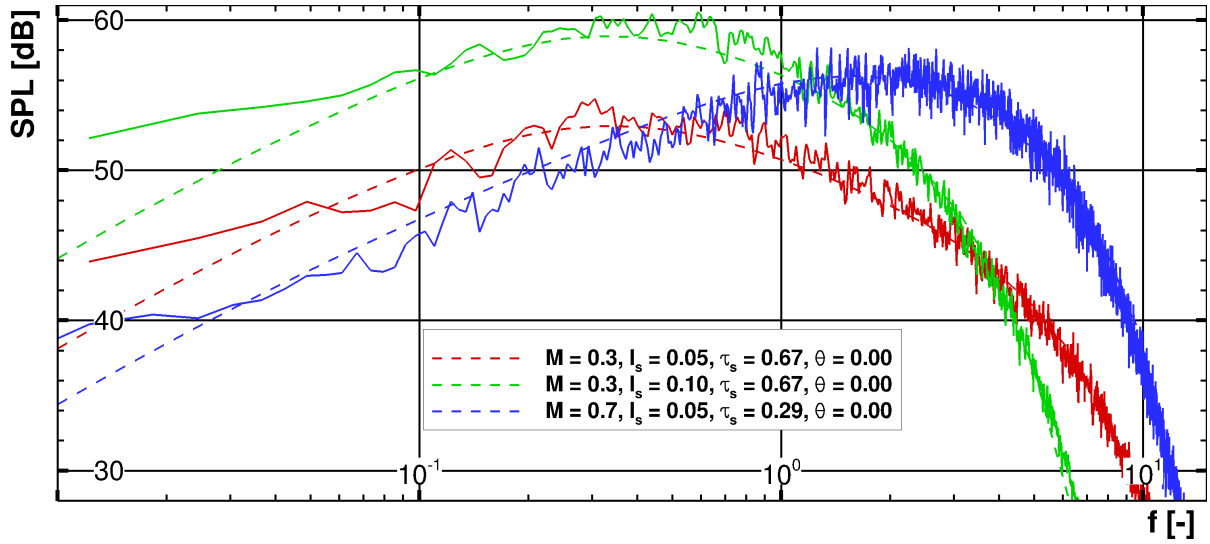



Figure 16: Comparison between analytical solution, Eq. (73) with Eq. (74), and results of the applied RPM-method for polar angle $\theta = 0°$ (downstream direction), radius $R = 1.8$; analytical solutions are indicated by the dashed lines, RPM solutions by solid lines; source convection velocity $M = u_c/c_0$, length scale $l_s$ and time scale $\tau_s$ varied.

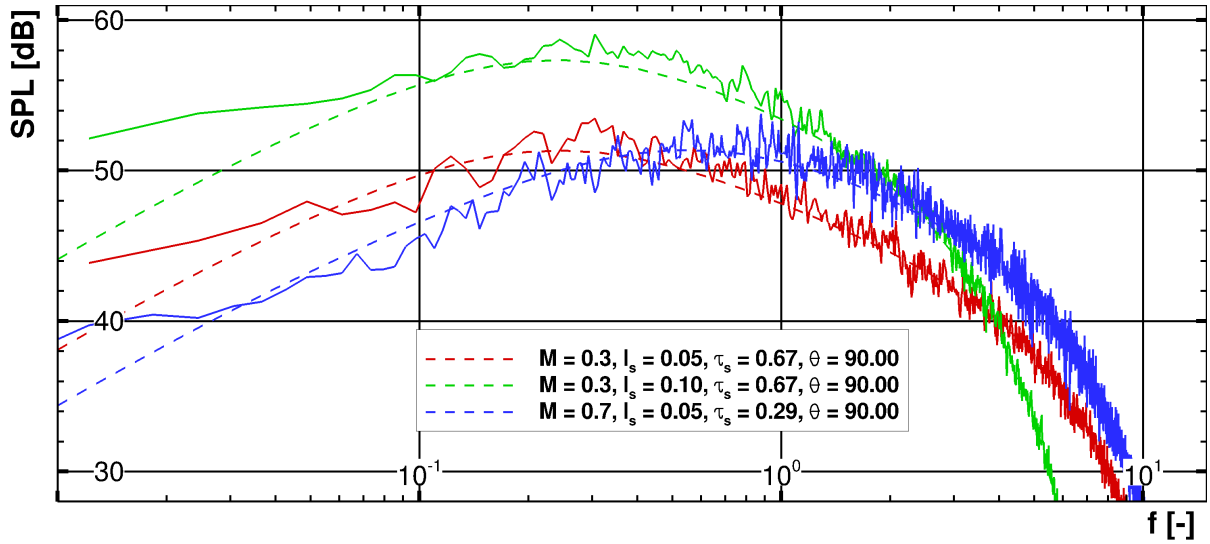



Figure 17: Comparison between analytical solution, Eq. (73) with Eq. (74), and results of the applied RPM-method for polar angle $\theta = 90°$, radius $R = 1.8$; the analytical solutions are indicated by the dashed lines, RPM solutions by solid lines; source convection velocity $M = u_c/c_0$, length scale $l_s$ and time scale $\tau_s$ varied.

As the dominating right-hand side sound source the fluctuating Lamb vector occurs as a vortex sound source

$$\boldsymbol{q_m} = -\underbrace{\boldsymbol{\omega}_0 \times \boldsymbol{v}'}_{I} - \underbrace{\boldsymbol{\omega}' \times \boldsymbol{v}_0}_{II} - \underbrace{\boldsymbol{\omega}' \times \boldsymbol{v}' + [\langle \boldsymbol{\omega}' \times \boldsymbol{v}' \rangle]}_{III}. \tag{77}$$

Here $\boldsymbol{v}'$ and $\boldsymbol{v}_0$ denote fluctuating velocities and mean velocities, respectively. The curl of the velocity defines vorticity, e.g.

$$\boldsymbol{\omega}' = \boldsymbol{\nabla} \times \boldsymbol{v}'. \tag{78}$$

Altogether the system Eq. (75) with source (77) constitutes an acoustic analogy based on the wave-operator of irrotational flow, taking into account only the vortex sound source contributions. The fluctuating turbulent quantities are computed with the FRPM-model described in the previous sections. For the CAA simulations the steady RANS solution is used to prescribe the mean-flow.

## 3.8 Source term formulations

Eq. (77) gives the vortex sound source term needed to be modeled. The non-linear term $III$ can be considered smaller than the linear terms $I$ and $II$. The source term Eq. (77) is in general composed out of a rotational part defined by $\nabla \times \boldsymbol{q}_m \neq 0$, and an irrotational part defined by $\nabla \cdot \boldsymbol{q}_m \neq 0$. Sound sources of free turbulence are defined by the irrotational part whereas the rotational part is primarily responsible for the generation of vorticity, which can be seen by taking the curl of the APE momentum equation yielding

$$\frac{\partial \boldsymbol{\omega}'}{\partial t} = \boldsymbol{\nabla} \times \boldsymbol{q_m}. \tag{79}$$

This shows that the induced vorticity on the left-hand side is entirely defined by the rotational part of the momentum source. The approach has the advantage that the actual dynamics of the induced vorticity closely matches those prescribed by the right-hand side source term. With a propagation model based on e.g. the linearized Euler equations (LEE) this is not necessarily the case, since partly vortex dynamics are directly resolved by the propagation equations and partly induced by the source. It may occur that the effectively forced vorticity does not exactly follow the behavior as expected to be induced by the source term. One essential difference that appears in comparison with traditional acoustic analogy is due to the fact that the source term induces not only acoustic modes but also vorticity mode contributions. Sound is generated as part of the acoustic simulation process due to the interaction of the airframe with the vorticity induced by the source term. This is e.g. different to other statistical airframe noise approaches which rely on the availability of a surface pressure spectrum. A vorticity based source model gives a more direct connection with turbulence properties and the generated sound.

It is well known that free turbulence generates a sound intensity following an eight power law, whereas airframe sound generation scales with a somewhat smaller, i.e., fifth power law. Hence, for small Mach numbers, the airframe noise mechanism is clearly dominating over the sound generation process of free turbulence. This means that for

airframe noise simulation the rotational part of the momentum source term is the most important contribution. Furthermore, the nonlinear part of the Lamb vector source term Eq. (77) (i.e. term $III$) is less important than the linear contribution and can be neglected in favor of the linear contributions given by terms $I$ and $II$. Acoustic arguments that the linear terms are acoustical inefficient compared to the non-linear terms in free turbulence (i.e. acoustic mode contributions are dominated in this particular case by the non-linear term $III$) don't apply in this case where the source term acts primarily as a vorticity source term. Indeed, vortex generation is dominated by terms $I$ and $II$.

### 3.8.1 Source term A

The Lamb vector source term Eq. (77) can be realized based on a realization of fluctuating velocity or vorticity, respectively. We will refer to the approach based on modeling fluctuating velocity subsequently as 'Source A' approach. Next this approach is discussed in more detail.

The linear part of the Lamb vector as defined by terms $I$ and term $II$ in Eq. (77), respectively, can be modeled with FRPM in 3-D by generating three independent realizations $\psi_i$, $i = 1 \dots 3$ by means of three independent random variables $r_{ik}$ associated to the $k = 1 \dots N$ random particles in Eq. (118). These variables are taken as the three components of a vector potential which defines fluctuating velocity components of synthetic turbulence via

$$v_i' = \epsilon_{ijk} \frac{\partial \psi_k}{\partial x_j}. \tag{80}$$

Here, $\epsilon_{ijk}$ is the Levi-Chivita symbol and the summation convention is applied to all products of same index. Due to this definition, the fluctuating velocities are solenoidal (divergence free). Fluctuating vorticity is obtained taking the curl of the such derived fluctuating velocities. The derivative with respect to $x_j$ in Eq. (80) effectively means to use a differentiated filter kernel in Eq. (118). It is possible to generated with this procedure a 3-D fluctuating velocity field on a 2-D slice defined by a 2-D auxiliary FRPM mesh using an appropriate scaling for the components $\hat{A}_i$. For more details of this procedure refer to(Ewert et al., 2011). In the Source A model the variance of the generated velocity fluctuations is prescribed by the local RANS turbulence kinetic energy, i.e.

$$\langle v_i'^2 \rangle = 2k. \tag{81}$$

This approach generates isotropic fluctuations with $\langle v_1^2 \rangle = \langle v_2^2 \rangle = \langle v_3^2 \rangle$. An extension to anisotropic velocity fluctuations is not applied here.

The locally realized longitudinal length scale is matched to the turbulence length scale from RANS, i.e.

$$l_s = \frac{c_l}{C_\mu} \frac{\sqrt{k}}{\omega} \tag{82}$$

Here $C_\mu \cong 0.09$ and

$$c_l \approx 0.54. \tag{83}$$

The procedure as outlined before has been applied for all 2-D Source A computations presented hereafter.

### 3.8.2 Source term B

The vorticity in term $II$ can be modeled directly by FRPM. In 2-D a scalar quantity generated by FRPM can be interpreted as the third component of fluctuating vorticity ($\omega_3'$). In 3-D a vector with three independent realizations is generated and interpreted as $\boldsymbol{\omega}'$. Based on findings from Source A simulations, we assume that the contribution of term $I$ has less importance than term $II$ and model only term $I$, i.e. $q_m = -\boldsymbol{\omega}' \times \boldsymbol{u_0}$. The relative unimportance of term $I$ compared to term $II$ was reported in(Ewert et al., 2011). Subsequently we will denoted a source term based on modeled fluctuating vorticity as 'Source B' approach.

For the Source B formulation the variance of the fluctuating quantity provided by FRPM has to be matched to the variance of vorticity in the turbulent flow. From dimensional reasoning the vorticity variance must scale according to

$$\left\langle \omega'^2 \right\rangle = c_\omega \frac{k}{l_\omega^2}, \tag{84}$$

where $k$ is the turbulence kinetic energy from RANS. Furthermore, the length scale $l_\omega$ in Eq. (84) is related to the Taylor micro scale $\lambda_f$, which according to Taylor may be roughly be regarded as a measure of the diameter of the smallest eddies which are responsible for the dissipation of the energy. However, the FRPM generated spectra can be deemed to represent a truncated part of the full turbulent spectrum, i.e. including the sound generated by the most energetic part of the turbulent spectrum by omitting high-frequency contribution of smaller turbulence. Hence, the generated Gaussian spectrum could be seen as a model to describe a truncated full turbulent spectrum for which the length scale $l_\omega$ would be associated to the cut-off wave length actually applied. Since the cut-off wave length is associated to the mesh resolution, we use throughout this work a globally constant length scale $l_\omega = l_{min}$, which is defined by the largest mesh resolution in the source domain. A truncation of the velocity spectrum means also a reduction of the effectively resolved turbulence kinetic energy, which must be accounted for in the calibration constant $c_\omega$ in Eq. (84). The length scale $l_\omega$ is also used as the integral length scale of vorticity (filter kernel width) in the FRPM realization of fluctuating vorticity.

### 3.8.3 2D to 3D correction

For 2D predictions the spanwise coherence has to be explicitly taken into account by a 2D to 3D correction step to approximately predict a 3D spectrum. The 2D to 3D procedure introduced in(Ewert et al., 2009) reveals that the shape for 2D and 3D spectra is maintained (i.e. the 2D to 3D correction is not frequency dependent). The formula to get the 3D SPL from a 2D SPL is as follows:

$$SPL_{3D} = SPL_{2D} + 10log\left(\frac{C}{2\pi}\frac{L}{R}Ma\right) \tag{85}$$

with $C = 1.4$, the span $L$ and R as observer distance.

## 3.9 Future developments

### 3.9.1 State-of-the-art of FRPM trailing-edge noise

The modeling of broadband noise sources with stochastic methods has a clear benefit over fully turbulent resolving methods, if the underlying averaged turbulent flow statistics are well described by Reynolds Averaged Navier-Stokes (RANS) CFD simulation and the flow problem exhibits a specific symmetry that allows to reduce the dimension of the simulation by one, e.g. for the simulation of airfoil trailing edge noise. Although the underlying unsteady turbulent flow inevitably requires the setup as a 3-D simulation problem, the Reynolds Averaged flow problem exhibits homogeneity in the spanwise direction, that is well predictable by 2-D RANS simulation. Furthermore, the reconstruction of turbulent velocity related broadband noise sources can be also done in a 2-D setup, if a proper 2D-to-3D scaling is applied. For trailing edge noise, the FRPM realization represents the velocity fluctuations for a slice through the computational domain, and the correction formula accounts for the frequency dependent spanwise correlation length of the noise source, expressed by an additional model for the spanwise coherence as put forward by the model in the previous paragraph.

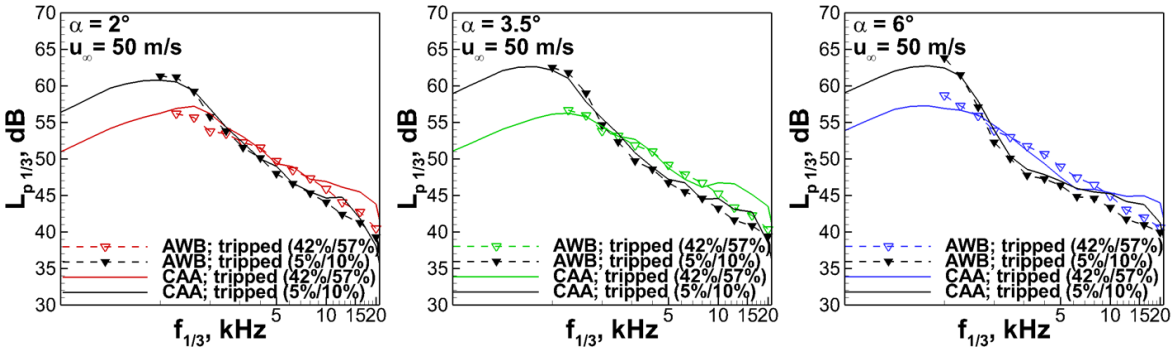



Figure 18: Comparison of measured (triangles) and predicted one-third octave trailing edge noise spectra and simulations (solid lines) for two different trippings applied to the pressure- and suction side of a RoH-W-18%c37 wind turbine airfoil at three angles of attack; red color coding, tripping at 42% and 57% on the pressure- and suction sides; black color coding, tripping at 5% and 10%; angle of attack of 2°, left; 3.5°, center; 6°, right,(Herr et al., 2018).

How well predictions based on this procedure predicting broadband trailing edge noise (TEN) is revealed by Fig. 18, which shows a cross-comparison of the simulated and measured TEN spectra involving different tripping positions applied on the pressure and suction sides. A picture of the experimental setup is shown in Fig. 19. Clearly different one-third octave spectra are obtained for two tripping scenarios for a RoH-W-18%c37 airfoil case at selected three different angles of attack. Here, the combination of tripping at 42% and 57% on the pressure- and suction sides, respectively, is indicated with red triangles for the measurement and for a more upstream tripping at positions 5% and 10% with black solid triangles. 2D simulations based on thre previously sketched FRPM approach with further 2D-to-3D corrections are shown as colored solid lines. Very good agreement can be confirmed. Further details can be found in Herr et al. (Herr et al., 2018).

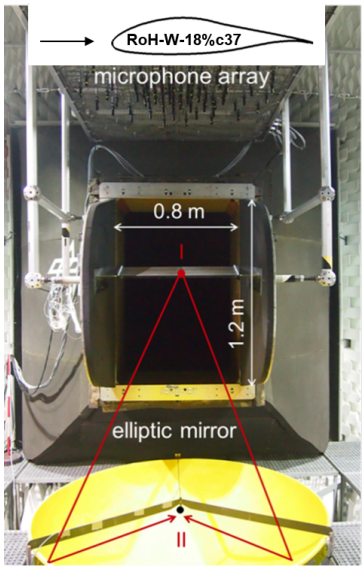



Figure 19: Windtunnel setup of RoH-W-18%c37 wind turbine airfoil.

A reduction by one order of magnitude has been also accomplished in the modeling of jet-noise using a primal time-domain realization of the Tam & Auriault jet mixing noise model with FRPM. The model was further successfully extended to the simulation of combustion noise.

Using Gaussian transforms, a wide range of different generic turbulence spectra can be accomplished through the superposition of Gaussian spectra of different length scale as generated by the generic FRPM procedure (Wohlbrandt et al., 2016; Reiche et al., 2016; Uhl et al., 2023).

## 3.10 Aeroacoustic Optimization

The modeling of turbulence related sound sources using synthetic turbulence has the potential to provide a physics informed fast prediction approach for aeroacoustics optimization.

The simulation of aerodynamically generated sound by means of mesoscopic or macroscopic scale resolving methods, e.g. using Wall Modeled Large Eddy Simulation (WM-LES) and subsequent/simultaneous far-field propagation with the Ffowcs-Williams Hawkings (FW-H) surface integral method, has reached a high level of maturity. However, for typical technical applications WM-LES still requires computational turnaround times of the order of 10 kCore·h and beyond. They therefore have to be combined with appropriate surrogate modeling for sophisticated interpolation to be usable in optimization workflows.

In an industrial context, turnaround times smaller than 50-100 Core·h often define an upper threshold of usability for optimization. Such a limit could be reached with Reynolds Averaged Navier-Stokes (RANS) simulation alone. In conjunction with 2D CAA simulation, simulation times of similar order can be accomplished. First promising results have been reported (Lim et al., 2022).

However, realistic technical problems such as the sound generated and radiated from a landing gear require on the CAA and the CFD side for 3D simulations. While the

required short simulation times can be accomplished on the CFD side, the question arises whether the time accurate modeling of synthetic turbulence in 3D still offers computational performance benefits, e.g. in comparison with wall modelled LES. In deed, spatial resolution requirements in the aeroacoustic source region are comparable for WM-LES and for synthetic turbulence generation as the scales responsible for the major sound generating contributions must be captured equally well by both approaches.

Furthermore, it is questionable whether isotropic models for synthetic turbulence can capture the more complex highly anistropic features in the main turbulence producing regime. For this reason, in recent work the focus is on the realization of synthetic turbulence by means of forced linear advection-diffuion-dissipation models (FLAD) for the realization of anisotropic synthetic turbulence (Ewert, 2016). In this models, the crucial turbulence production mechanisms are directly resolved as in scale resolving simulation, while the stochastic forcing actually is a model of the energy re-distribution otherwise accomplished by the non-linear part of the convective terms.

Linear transport equations can be realized with fast simple second order transport equation numerics very efficiently. The computational efficiency can be demonstrated to be about 3 times better compared to a LBM streaming and collision step. Furthermore, these linear transport equation models are based on a convective time scale, not on a compressible time scale. For subsonic problem, the overall benefit can be estimated to yield one order of magnitude. Additional significant savings come form the fact that for the modeling of a specific noise source region only a reduced computational domain is required (e.g. restricted to the vicinity of a landing gear), while the other flow part is obtained from a RANS CFD simulation of the entire domain (e.g. an entire transport aircraft). In total, synthetic turbulence offers the potential to predict also 3D sound sources about two orders of magnitude faster than stat-of-the-art LBM methods and therefore have some potential for 3D aeroacoustics optimization. Some recent developments are briefly sketched in the next paragraphs.

### 3.10.1 APE-vortical velocity equation split of LEE

Helmholtz decomposition can be used to accomplish a hydrodynamic-acoustic splitting of the Navier-Stokes equation into incompressible flow equations and acoustic propagation equations (Ewert and Kreuzinger, 2021). The major acoustic source term found that way is based on the fluctuating incompressible pressure defined by the flow equation. Attempts are underway to use this source term as an acoustic metric to characterize acoustic sound generation from near field data (Uhl et al., 2023). The incompressible pressure in general requires solution of a Poisson equation.

Here, we consider a slightly modified decomposition to obtain a split equation system that will give an alternative source term that can be computed without the need to solve a Poisson problem. A specific dilatation based cross-coupling term can be identified as a purely acoustic source term, which is employed as a suitable near-field metric to characterize vortex sound generation.

To proceed along this line, we start referring to the LEE (Eq. 26 and Eq. 27), in

cartesian tensor notation given in the form

$$\frac{\partial p'}{\partial t} + \bar{u}_j \frac{\partial p'}{\partial x_j} + u'_j \frac{\partial \bar{p}}{\partial x_j} + \gamma \bar{p} \frac{\partial u'_j}{\partial x_j} + \gamma p' \frac{\partial \bar{u}_j}{\partial x_j} = 0 \tag{86}$$

$$\frac{\partial u'_i}{\partial t} + \bar{u}_j \frac{\partial u'_i}{\partial x_j} + \underbrace{u'_j \frac{\partial \bar{u}_i}{\partial x_j}}_{(I)} + \underbrace{\frac{\partial}{\partial x_i}\left(\frac{p'}{\bar{\rho}}\right)}_{(IV)} = f'_i. \tag{87}$$

Here, $u'_i(\boldsymbol{x}, t)$ and $p'(\boldsymbol{x}, t)$ denote compressible velocity and pressure fluctuations, whereas $\bar{u}_i(\boldsymbol{x})$, $\bar{\rho}(\boldsymbol{x})$, and $\bar{p}(\boldsymbol{x})$ indicate steady but in general non-uniform mean-flow fields for flow and pressure. Entropy fluctuations are neglected by assuming an isentropic relation to hold for pressure and density fluctuations, $p' = c^2 \rho'$, where $c = \sqrt{\gamma \bar{p}/\bar{\rho}}$ with $\gamma = 1.4$ denotes the constant speed of sound. Furthermore, a mean-flow satisfying the steady Euler equations obeys

$$\frac{\partial \bar{p}}{\partial x_i} = c^2 \frac{\partial \bar{\rho}}{\partial x_i} \tag{88}$$

for thermally and calorical ideal gas. This allows to reformulate the pressure term into the form $(IV)$ shown in Eq. (87), so that the LEE continuity equations decouples from the energy (pressure) and momentum equations. Although derived by linearizing the Euler equations, a formally identical set of equations is obtained from the Navier-Stokes equations in primitive disturbance form over RANS mean-flow (Ewert et al., 2014) by neglecting non-linear terms and fluctuating viscous terms and taking into account that Eq. (88) also holds for subsonic RANS mean-flow where viscous and dissipation terms can be neglected in the energy equation. Note, the LEE in the form given above comprise acoustic and vorticity modes.

The linearized Euler equations in the form given by Eqs. (86) and (87) above can be split up further into Acoustic Perturbation Equations (APE) and linear equations for the split velocity fluctuations that governs vorticity transport.

The velocity decomposition is the one used in the work of Goldstein (Goldstein, 1978), Golubev & Atassi (Golubev and Atassi, 1998), Cooper & Peake (Cooper and Peake, 2001). The perturbation velocity $\boldsymbol{u}'$ is split up into an irrotational (acoustic) part $\boldsymbol{u}^a = \boldsymbol{\nabla}\varphi$ plus a residual part $\boldsymbol{u}^r$ that contains the complete vorticity,

$$\boldsymbol{u}' = \boldsymbol{\nabla}\varphi + \boldsymbol{u}^r. \tag{89}$$

Different to Helmholtz decomposition, where the velocity field would contain an irrotational and a divergence-free (solenoidal) part, $\boldsymbol{u}' = \boldsymbol{\nabla}\phi + \boldsymbol{\nabla} \times \boldsymbol{A}$, $\boldsymbol{\nabla} \cdot (\boldsymbol{\nabla} \times \boldsymbol{A}) = 0$, the residual part of Eq. (89) in general is not divergence free, i.e., comprises irrotational components, $\boldsymbol{\nabla} \cdot \boldsymbol{u}^r \neq 0$.

However, fluctuating vorticity $\boldsymbol{\omega}' := \boldsymbol{\nabla} \times \boldsymbol{u}'$ is entirely described by the residual velocity term of Eq. (89), since $\boldsymbol{\nabla} \times \boldsymbol{u}' = \boldsymbol{\nabla} \times \boldsymbol{u}^r = \boldsymbol{\omega}'$.

For Helmholtz decomposition the irrotational and divergence-free constraint provides two governing equations for the two split components. To complete Eq. (89) we need an additional equation to complete the split definition. Therefore, we define the $\varphi$ to represent a generalized acoustic potential for the general flow case and require it to specify also the fluctuating pressure by means of a flow dependent substantial time derivative,

$$p' = -\bar{\rho} \frac{\bar{D}\varphi}{Dt}. \tag{90}$$

Introducing the variable decomposition Eq. (89) with Eq. (90) into the LEE as given by Eqs. (86) and (87) yields the split set of equations:

$$\frac{\partial p'}{\partial t} + c^2 \frac{\partial}{\partial x_i}\left(\frac{p'}{c^2}\bar{u}_i + \bar{\rho} u_i^a\right) = -c^2 \frac{\partial}{\partial x_i}\left(\bar{\rho} u_i^r\right) \tag{91}$$

$$\frac{\partial u_i^a}{\partial t} + \frac{\partial}{\partial x_i}\left(\bar{u}_j u_j^a + \frac{p'}{\bar{\rho}}\right) = 0 \tag{92}$$

$$\frac{\partial u_i^r}{\partial t} + \bar{u}_j \frac{\partial u_i^r}{\partial x_j} + \underbrace{u_j^r \frac{\partial \bar{u}_i}{\partial x_j}}_{(I)} = -\epsilon_{ijk} \bar{\omega}_j u_k^a + f_i' \tag{93}$$

Here, Eqs. (91) and (92) represent the acoustic perturbation equations (APE), and Eq. (93) is the split equations for the vorticity mode. Thereby the APE momentum equation Eq. (92) follows from taking the gradient of Eq. (90). The general LEE forcing terms appears unmodified on the right-hand side of the vortical flow equation. The split equation system has been already used to simulate installed rotor noise with a Discontinuous Galerkin method (Franco et al., 2022).

Two cross-coupling terms are present. In Eq. (93) the curl of mean vorticity with the acoustic particle velocity represents the feedback from the acoustics to the flow. It complies with the feedback term found in Ref. (Ewert and Kreuzinger, 2021). It is only present in rotational mean flows.

In addition, a cross coupling term occurs on the right-hand side of the APE pressure equation, which is defined by the dilatation of the vortical velocity $\boldsymbol{u}^r$.

### 3.10.2 Turbulent Inflow Forcing

The Fast Random Particle-Mesh (FRPM) method has been successfully applied also for turbulent inflow seeding for purely acoustic purposes but also in the framework of scale resolving simulation. Turbulent velocity fluctuations are generated and seeded into the linearized Euler Equations (LEE) using an Eddy Relaxation Term (ERT) on the right-hand side of the momentum equation (Ewert et al., 2014),

$$f_i' = -\epsilon_{ijk} \frac{\partial}{\partial x_j}\left[\sigma\left(\omega_k' - \omega_k^{ref}\right)\right], \tag{94}$$

which is applied in a certain inflow volume (inflow forcing patch), refer to the sketch shown in Fig. 20. Here, $\omega_i' := \epsilon_{ijk}\partial u_k'/\partial x_j$ denotes the fluctuating vorticity and $\omega_k^{ref} := \epsilon_{ijk}\partial u_k^{ref}/\partial x_j$ is the vorticity related to the stochastically generated velocity on the inflow forcing patch.

This specific form realizes a mode selective relaxation source term to impose vorticity fluctuations of well defined level and characteristics into the simulation domain while simultaneously being transparent to acoustic waves passing through, refer e.g. to the discussion in Refs. (Ewert et al., 2014; Akkermans et al., 2018).

The source term has been successfully applied to simulate airframe noise mechanism with the LEE with ERT based sound sources but also has proven to be a valuable method

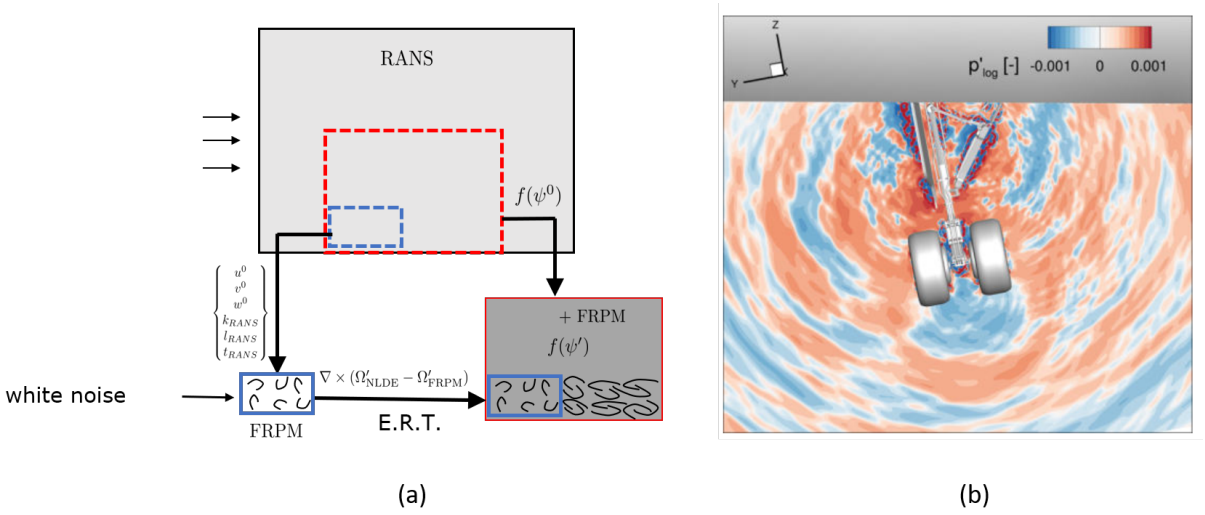



Figure 20: (a) FRPM inflow turbulence forcing via eddy relaxation term (ERT); the LEE simulation domain (red box) is a sub-domain of the larger RANS domain; inflow-forcing is applied in the blue box utilizing RANS informations; (b) LEE sound field at fully dressed landing gear with FRPM-ERT forcing.

to silently seed inflow turbulence in direct noise computations and scale resolving simulation, e.g. refer to (Ananthan et al., 2022; Akkermans et al., 2018). Furthermore, it has been successfully applied to model turbulent backscatter (Ewert et al., 2017).

The forcing term relaxes or nudges the actual fluctuating velocity solution towards a vorticity reference solution as specified by the stochastic source model, whereby the size of relaxation parameter $\sigma$ defines closeness of coupling of the resolved fluctuating vorticity with target values.

The part of the eddy relaxation term depending on fluctuating vorticity can be shown for small Mach numbers where $\boldsymbol{\nabla} \cdot \boldsymbol{u}' =$ and with constant $\sigma$ to take on the form of a viscous term (using nabla notation),

$$-\boldsymbol{\nabla} \times (\sigma \boldsymbol{\nabla} \times \boldsymbol{u}') \overset{M \to 0}{\to} \sigma \boldsymbol{\nabla}^2 \boldsymbol{u}', \tag{95}$$

where $\sigma$ represents viscosity, refer to the discussion in (Neifeld and Ewert, 2018). Replacing $\sigma$ with a (non-constant ) subgrid scale viscosity, the left-hand side term has been proposed and successfully applied as a vector force model for the divergence of shear-stresses (Dantinne et al., 1998).

On these grounds, by using the eddy-viscosity from RANS to define the relaxation parameter, $\sigma = \nu_t$, the fluctuating vorticity term in the ERT forcing provides a close approximation to the viscous term that arises in the linearized Navier-Stokes (LNS) equations as a model for fluctuating Reynolds stresses.

In conjunction with the stochastic forcing part, the entire forcing term therefore could be deemed to represent a proper model for the actual forcing term given in low subsonic flow. Especially, the non-linear term will not only act as an additional diffusion/viscous term as modeled by an effective eddy viscosity model in RANS. It further accomplishes a redistribution of fluctuations between different wave-numbers that must be suitably reproduced if modeled in a time dependent model equation for velocity fluctuations. With

a $\nu_t$-based eddy relaxation term this is accomplished simply through augmenting the energetically dissipative effect of the viscous-term-like part of the forcing term with an equally strong forcing term (the second part of the ERT term) that exactly replenishes the removed contributions. The spectral shape of the forcing term then models the spectral redistribtion accomplished by the non-linear energy redistribution term.

Occasionally the imposed reference solution might not comply with some other dynamics as resolved by the linear equations. For example, the forcing vorticity might not satisfy a divergence-free constraint, otherwise always satisfied by the resolved fluctuating vorticity $\boldsymbol{\omega}' = \boldsymbol{\nabla} \times \boldsymbol{u}' \rightarrow \boldsymbol{\nabla} \cdot \boldsymbol{\omega}' = 0$.

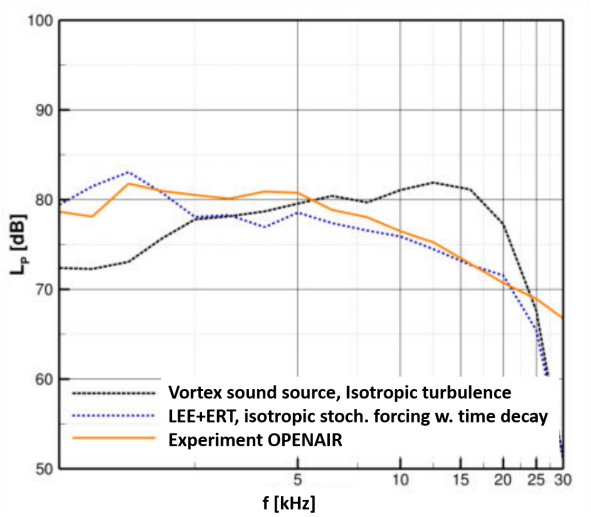



Figure 21: One-third octave spectrum for fully dressed landing gear simulation LEE+ERT and comparison with wind tunnel measurement (Ehlert, 2022).

It was observed that the resolved fluctuations will obey the forcing solution in a 'least-square sense', i.e. as close as possible but not giving up key dynamics as imposed by the governing equations. It was conjectured that this improves the modeling of synthetic turbulence and the associated quality of sound generation. For example, a reference solution derived from isotropic synthetic turbulence models is found to become slightly readjusted to acccount for anisotropic flow dynamics from the linearized flow equations in non-uniform flow. Indeed, better sound source trends could be found for challenging flow problems using LEE with ERT and isotropic turbulence, whereas vortex source terms, e.g. based on Lamb's vector directly derived from isotropic synthetic turbulence, failed to reproduce correct trends. For example, Fig. 21 shows the sound spectra for a fully dressed landing gear obtained with ERT forcing (for the sound field see also Fig. 20(b)) that resembles close agreement in the resolved frequency range with measurements in the AWB acoustic wind tunnel at DLR Braunschweig.

In subsection 3.11 these somewhat loose arguments–that the ERT provide an improvement of synthetic turbulence even if used with isotropic turbulence in the underlying stochastic forcing model–will be put on more firm grounds by demonstrating that the linearized Euler equations with eddy-relaxation source term (LEE+ERT) to be equivalent to an acoustic propagation model driven by a source term from a forced linear advection-dissipation equations (APE+FLAD). The forced linear advection-dissipation

equation was proposed in Ref. (Ewert, 2016) as a stochastic partial differential equation that realizes synthetic turbulence in closest possible compliance with the RANS turbulence statistics and as such is intended to give better results as e.g. obtained from a model of isotropic turbulence applied all over the source region. The improvements seen from LEE+ERT applications therefore provide direct evidence for that conjecture. Furthermore, the stochastic FLAD forcing must have a specific spectral color to provide meaningful turbulence spectra. Any experience of FLAD modeling therefore can be directly use to improve the LEE+ERT forcing as well.

Lastly, this somewhat surprising finding paves way for immediate realization of a FLAD transport equation based on already existing numerics as being demonstrated in this paper.

## 3.11 Forced linear advection diffusion equation

Improved modeling of RANS informed synthetic turbulence was proposed in Ref. (Ewert, 2016) in terms of a stochastically forced linear advection-diffusion-dissipation (FLAD$^2$) equation. Starting from the fluctuation equations that governs turbulence, it can be rearranged to provide the exact but unclosed equation for turbulence kinetic energy $k_t := \overline{u_i^2}$, refer to Fig. 22(a) (for stationary turbulence problems as assumed here ensemble and time averaging are interchangeable).

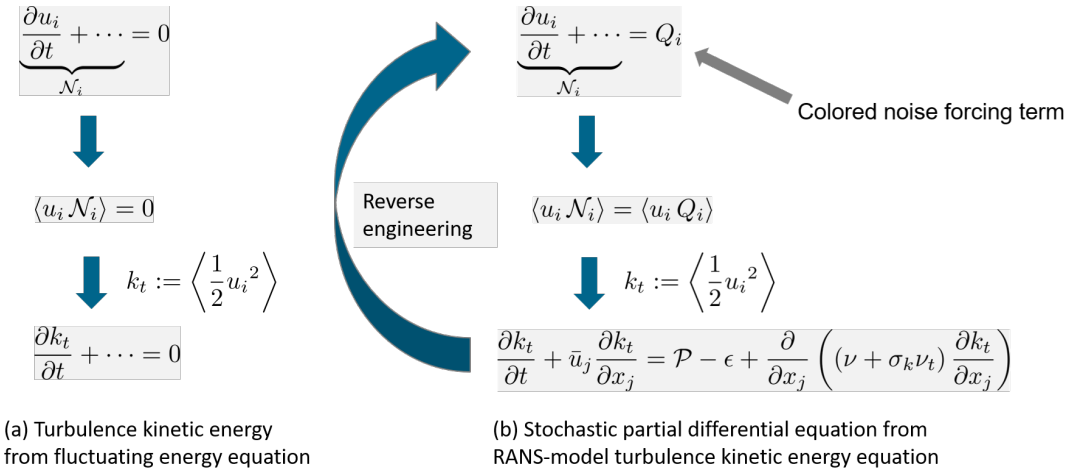



Figure 22: (a) Exact turbulence kinetic energy equation from fluctuating velocity equation; (b) stochastic partial differential equation from simplified RANS turbulent kinetic energy transport equation and reverse-engineered fluctuating velocity equation with colored stochastic forcing term to model redistribution of fluctuations in wave-number space.

In RANS modeling a closed turbulence kinetic energy (TKE) equation is approximated by an advection-diffusion-dissipation equation, refer to Fig. 22(b). Reversely to the previous steps, a proper fluctuating velocity equation can be found from the RANS TKE equation, Fig. 22(b). The resulting forced linear advection-diffusion equation consists of a stochastic forcing term on the right-hand side that realizes properly scaled colored noise. The forcing term represents an additive noise source that - unlike multiplicative noise - does not pose any subtle mathematical problems (Kloeden and Platen, 2013). Additive

noise, e.g., has been widely used in renormalization theory to study homogeneous isotropic turbulence by means of a forced linear equation with colored noise source term.

The resulting stochastic partial differential FLAD equations incorporates RANS variables (linear flow, turbulent viscosity) and as such exactly reproduces the RANS TKE equation. In that and only that form it represents a synthetic turbulence twin to the TKE equation.

To summarize some modifications to the method as initially outlined in Ref. (Ewert, 2016), properly scaled colored rather than white noise has to be used. Furthermore, dissipation is not explicitly accounted for anymore by an explicit term in the model equation but rather eventually results in the TKE equation by means of the molecular viscosity in the FLAD diffusion term[1]. Also, turbulent production and re-distribution comes directly from the now included mean-shear term.

Stochastic forcing therefore is not needed to model turbulence production but rather balances the extra dissipation inevitably coming from the eddy viscosity in the FLAD diffusive term that otherwise is needed to realize the proper diffusive term in the target RANS TKE equation. That way the stochastic forcing models the redistribution of fluctuations in wave number space caused. The spectrum of forcing can be found by requiring it to provide a proper model spectrum for homogeneous isotropic turbulence.

In previous work it was conjectured that the resulting length scale of synthetic turbulence is defined by the eddy-viscosity used in the diffusive term and turbulence time scale from an explicit dissipation term, $l \propto \sqrt{\nu_t \tau}$, $\tau = k_t/\epsilon$. However, in the mean time it was found from semi-analytical analysis that the time scale can be also provided by a Langevin model equation with time scale $\tau$ used in the FLAD forcing that allows to skip the explicit dissipation term. The spectra derived from semi-analytical analysis by integrating the theroretical wave-number spectra numerically exhibit an even more robust reproduction of turbulence spectra, refer to Fig. 23.

There, a uniform non-dimensional velocity $u$ is assumed in $x$-direction. 1-D turbulence spectra are computed from 3-D turbulence. The parameter $\alpha = u\tau/l$ specifies the ratio of decay time to a convection time defined by the ratio of realized non-dimensional integral length scale $l$ and convection velocity $u$. A time scale $\tau = \alpha l/u$ following from this definition is used as the time-scale parameter in the Langevin equation. The length scale is defined by the square root of an effective eddy-viscosity used in the model equation and the time scale, $l = \sqrt{\nu^* \tau}$. Hence, the given set of parameters implicitly specifies the effective eddy viscosity to be $\nu^* = lu/\alpha$. Lastly, the quantity $lsrc$ specifies the spatial correlation length of the Langevin forcing. The resulting spectra reveal the characteristic shape of a 1-D turbulence spectral with plateau and later drop off. Based on the chosen colored forcing the drop-off complies with a factor 6/3 power law (i.e. realizes a Liepmann spectrum), refer to the reference spectrum. While $l$ and $u$ are kept constant, $\alpha$ is varied over a larger parameter range (implying changes in eddy viscosity and time scale). However, all resulting spectra collapse very well in the resolved regime, which indicates the fundamental length scale scaling $l = \sqrt{\nu^* \tau}$ to hold.

[1]That way one 'D' of the terminology 'FLADD' used in Ref. (Ewert, 2016) got lost.

## 3.12 APE + FLAD = LEE + ERT

To show the FLAD type of equation realized by the split equation Eq. (93), the eddy relaxation source term Eq. (94) has to be used as a forcing term in the split equation. Taking into account that the ERT part from resolved fluctuations well approximates a viscous term and using $\sigma = \nu + \sigma_k \nu_t$ as relaxation parameter ($\sigma_k \simeq 0.85 \ldots 1$), the characteristic FLAD form is obtained (bearing in mind $\boldsymbol{\nabla} \times (\sigma \boldsymbol{\nabla} \times \boldsymbol{u}') \simeq \boldsymbol{\nabla} \cdot (\sigma \boldsymbol{\nabla} \boldsymbol{u}')$),

$$\frac{\partial \boldsymbol{u}^r}{\partial t} + (\bar{\boldsymbol{u}} \cdot \boldsymbol{\nabla})\, \boldsymbol{u}^r + (\boldsymbol{u}^r \cdot \boldsymbol{\nabla})\, \bar{\boldsymbol{u}} + \boldsymbol{\nabla} \times \left[ (\nu + \sigma_k \nu_t)\, (\boldsymbol{\nabla} \times \boldsymbol{u}^r) \right] = \boldsymbol{\nabla} \times \left[ (\nu + \sigma_k \nu_t) \left( \boldsymbol{\nabla} \times \boldsymbol{u}^{ref} \right) \right]. \tag{96}$$

From this the proper generic RANS TKE equation derives,

$$\frac{\partial k_t}{\partial t} + (\bar{\boldsymbol{u}} \cdot \boldsymbol{\nabla})\, k_t - \boldsymbol{\nabla} \cdot \left[ (\nu + \sigma_k \nu_t)\, \boldsymbol{\nabla} k_t \right] = \underbrace{\mathcal{P}}_{\text{prod. MGT}} - \underbrace{\epsilon}_{\text{time decay } (\nu)} + \underbrace{\underbrace{\mathcal{P}^*}_{\text{prod. forcing}} - \underbrace{\epsilon^*}_{\text{time decay } (\nu_t)}}_{\sum \simeq 0}. \tag{97}$$

Colors in both equations indicate links between FLAD and resulting TKE terms. Molecular viscosity causes the expected dissipation $\epsilon$. The mean-shear term in magenta (Mean-Flow Gradient, MGT) yields the turbulence production in the TKE equation. The blue term in Eq. (96) specifies the turbulent forcing from the eddy relaxation term. The formulation as a relaxation term by construction ensures that the turbulence production from forcing balances in magnitude the turbulent dissipation from eddy viscosity, $\mathcal{P}^* - \epsilon* \simeq 0$, and provides the right source strength if $\boldsymbol{u}^{ref}$ if taken from a synthetic turbulence model for velocity.

An exact implementation of the viscous terms would be also possible. However, on the one hand, the realization via ERT is chosen here as it is already implemented so that the FLAD transport equation can be made operation with minor implementation effort with existing numerics. Secondly, the exact source term will induce non-divergence free components that give rise to additional noise source contributions in the source term Eq. (94) that could be spurious as being caused by the numerical model introduced. Usage of ERT ensures that no such spurious noise sources are generated at all.

The split equation formulation discussed above gives the possibility to derive the essential acoustic metric from near field data of standalone simulation. Formally, a split set of equations based on the APE Eqs. (91) and (92) acoustic propagation and the FLAD model equation for synthetic turbulence Eq. (96) separates the turbulence model equation from the physical propagation equation, similar to RANS CFD, where physical Reynolds equations for the flow are augmented by turbulent transport equations as approximate closure models.

## 3.13 Boundary conditions of split equations

Solid wall boundary conditions are realized in the LEE with mean-flow by RANS by imposing the condition $\partial p'/\partial n \simeq 0$ at the wall. RANS mean flow satisfies a no-slip condition at the wall. Also extrapolated RANS slip velocities could be used but their implication is not discussed here. This automatically will give a kinematic slip condition

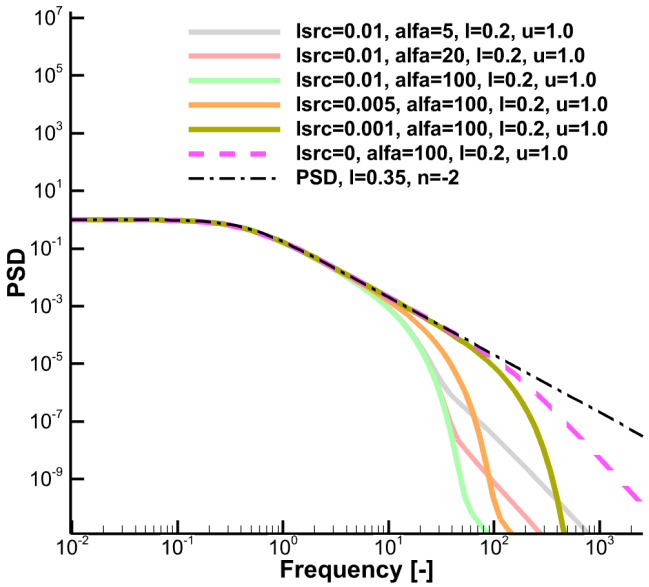



Figure 23: Semi-analytical results for resulting 1-D turbulence spectra from FLAD with Langevin forcing; the parameters are explained in the body of the text.

for the fluctuating velocity at the wall, $\boldsymbol{u}' \cdot \boldsymbol{n} = 0$ if the LEE momentum equation is solved down to the wall [2].

In the split APEs the same boundary condition is applied for the pressure gradients at the wall. Note, in the current split system $p'$ is identical to the LEE quantity and therefore the LEE wall gradient still has to be applied. Under the given constraints this also leads to a kinematic slip condition for the APE velocity $\boldsymbol{u}^a \cdot \boldsymbol{n} = 0$. Consequently, the vortical velocity component must satisfy $\boldsymbol{u}^r \cdot \boldsymbol{n} = (\boldsymbol{u}' - \boldsymbol{u}^a) \cdot \boldsymbol{n} = 0$ at the wall. This is imposed e.g. using the immersed boundary method (IBM) in `PIANO-IBM`. At in- and outflow boundaries simple convection conditions are applied for the vortical velocity equation.[3]

[2]Further possible residual drift effects are corrected for on top in the actual BC.

[3]Hydrodynamic acoustic splitting studies have shown that a hydrodynamic pressure that obeys a boundary condition $\partial P/\partial n = 0$ must be included in a model equation for synthetic turbulence to enforce leading-edge noise of vortex-airfoil interaction noise. However, the LEE can resolve vortex-airfoil interaction noise and so must do the equivalent APE-based split equation system, where Eq. (93) is a velocity transport equation excluding pressure, i.e. leading edge noise must also be generated by transport equations without pressure term. The difference between HAS and the splitting approach discussed in this paper lies in the application of a proper vortical velocity wall boundary conditions in Eq. (93) that in the other case is enforced by the incompressible pressure.

# 4 Model Validation

The approach proposed was validated in the context of ENODISE with the experiments conducted for configurations A1 (Zaman et al., 2023a), A2 (Zaman et al., 2023b) and B1 (do Nascimento Monteiro et al., 2023). In Configuration A1, a two-bladed propeller is operated at different RPMs, and at different tip-gap distances relatively to a flat plate. In Configuration A2, the same two-blade propeller is operated at different RPMs, and at different tip-gap distances relatively to an S-shaped plate. In Configuration B1, one and three six-blades leading-edge-placed propellers are operated at different RPMs, and at different relative rotation phase angles. In all configurations, the AD-based rotor model was considered, without the addition of the thickness noise source, since the propellers operate at low blade-tip Mach number.

## 4.1 Configuration A1

The propeller of configuration A1 has a diameter $Db = 0.3048m$, and is located downstream of the wind tunnel nozzle exit at $1000mm$. Inflow velocity at the exit of the nozzle is $U_\infty = 30m/s$. The cases simulated consider 2 different RPMs and 2 different tip-gap distances in relation to the plate. The cases simulated are:

| **Rotor tip-gap with Plate (mm)** | **RPM (rev/min)** |
|---|---|
| 5 | 6500 |
| 5 | 8100 |
| 70 | 6500 |
| 70 | 8100 |

Table 2: Summary of rotor tip-gap locations and corresponding RPMs used in the study.

### 4.1.1 Computational Domains and Boundary Conditions

As a first step, 3D AD RANS simulations were conducted on the configurations investigated using the DLR's TAU solver, which requires as an input a table of the propeller blade geometrical parameters, together with lift and drag coefficients computed at different sections along the blade span. For the lift and drag values, 2D RANS simulations were conducted for given airfoil sections extracted from the blade geometry. The computational domain of the 3D AD RANS simulations considers part of the wind tunnel configuration, including the nozzle and the $10mm$ thick boundary layer trip at the exit of the nozzle. An hybrid computational mesh was generated of approximately 20 mln cells. A detail of the mesh generated can be seen in Fig. 24. The boundary conditions used in these setups, together with the particular TAU AD boundary condition, are:

- of viscous wall type for nozzle, wind tunnel walls, boundary layer trip and nacelle,
- of reservoir-pressure-inflow type for the wind tunnel nozzle inlet
- of exit-pressure-inflow type for the wind tunnel exit

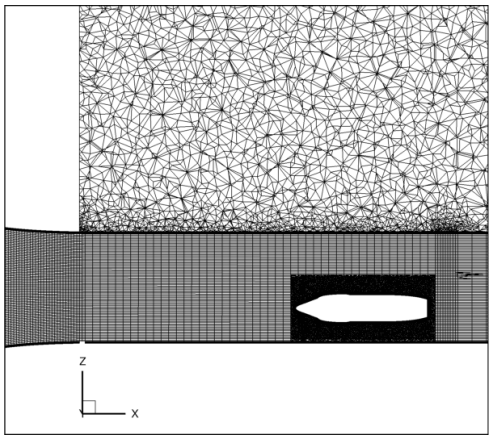



Figure 24: RANS grid example, Config. A1

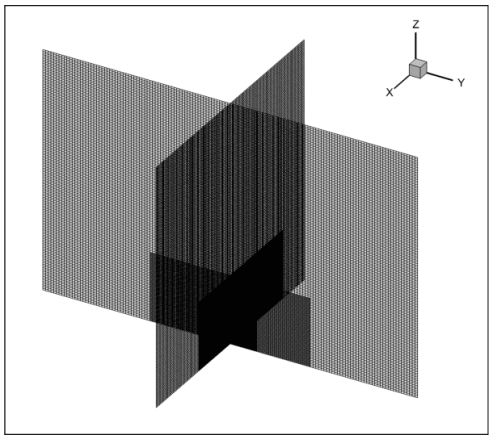



Figure 25: CAA grid example, Config. A1

The computational domain of the 3D CAA simulations consists of a hierarchical Cartesian grid with a refinement region around the propeller modelled. Three overall grid levels were considered, with smallest node spacing of $8mm$, for a total of approximately 6 mln points (Fig. 25). All boundaries of immersed solid wall bodies are assigned a no-slip wall boundary condition, whereas the remaining boundaries are assigned a Thompson type boundary condition ((Thompson, 1987) and (Thompson, 1990)). A total of 5 revolutions was simulated.

### 4.1.2 Simulations Results

Figure 26 and Fig. 27 show the comparison of the velocity profiles measured at a distance of $10cm$ from the exit of the wind tunnel nozzle, for both the experiments and the RANS simulations for the cases with $RPM = 6500$. A good agreement in general can be observed, with matching boundary profiles. In the upper part of the profile, a discrepancy between measurements and simulations can be identified, due probably to a more rapid dissipation of turbulence in the nozzle exit shear layer of the experiments.

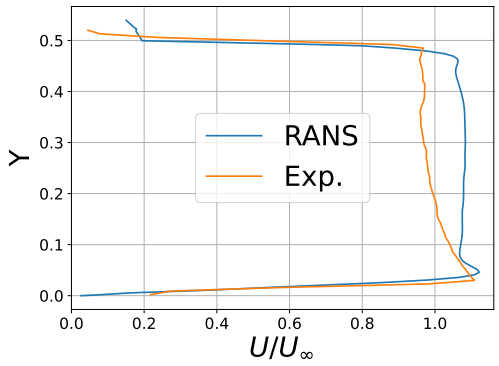



Figure 26: Velocity profile at 10 cm after nozzle exit, Config A1, RPM6500, Tip-Gap 5 mm

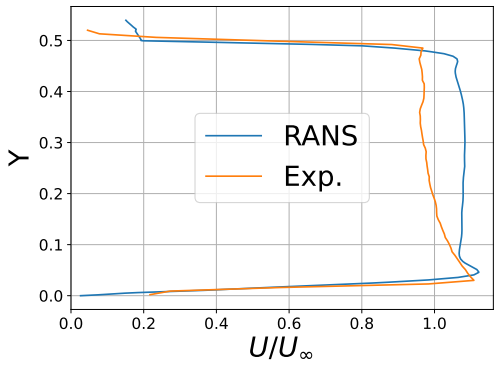



Figure 27: Velocity profile at 10 cm after nozzle exit, Config A1, RPM6500, Tip-Gap 70 mm

The CAA results obtained are shown first as contour plots, to highlight qualitatively the capabilities of the rotor tonal noise prediction model. In addition to this, results are shown as narrow band spectra to highlight the predicted tonal component, and as third octave band spectra, to allow the addition of the trailing edge noise and leading edge noise contribution to the tonal component. For the latter plots' type, third octave bands are chosen, since the Lowson model provides a prediction in terms of third octave bands data. The results are considered for a selected microphone at 90° for both overhead and side microphone arrays. Overall, a very good agreement can be observed between experiments and tonal component prediction, whereas the addition of trailing edge noise and leading edge noise components agrees well for certain cases (e.g Fig. 39 and Fig. 47), but other cases still show that the current implementation might need further tuning.

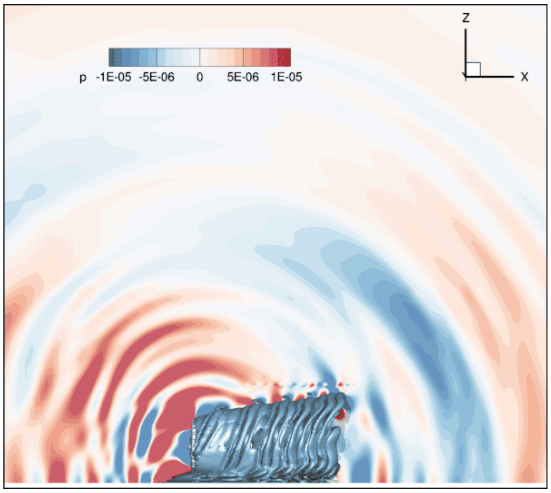



Figure 28: Contour plot of p', Config A1, RPM6500, Tip-Gap 5 mm

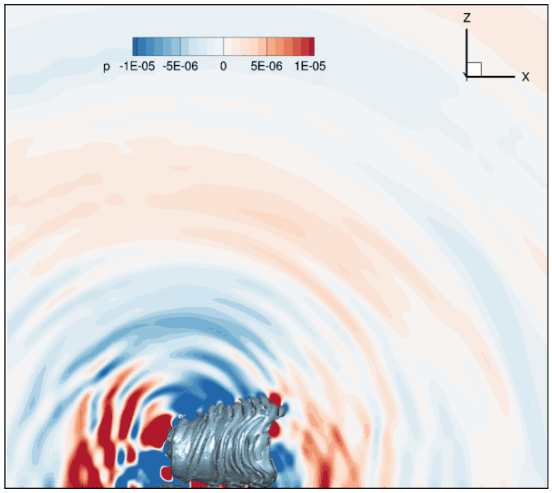



Figure 29: Contour plot of p', Config A1, RPM6500, Tip-Gap 70 mm

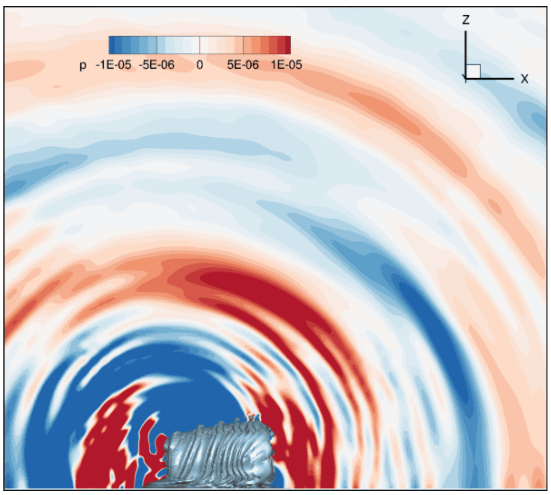



Figure 30: Contour plot of p', Config A1, RPM8100, Tip-Gap 5 mm

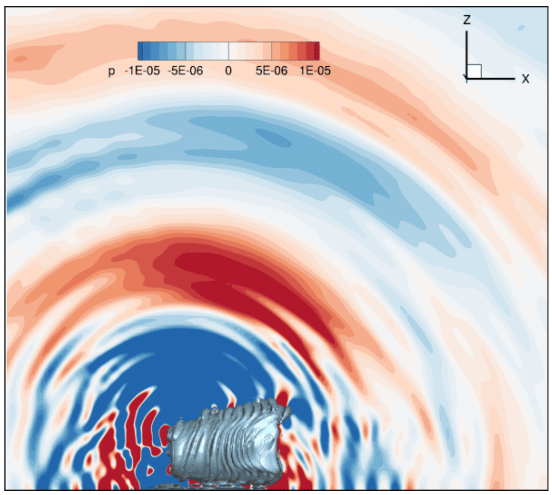



Figure 31: Contour plot of p', Config A1, RPM8100, Tip-Gap 70 mm

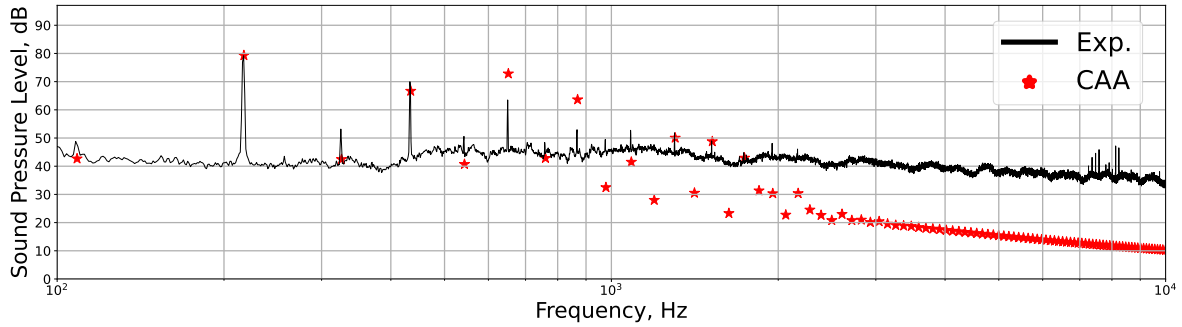



Figure 32: Comparison of CAA results with experiments, narrow band plot, Config A1, RPM6500, Tip-Gap 5 mm, Mic 90°, Overhead mics array, tonal component

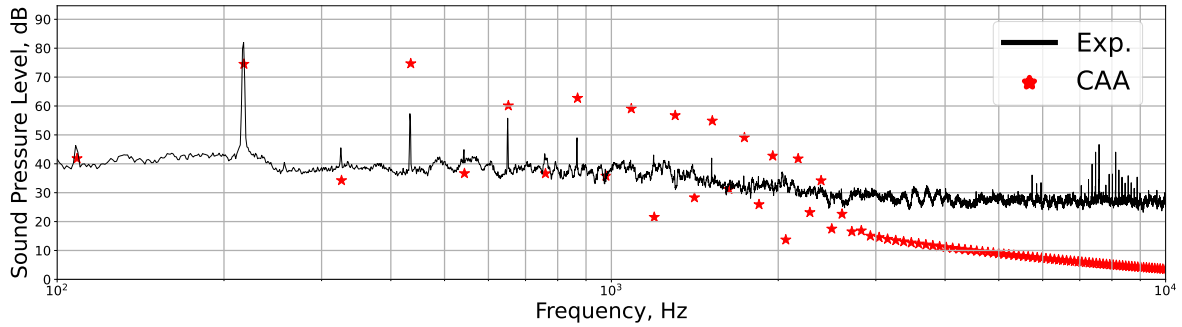



Figure 33: Comparison of CAA results with experiments, narrow band plot, Config A1, RPM6500, Tip-Gap 5 mm, Mic 90°, Side mics array, tonal component

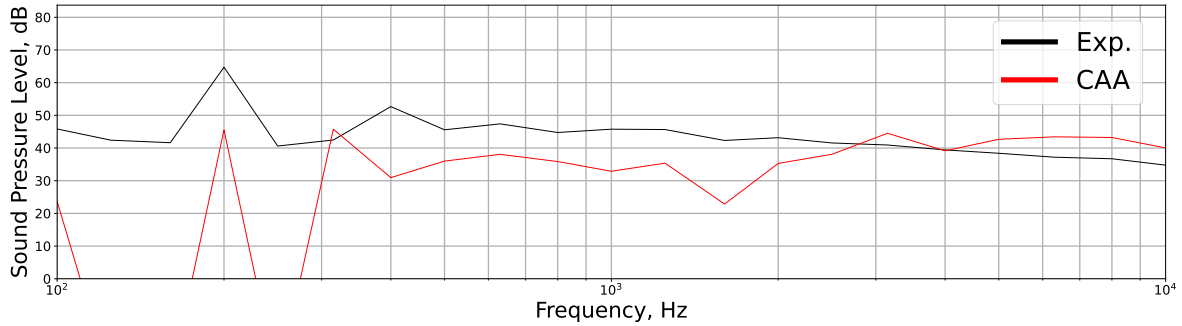



Figure 34: Comparison of CAA results with experiments, third octave band plot, Config A1, RPM6500, Tip-Gap 5 mm, Mic 90°, Overhead mics array, tonal + broadband components

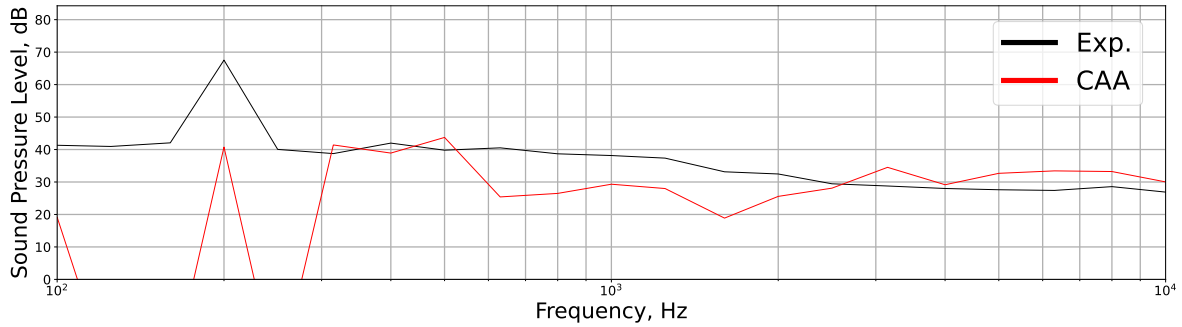



Figure 35: Comparison of CAA results with experiments, third octave band plot, Config A1, RPM6500, Tip-Gap 5 mm, Mic 90°, Side mics array, tonal + broadband components

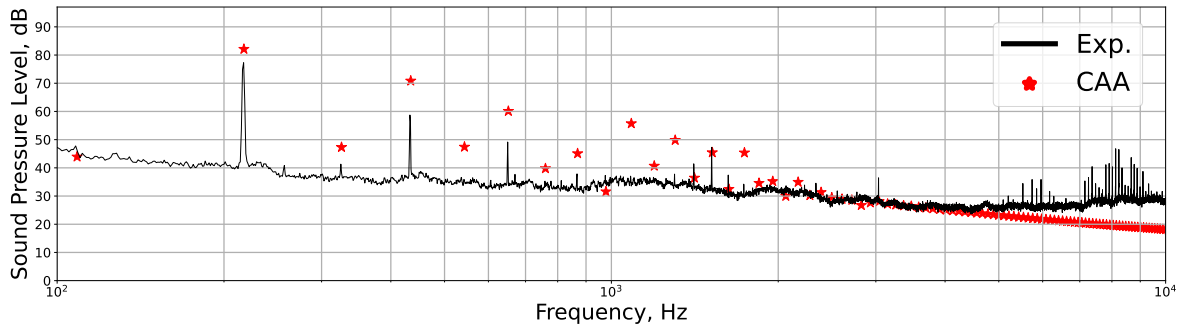



Figure 36: Comparison of CAA results with experiments, narrow band plot, Config A1, RPM6500, Tip-Gap 70 mm, Mic 90°, Overhead mics array, tonal component

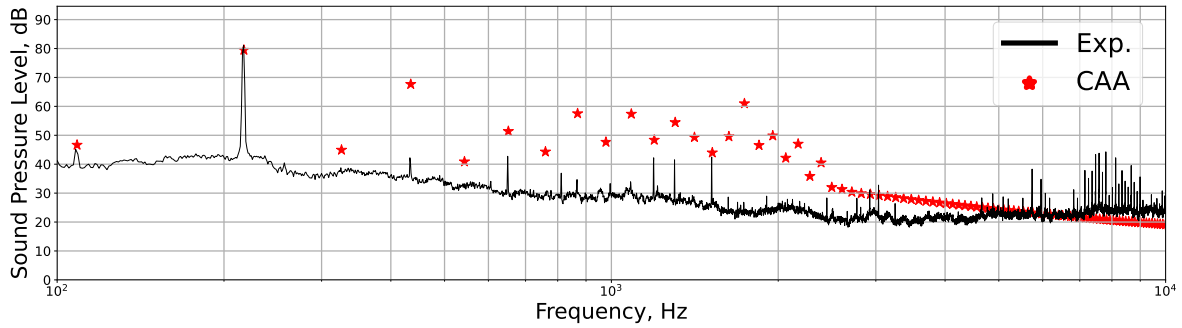



Figure 37: Comparison of CAA results with experiments, narrow band plot, Config A1, RPM6500, Tip-Gap 70 mm, Mic 90°, Side mics array, tonal component

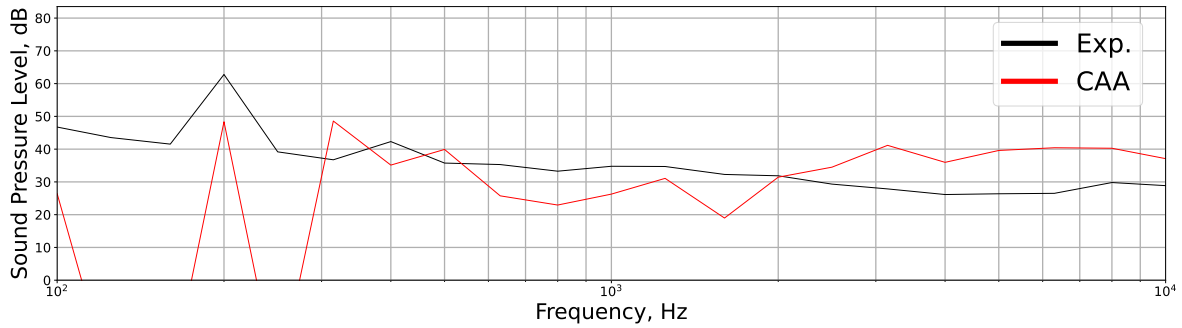



Figure 38: Comparison of CAA results with experiments, third octave band plot, Config A1, RPM6500, Tip-Gap 70 mm, Mic 90°, Overhead mics array, tonal + broadband components

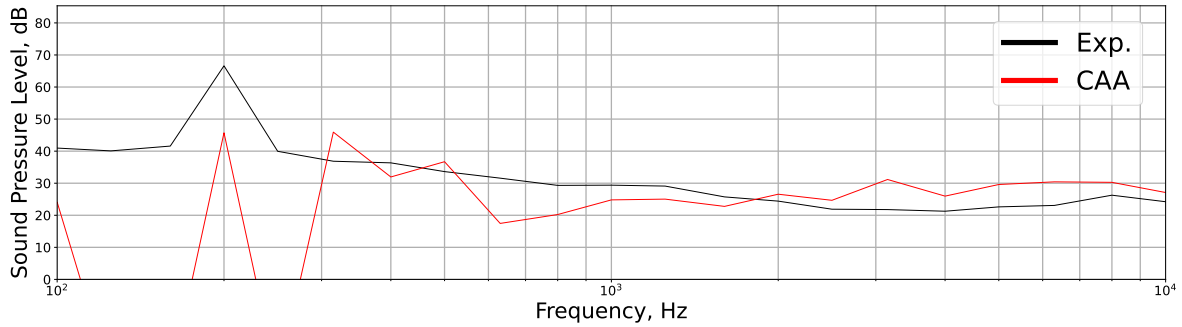



Figure 39: Comparison of CAA results with experiments, third octave band plot, Config A1, RPM6500, Tip-Gap 70 mm, Mic 90°, Side mics array, tonal + broadband components

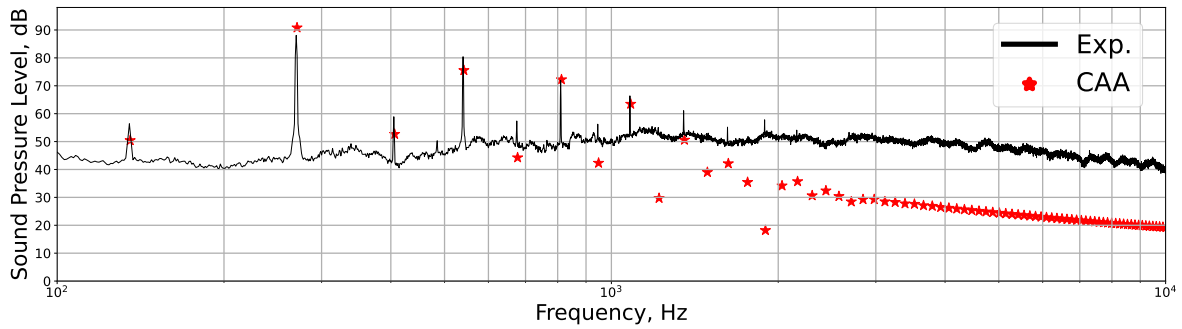



Figure 40: Comparison of CAA results with experiments, narrow band plot, Config A1, RPM8100, Tip-Gap 5 mm, Mic 90°, Overhead mics array, tonal component

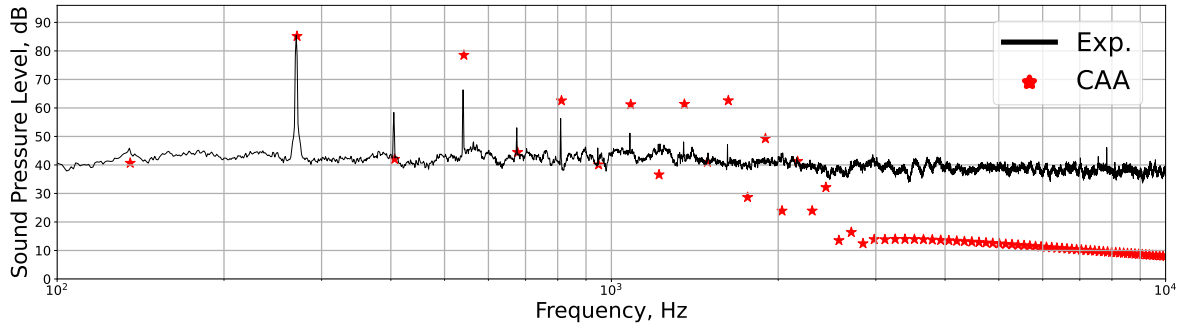



Figure 41: Comparison of CAA results with experiments, narrow band plot, Config A1, RPM8100, Tip-Gap 5 mm, Mic 90°, Side mics array, tonal component

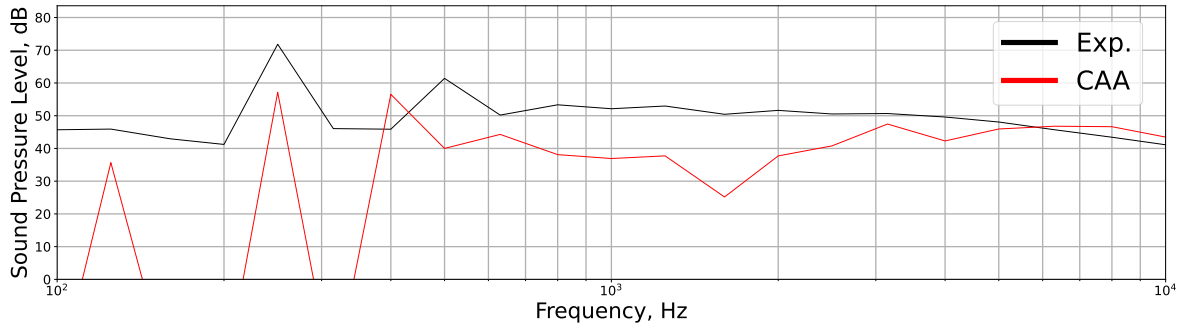



Figure 42: Comparison of CAA results with experiments, third octave band plot, Config A1, RPM8100, Tip-Gap 5 mm, Mic 90°, Overhead mics array, tonal + broadband components

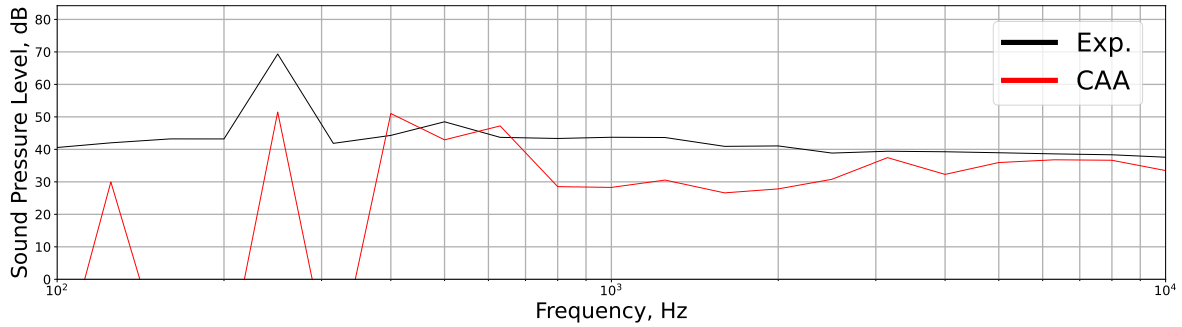



Figure 43: Comparison of CAA results with experiments, third octave band plot, Config A1, RPM8100, Tip-Gap 5 mm, Mic 90°, Side mics array, tonal + broadband components

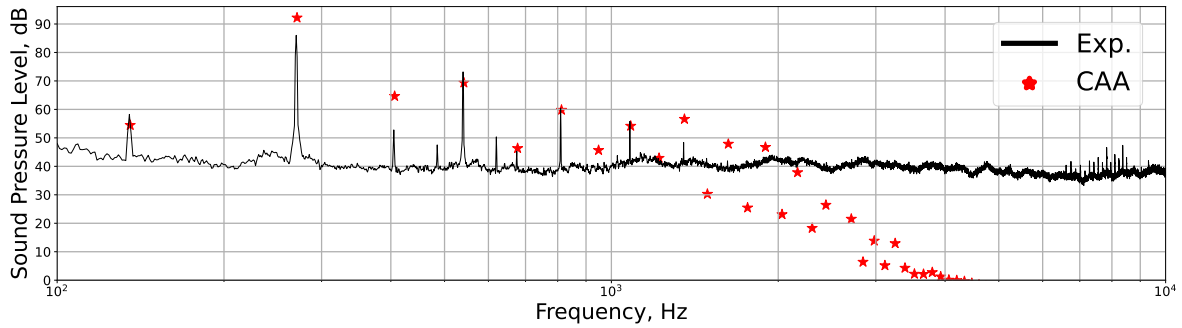



Figure 44: Comparison of CAA results with experiments, narrow band plot, Config A1, RPM8100, Tip-Gap 70 mm, Mic 90°, Overhead mics array, tonal component

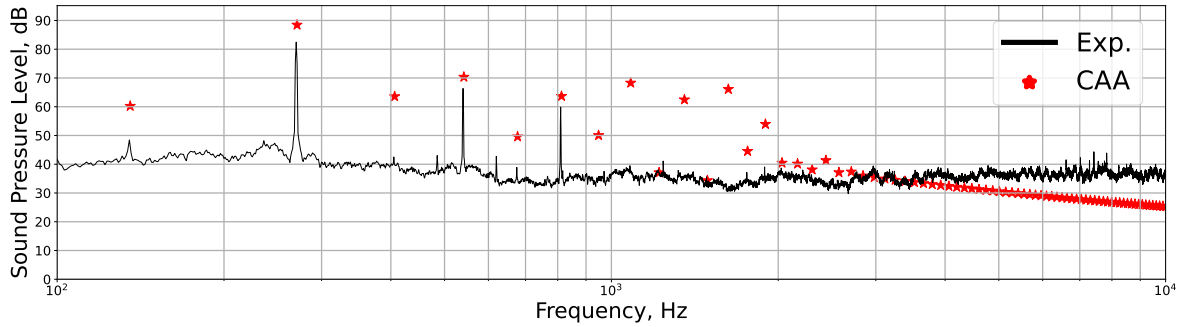



Figure 45: Comparison of CAA results with experiments, narrow band plot, Config A1, RPM8100, Tip-Gap 70 mm, Mic 90°, Side mics array, tonal component

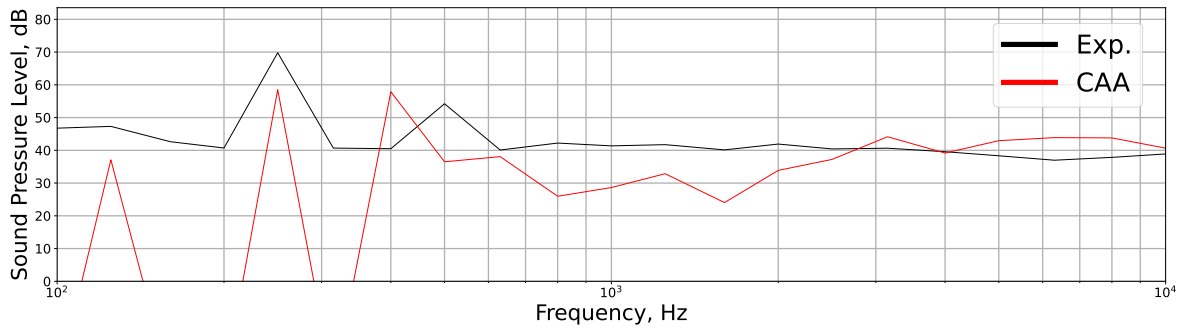



Figure 46: Comparison of CAA results with experiments, third octave band plot, Config A1, RPM8100, Tip-Gap 70 mm, Mic 90°, Overhead mics array, tonal + broadband components

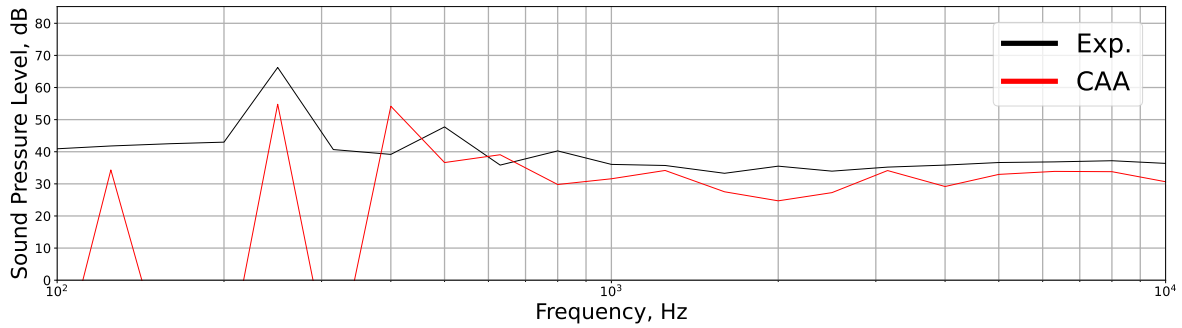



Figure 47: Comparison of CAA results with experiments, third octave band plot, Config A1, RPM8100, Tip-Gap 70 mm, Mic 90°, Side mics array, tonal + broadband components

### 4.1.3 Computational Cost of the Model

The computational cost of each simulation step is:

- 2D RANS for AD table creation: $128 Cores \cdot 15 BladeSections \cdot 3 Hours = 5760 CoreHours$
- 3D AD RANS to generate background meanflow and AD solution for CAA: $1280 Cores \cdot 8 Hours = 10240 CoreHours$
- 3D CAA tonal noise prediction: $512 Cores \cdot 1 Hour = 512 CoreHours$
- 2D CFD-CAA trailing edge broadband noise prediction: $128 Cores \cdot 15 BladeSections \cdot 18 Hours = 34560 CoreHours$
- Analytical Lowson model for leading edge broadband noise prediction: $1 Cores \cdot 15 BladeSections \cdot 40 seconds = 0.166 CoreHours$
- Total Core Hours = $52608.166 CoreHours$

## 4.2 Configuration A2

The propeller of configuration A2 has a diameter $Db = 0.3048m$, and is located downstream of the wind tunnel nozzle exit at $800mm$. Inflow velocity at the exit of the nozzle is $U_\infty = 27m/s$. The cases simulated consider 2 different RPMs and 2 different tip-gap distances in relation to the plate. The cases simulated are:

| **Rotor tip-gap with Plate (mm)** | **RPM (rev/min)** |
|---|---|
| 5 | 6500 |
| 5 | 8100 |
| 70 | 6500 |
| 70 | 8100 |

Table 3: Summary of rotor tip-gap locations and corresponding RPMs used in the study.

### 4.2.1 Computational Domains and Boundary Conditions

As a first step, 3D AD RANS simulations were conducted on the configurations investigated using the DLR's TAU solver, which requires as an input a table of the propeller blade geometrical parameters, together with lift and drag coefficients, computed at different sections along the blade span. For the lift and drag values, 2D RANS simulations were conducted for given airfoil sections extracted from the blade geometry. The computational domain for the 3D AD RANS simulations considers part of the wind tunnel configuration, including the nozzle and the $10mm$ thick boundary layer trip at the exit of the nozzle. An hybrid computational mesh was generated of approximately 20 mln cells. A detail of the mesh generated can be seen in Fig. 48. The boundary conditions used in these setups, together with the particular TAU AD boundary condition, are:

- of viscous wall type for nozzle, wind tunnel walls, boundary layer trip and nacelle,
- of reservoir-pressure-inflow type for the wind tunnel nozzle inlet
- of exit-pressure-inflow type for the wind tunnel exit

The computational domain of the 3D CAA simulations consists of a hierarchical Cartesian grid with a refinement region around the propeller modelled. Three overall grid levels were considered, with smallest node spacing of $8mm$, for a total of approximately 6 mln points (Fig. 49). All boundaries of immersed solid wall bodies are assigned a no-slip wall boundary condition, whereas the remaining boundaries are assigned a Thompson type boundary condition. A total of 5 revolutions was simulated.

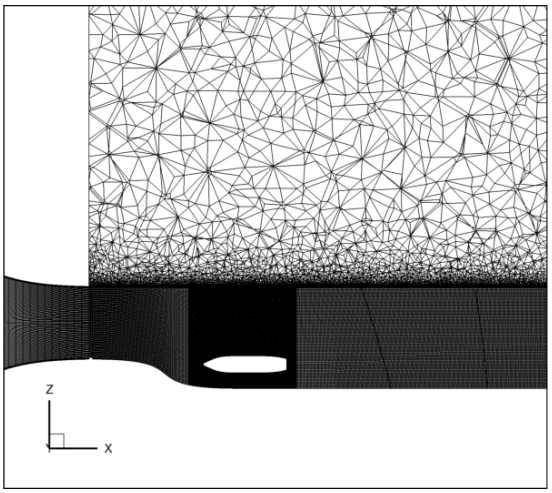



Figure 48: RANS grid example, config. A1

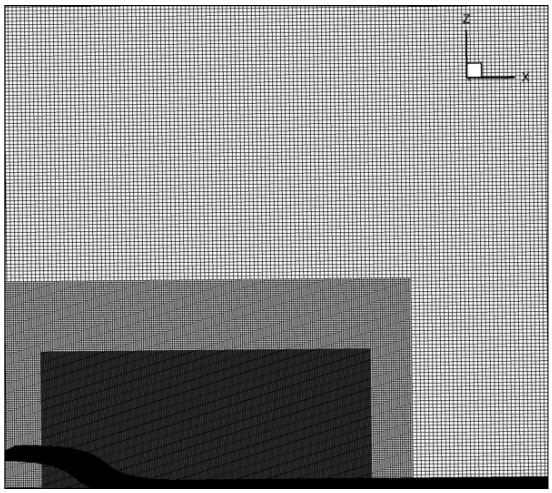



Figure 49: CAA grid example, config. A1

### 4.2.2 Simulations Results

Figure 50 and Fig. 51 show the comparison of the velocity profiles measured at a distance of $10cm$ from the exit of the wind tunnel nozzle, for both the experiments and the RANS simulations for the cases with $RPM = 6500$. A close agreement in general can be observed for the velocity profiles, even though in the boundary layer region, a discrepancy is seen for the experimental data when compared to the RANS data, which could be probably due to a stronger vortical structure being convected after the trip in the experiments.

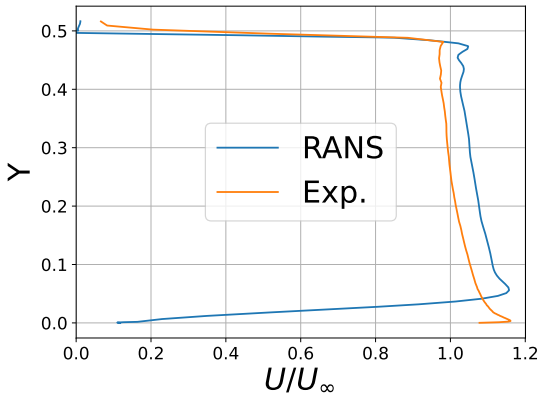



Figure 50: Velocity profile at 10 cm after nozzle exit, Config. A2, RPM6500, Tip-Gap 5 mm

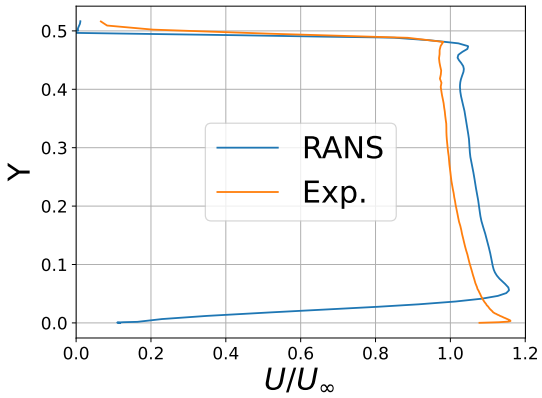



Figure 51: Velocity profile at 10 cm after nozzle exit, Config. A2, RPM6500, Tip-Gap 70 mm

The CAA results obtained are shown first as contour plots, to highlight qualitatively the capabilities of the rotor tonal noise prediction model. In addition to this, results are shown as narrow band spectra to highlight the predicted tonal component, and as third octave band spectra, to allow the addition of the trailing edge noise and leading edge noise contribution to the tonal component.

For the latter plots' type, third octave bands are chosen since the Lowson model provides a prediction in terms of third octave bands data. The results are considered for a selected microphone at 90° for both overhead and side microphone arrays. Overall, a very good agreement can be observed between experiments and tonal component prediction, whereas the addition of trailing edge noise and leading edge noise components agrees well for certain cases (e.g Fig. 63 and Fig. 70), but other cases still show that the current implementation might need further tuning.

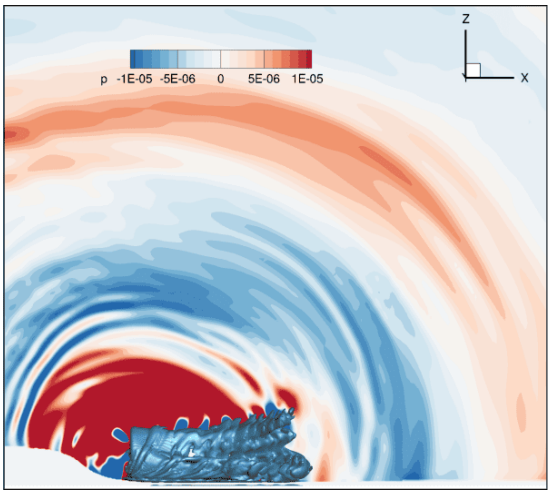



Figure 52: Contour plot of p', Config A2, RPM6500, Tip-Gap 5 mm

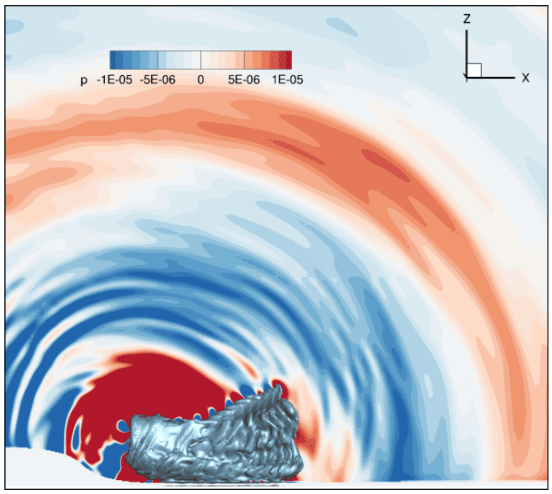



Figure 53: Contour plot of p', Config A2, RPM6500, Tip-Gap 70 mm

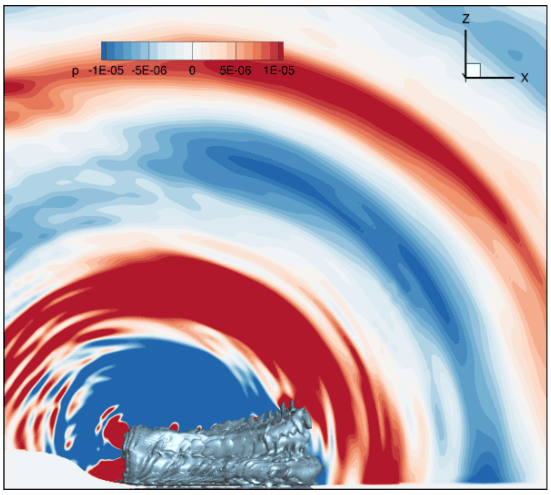



Figure 54: Contour plot of p', Config A2, RPM8100, Tip-Gap 5 mm

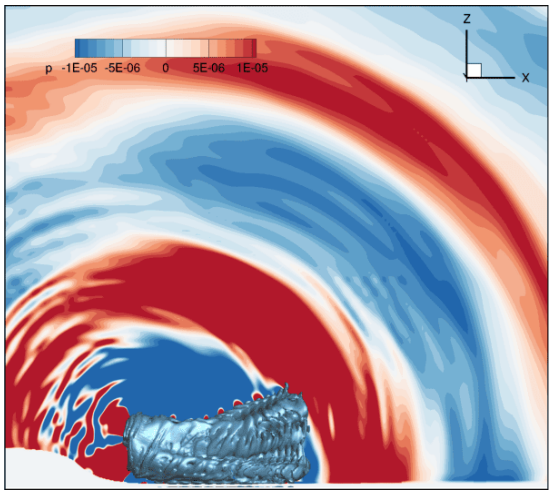



Figure 55: Contour plot of p', Config A2, RPM8100, Tip-Gap 70 mm

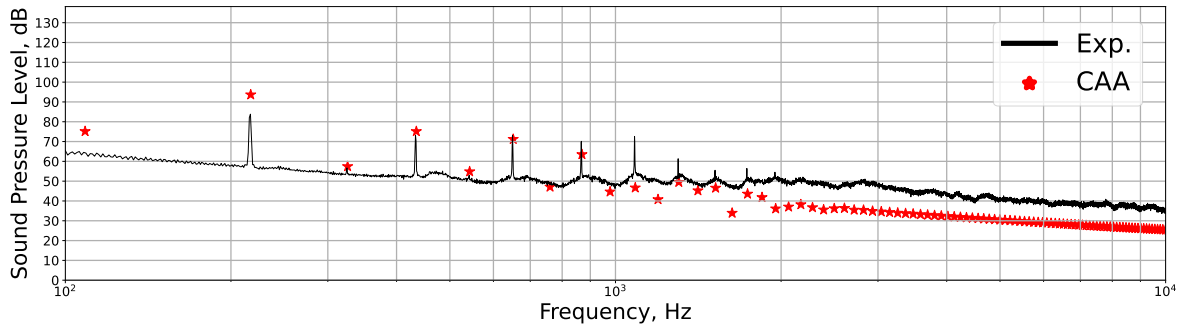



Figure 56: Comparison of CAA results with experiments, narrow band plot, Config A2, RPM6500, Tip-Gap 5 mm, Mic 90°, Overhead mics array, tonal component

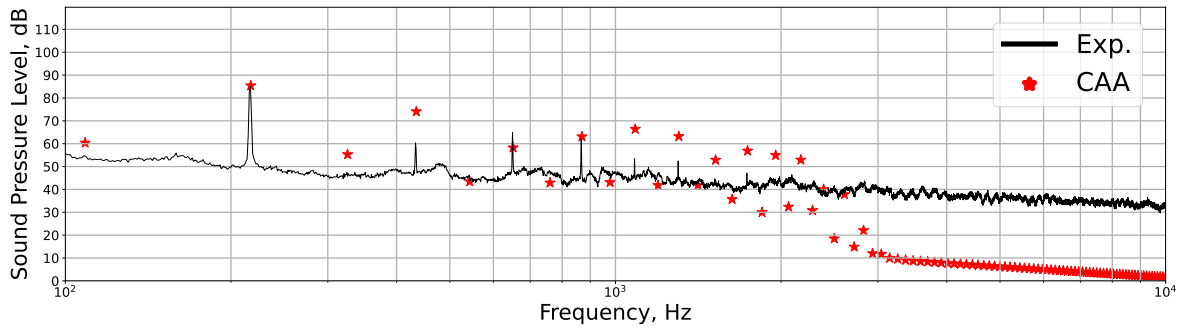



Figure 57: Comparison of CAA results with experiments, narrow band plot, Config A2, RPM6500, Tip-Gap 5 mm, Mic 90°, Side mics array, tonal component

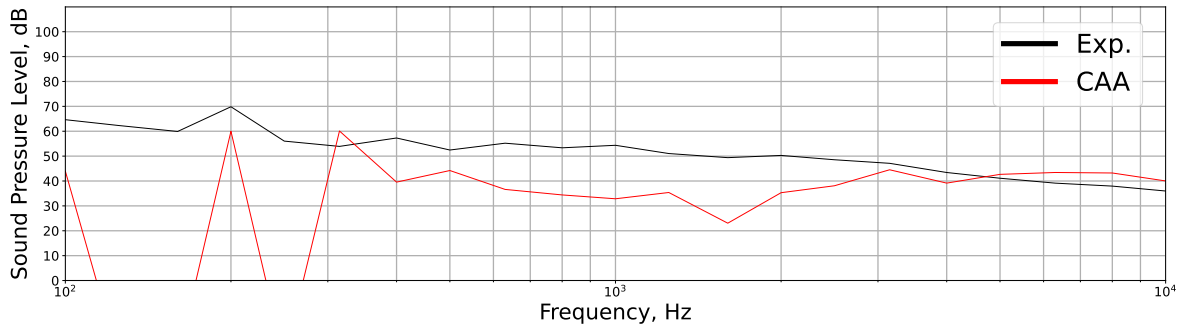



Figure 58: Comparison of CAA results with experiments, third octave band plot, Config A2, RPM6500, Tip-Gap 5 mm, Mic 90°, Overhead mics array, tonal + broadband components

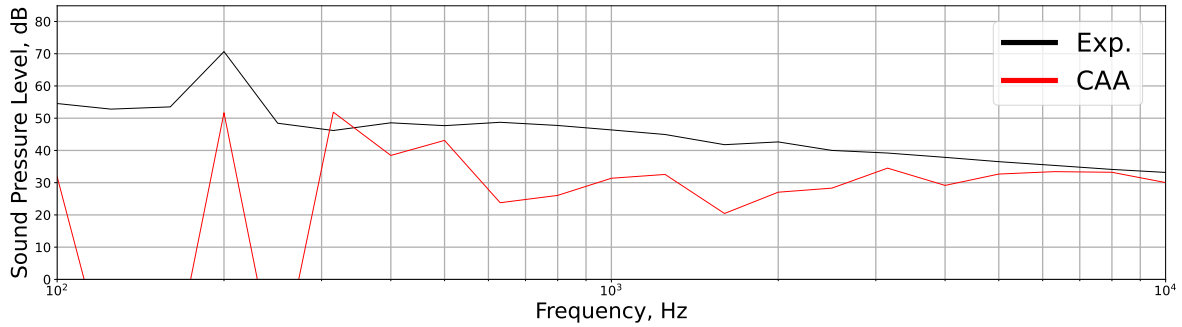



Figure 59: Comparison of CAA results with experiments, third octave band plot, Config A2, RPM6500, Tip-Gap 5 mm, Mic 90°, Side mics array, tonal + broadband components

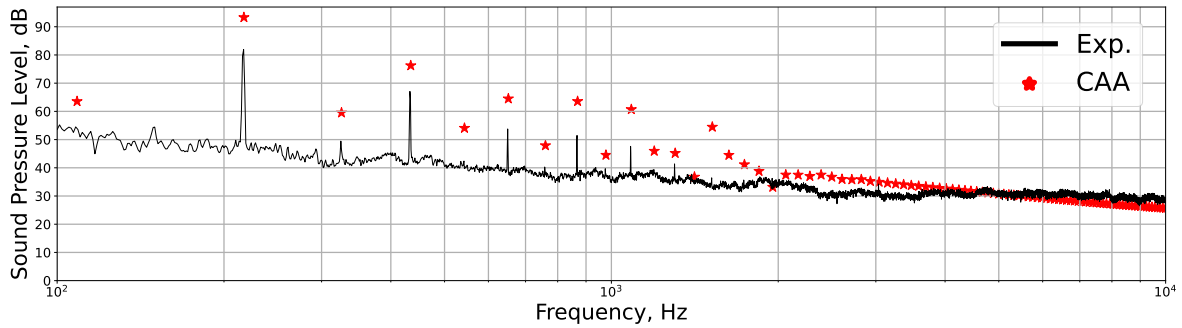



Figure 60: Comparison of CAA results with experiments, narrow band plot, Config A2, RPM6500, Tip-Gap 70 mm, Mic 90°, Overhead mics array, tonal component

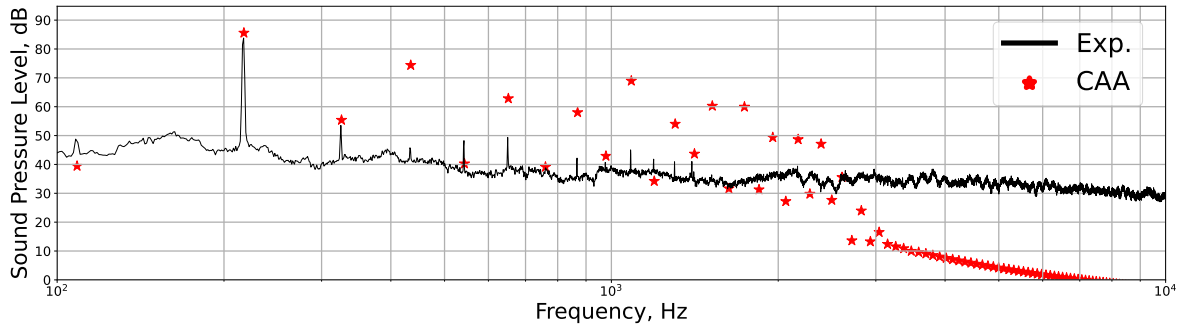



Figure 61: Comparison of CAA results with experiments, narrow band plot, Config A2, RPM6500, Tip-Gap 70 mm, Mic 90°, Side mics array, tonal component

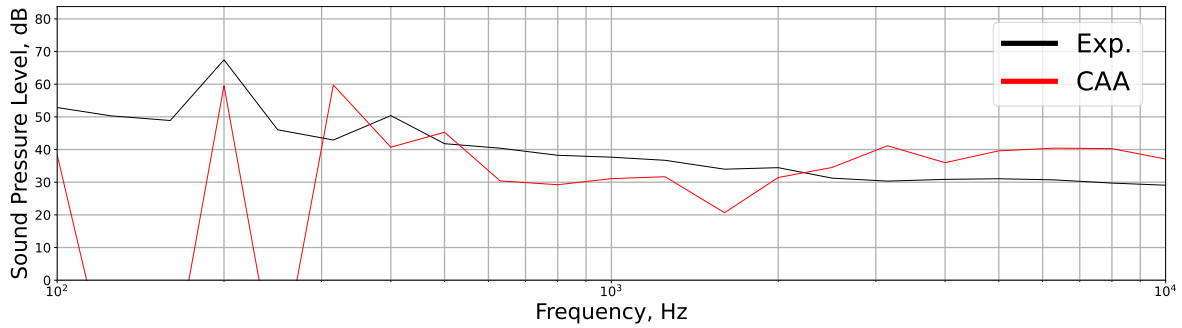



Figure 62: Comparison of CAA results with experiments, third octave band plot, Config A2, RPM6500, Tip-Gap 70 mm, Mic 90°, Overhead mics array, tonal + broadband components

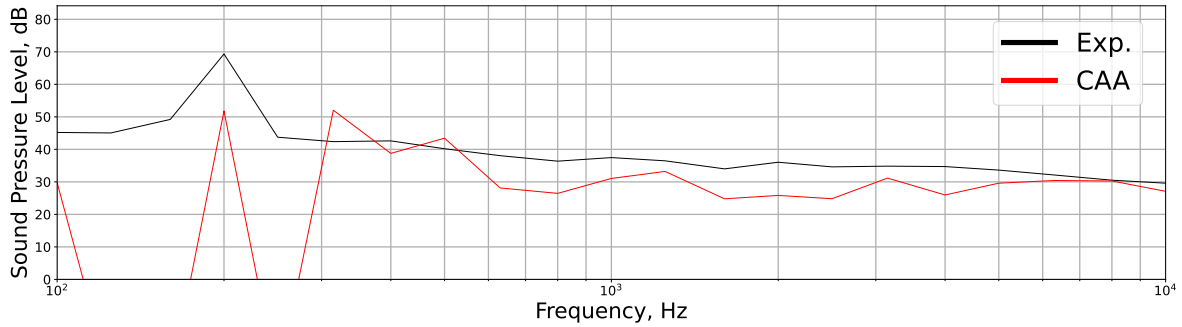



Figure 63: Comparison of CAA results with experiments, third octave band plot, Config A2, RPM6500, Tip-Gap 70 mm, Mic 90°, Side mics array, tonal + broadband components

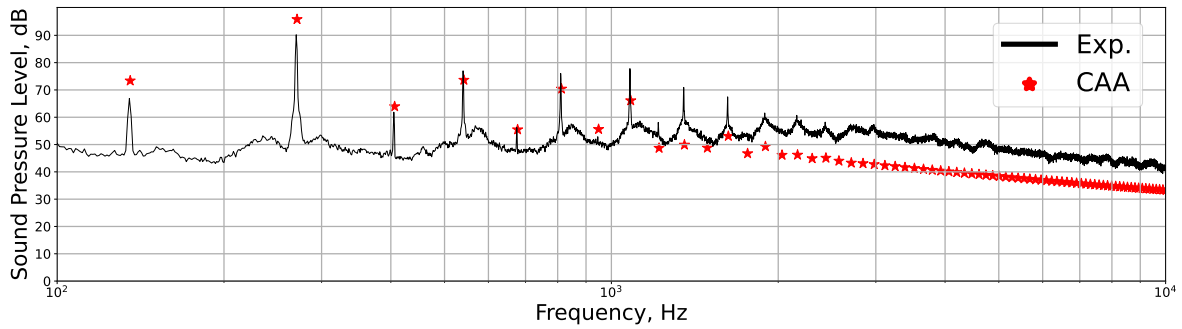



Figure 64: Comparison of CAA results with experiments, narrow band plot, Config A2, RPM8100, Tip-Gap 5 mm, Mic 90°, Overhead mics array, tonal component

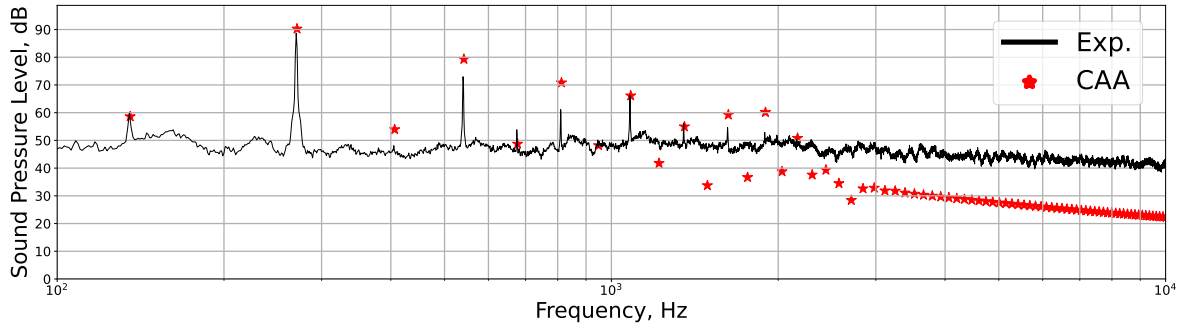



Figure 65: Comparison of CAA results with experiments, narrow band plot, Config A2, RPM8100, Tip-Gap 5 mm, Mic 90°, Side mics array, tonal component

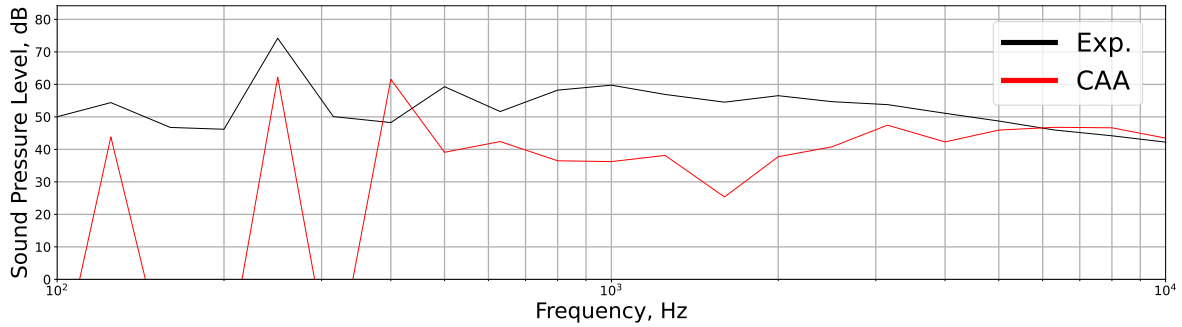



Figure 66: Comparison of CAA results with experiments, third octave band plot, Config A2, RPM8100, Tip-Gap 5 mm, Mic 90°, Overhead mics array, tonal + broadband components

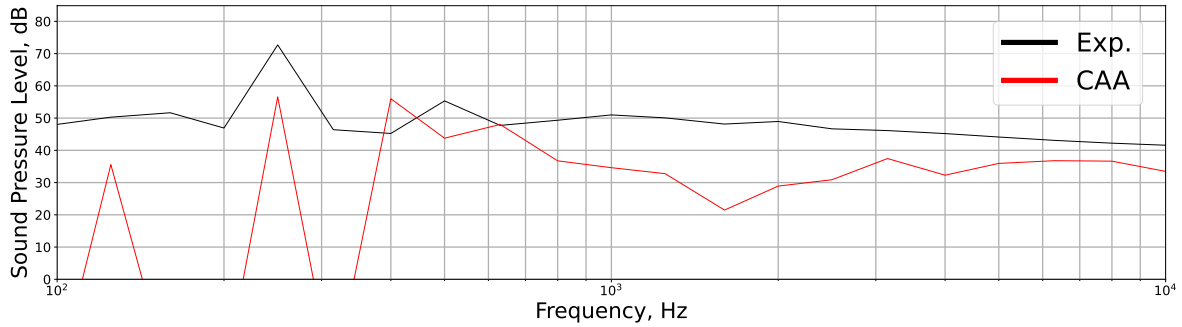



Figure 67: Comparison of CAA results with experiments, third octave band plot, Config A2, RPM8100, Tip-Gap 5 mm, Mic 90°, Side mics array, tonal + broadband components

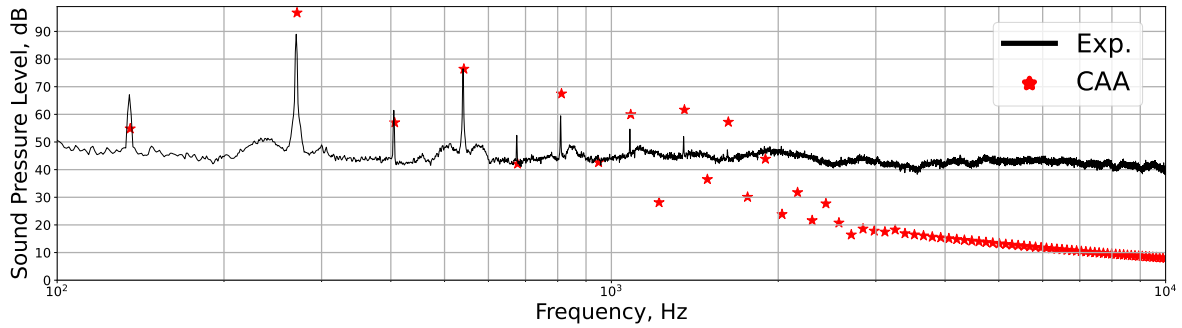



Figure 68: Comparison of CAA results with experiments, narrow band plot, Config A2, RPM8100, Tip-Gap 70 mm, Mic 90°, Overhead mics array, tonal component

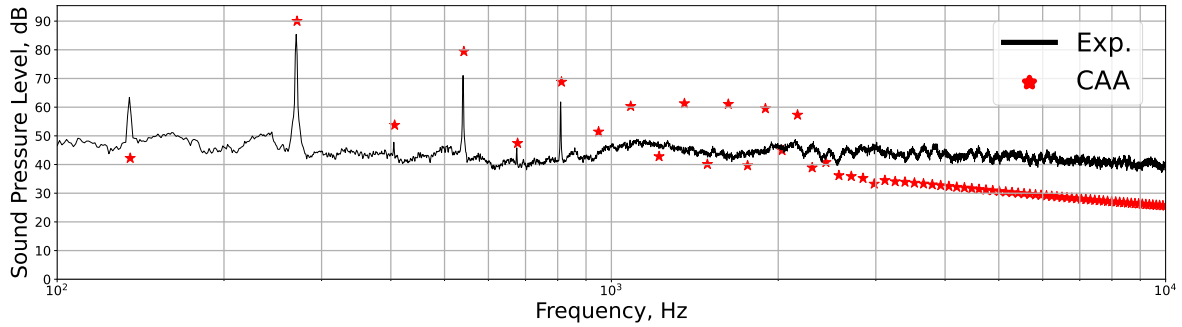



Figure 69: Comparison of CAA results with experiments, narrow band plot, Config A2, RPM8100, Tip-Gap 70 mm, Mic 90°, Side mics array, tonal component

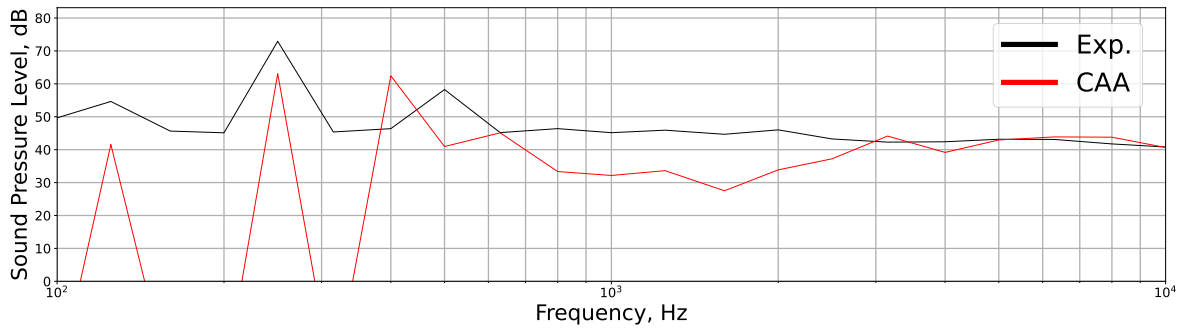



Figure 70: Comparison of CAA results with experiments, third octave band plot, Config A2, RPM8100, Tip-Gap 70 mm, Mic 90°, Overhead mics array, tonal + broadband components

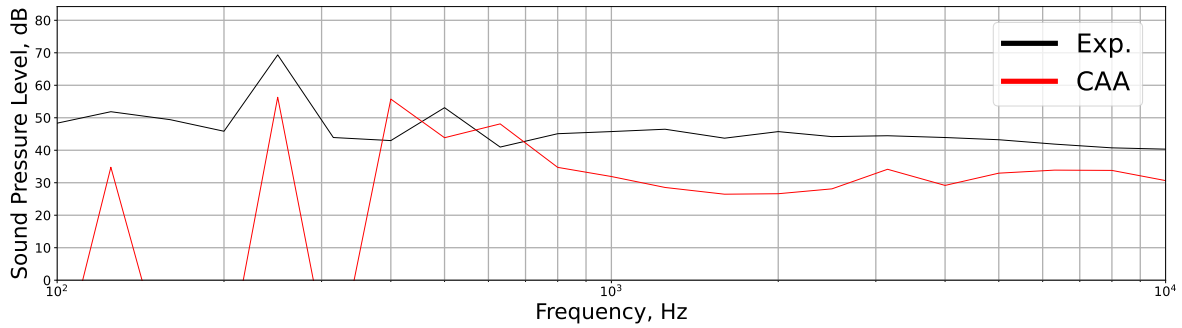



Figure 71: Comparison of CAA results with experiments, third octave band plot, Config A2, RPM8100, Tip-Gap 70 mm, Mic 90°, Side mics array, tonal + broadband components

### 4.2.3 Computational Cost of the Model

The computational cost of each simulation step is:

- 2D RANS for AD table creation: $128 Cores \cdot 15 BladeSections \cdot 3 Hours = 5760 CoreHours$
- 3D AD RANS to generate background meanflow and AD solution for CAA: $1280 Cores \cdot 8 Hours = 10240 CoreHours$
- 3D CAA tonal noise prediction: $512 Cores \cdot 1 Hour = 512 CoreHours$
- 2D CFD-CAA trailing edge broadband noise prediction: $128 Cores \cdot 15 BladeSections \cdot 18 Hours = 34560 CoreHours$
- Analytical Lowson model for leading edge broadband noise prediction: $1 Cores \cdot 15 BladeSections \cdot 40 seconds = 0.166 CoreHours$
- Total Core Hours = $52608.166 CoreHours$

## 4.3 Configuration B1

The propeller of Config. B1 has a diameter $D = 0.2032m$. Inflow velocity for Config. B1 is $U_\infty = 30m/s$. The cases simulated consider a single propeller operating at $RPM = 11070$, and two additional three-propellers configurations, in which the rotor blades phase angle was varied between 0° and 30°.

### 4.3.1 Computational Domains and Boundary Conditions

As a first step, 3D AD RANS simulations were conducted on the configurations investigated using the DLR's TAU solver, which requires as an input a table of the propeller blade geometrical parameters, together with lift and drag coefficients, computed at different sections along the blade span. For the lift and drag values, 2D RANS simulations were conducted for given airfoil sections extracted from the blade geometry. The computational domain for the 3D AD RANS simulations is defined for an external flow setup, where the section of interest of the wing span is simulated. An hybrid computational mesh was generated of approximately 20 mln cells. A detail of the mesh generated can be seen in Fig. 72. The boundary conditions used in these setups, together with the particular TAU AD boundary condition, are:

- of viscous wall type for nacelles,
- of symmetry type for the spanwise boundaries
- of farfield type for the remaining boundaries

The computational domain of the 3D CAA simulations consists of a hierarchical Cartesian grid with a refinement region around the propeller modelled (Fig. 73). Three overall grid levels were considered, with smallest node spacing of $4mm$, for a total of approximately 20 mln points. All boundaries of immersed solid wall bodies are assigned a no-slip wall boundary condition, whereas the remaining boundaries are assigned a Thompson type boundary condition. A total of 5 revolutions was simulated.

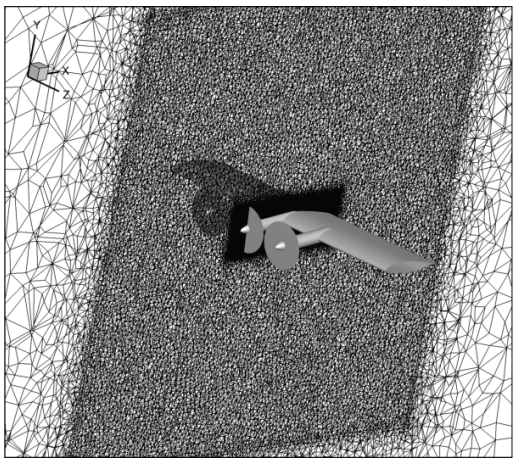


Figure 72: RANS grid example, Config. B1

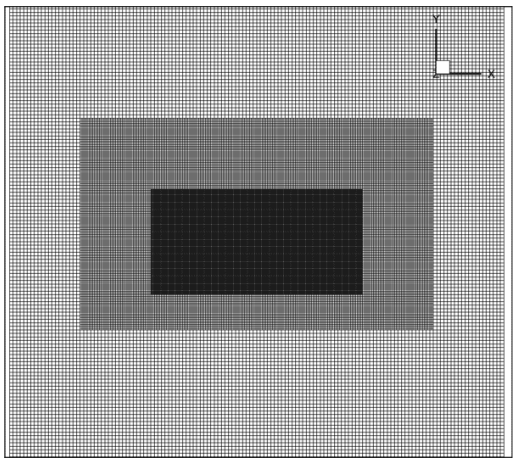


Figure 73: CAA grid example, Config. B1

### 4.3.2 Simulations Results

Figure 74 and Fig. 75 show the RANS solutions in terms of contour plots of the velocity magnitude, highlighting the modelled slipstream of the AD TAU model for the cases considered.

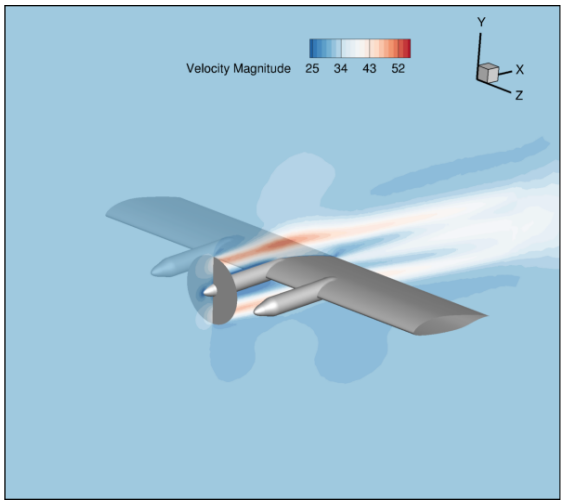



Figure 74: Contour plot of the velocity magnitude, Config. B1, single propeller

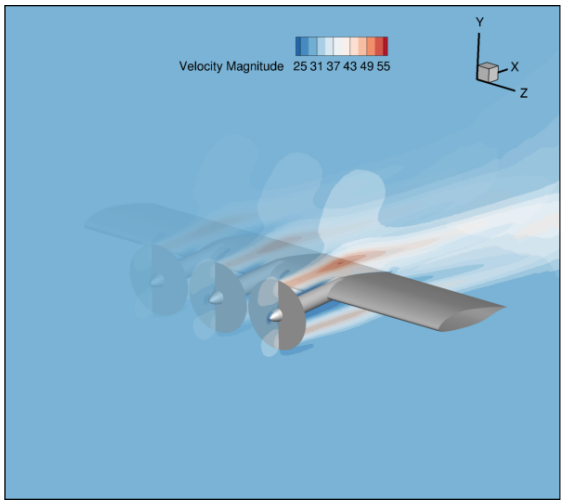



Figure 75: Contour plot of the velocity magnitude, Config. B1, three propellers

The CAA results obtained are shown first as contour plots, to highlight qualitatively the capabilities of the rotor tonal noise prediction model. In addition to this, results are shown as narrow band spectra to highlight the predicted tonal component, and as third octave band spectra, to allow the addition of the trailing edge noise and leading edge noise contribution to the tonal component. For the latter plots' type, third octave bands are chosen since the Lowson model provides a prediction in terms of third octave bands data. The results are considered for a selected microphone at 90° for the pressure side mics, and 270° for suction side mics. Overall, a good agreement can be observed between experiments and tonal component prediction, whereas the addition of trailing edge noise and leading edge noise components show that the current implementation might need further tuning.

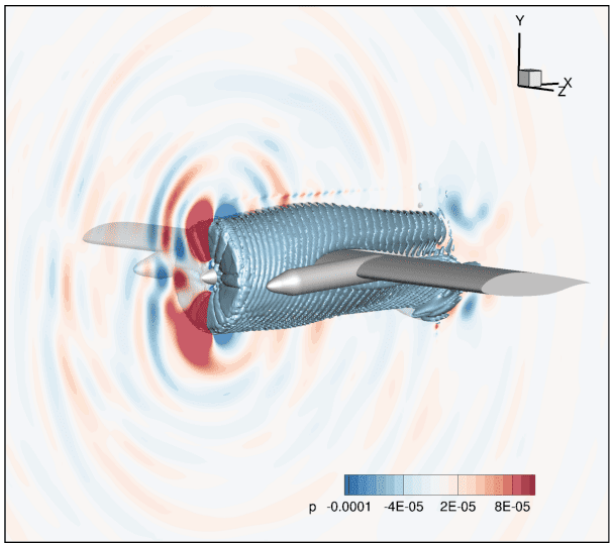



Figure 76: Contour plot of p', single propeller

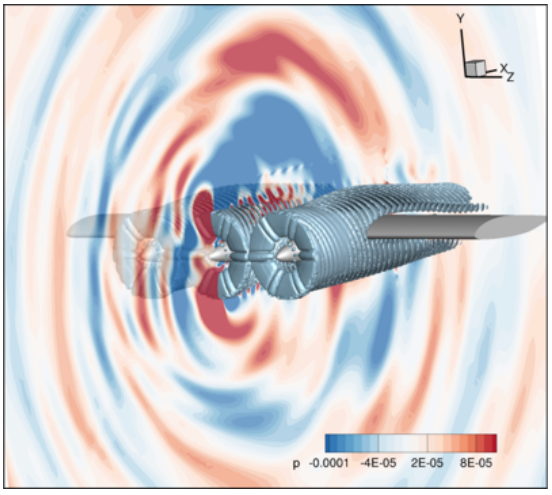



Figure 77: Contour plot of p', three propellers rotating in phase

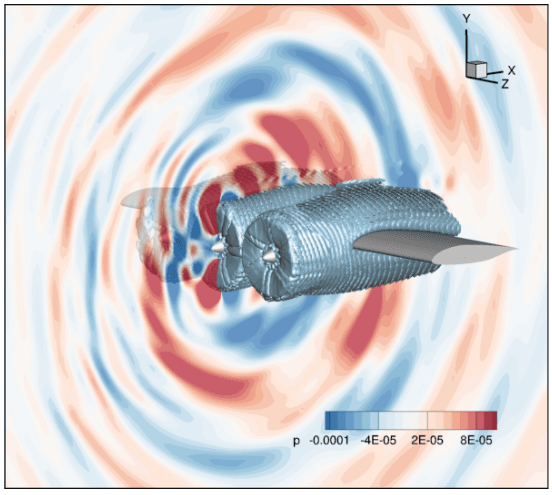



Figure 78: Contour plot of p', three propellers rotating with phase difference of 30°

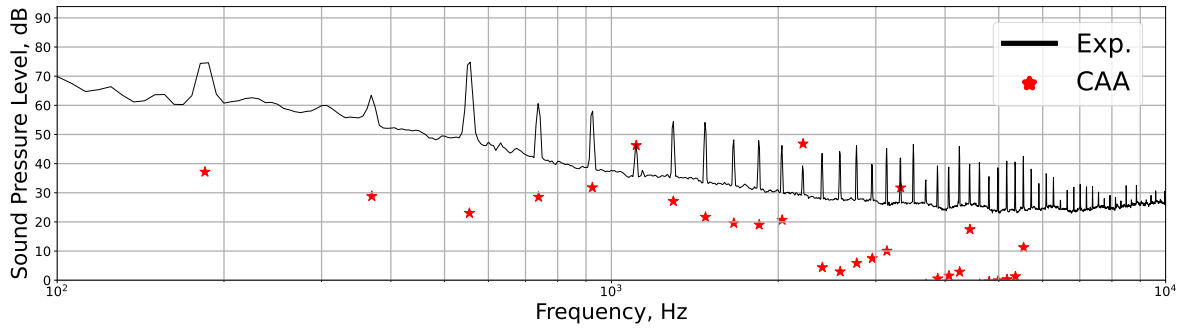



Figure 79: Comparison of CAA results with experiments, narrow band plot, Single Propeller, Mic 90°, Pressure Side mics, tonal component

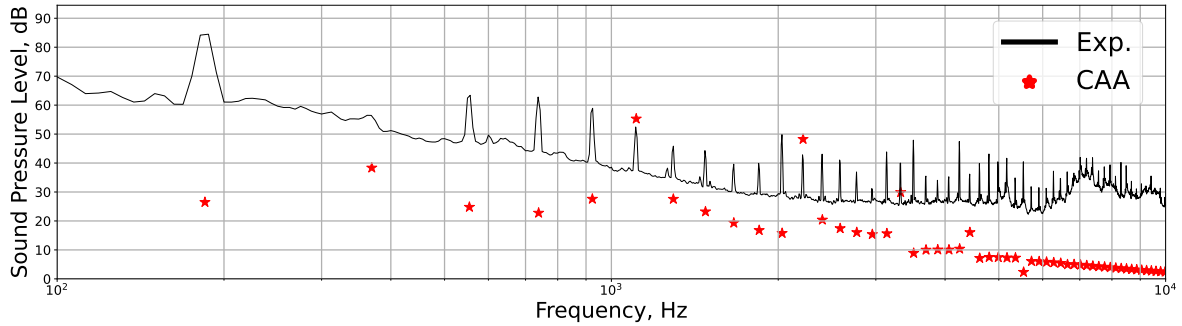



Figure 80: Comparison of CAA results with experiments, narrow band plot, Single Propeller, Mic 90°, Suction Side mics, tonal component

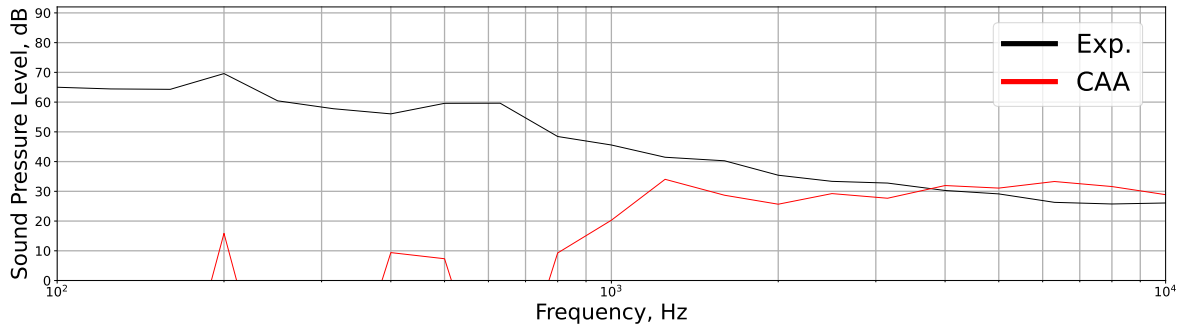



Figure 81: Comparison of CAA results with experiments, third octave band plot, Single Propeller, Mic 90°, Pressure Side mics, tonal + broadband components

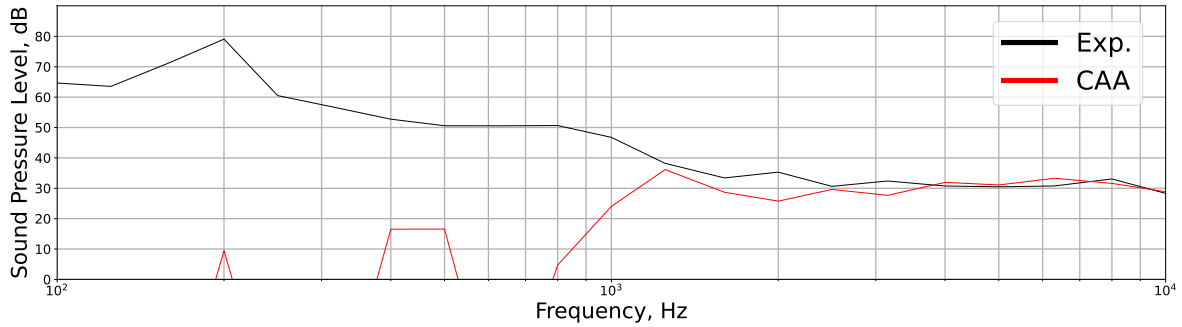



Figure 82: Comparison of CAA results with experiments, third octave band plot, Single Propeller, Mic 90°, Suction Side mics, tonal + broadband components

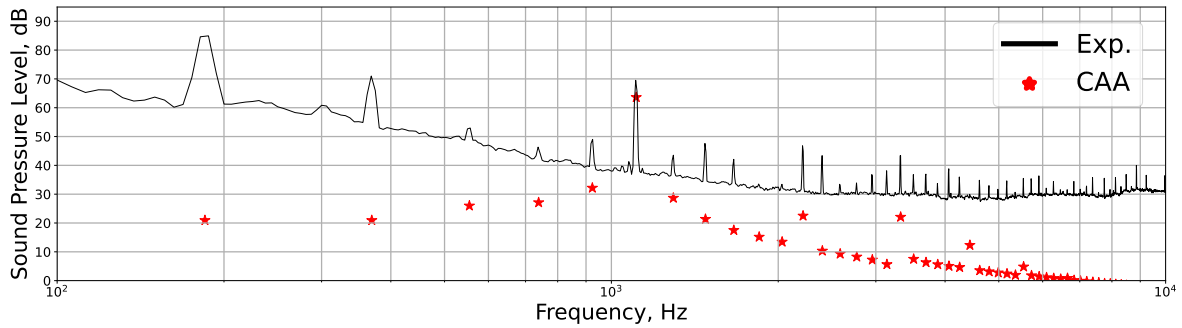



Figure 83: Comparison of CAA results with experiments, narrow band plot, Three Propellers Phase 0°, Mic 90°, Pressure Side mics, tonal component

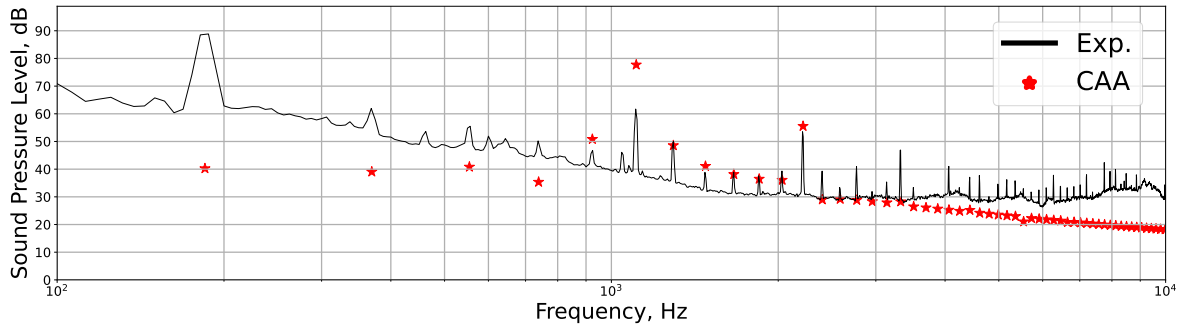



Figure 84: Comparison of CAA results with experiments, narrow band plot, Three Propellers Phase 0°, Mic 90°, Suction Side mics, tonal component

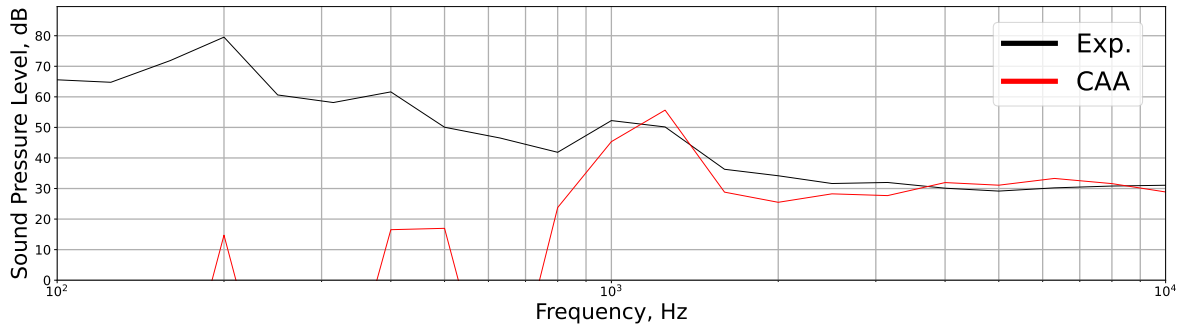



Figure 85: Comparison of CAA results with experiments, third octave band plot, Three Propellers Phase 0°, Mic 90°, Pressure Side mics, tonal + broadband components

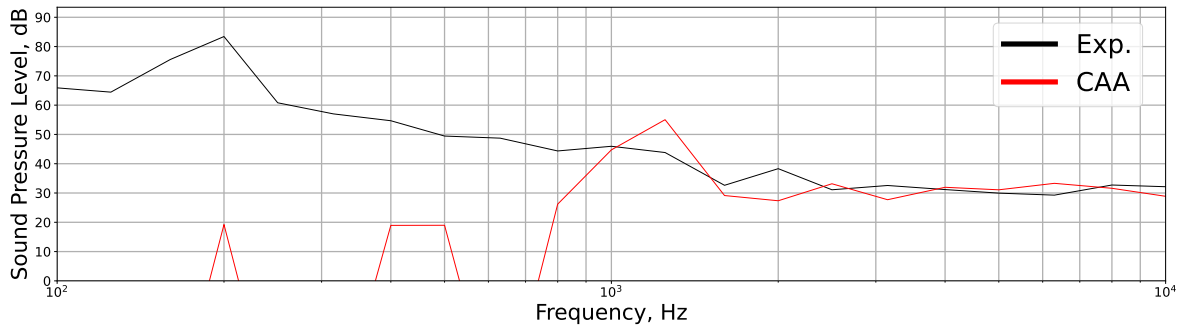



Figure 86: Comparison of CAA results with experiments, third octave band plot, Three Propellers Phase 0°, Mic 90°, Suction Side mics, tonal + broadband components

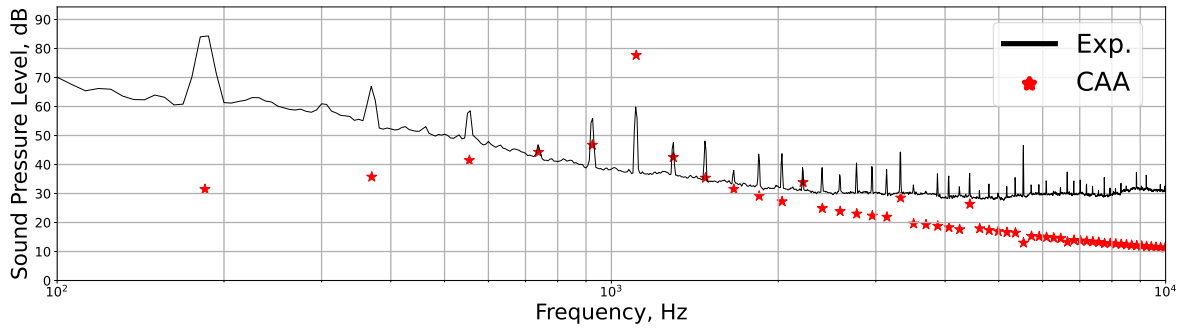



Figure 87: Comparison of CAA results with experiments, narrow band plot, Three Propellers Phase 30°, Mic 90°, Pressure Side mics, tonal component

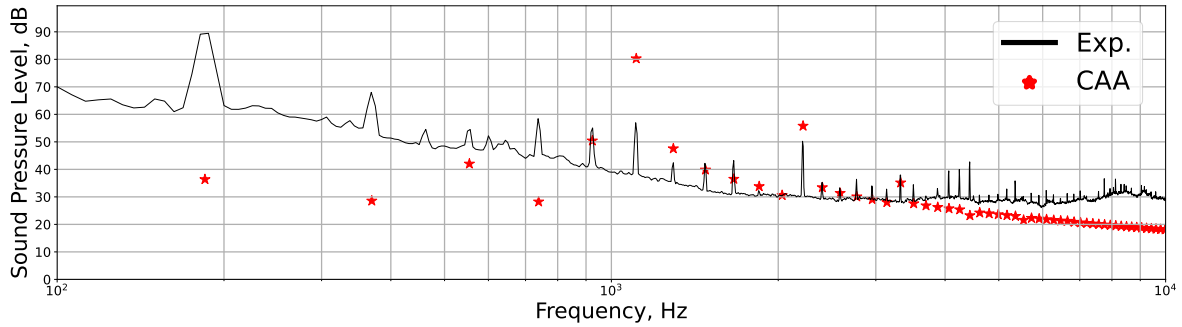



Figure 88: Comparison of CAA results with experiments, narrow band plot, Three Propellers Phase 30°, Mic 90°, Suction Side mics, tonal component

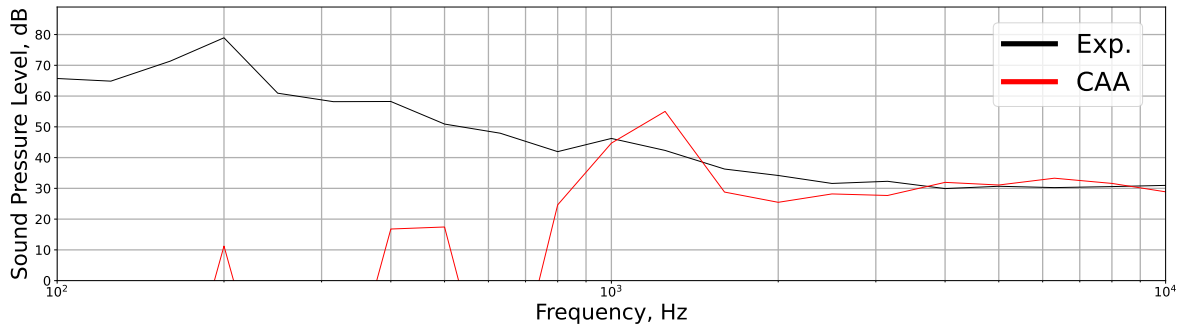



Figure 89: Comparison of CAA results with experiments, third octave band plot, Three Propellers Phase 30°, Mic 90°, Pressure Side mics, tonal + broadband components

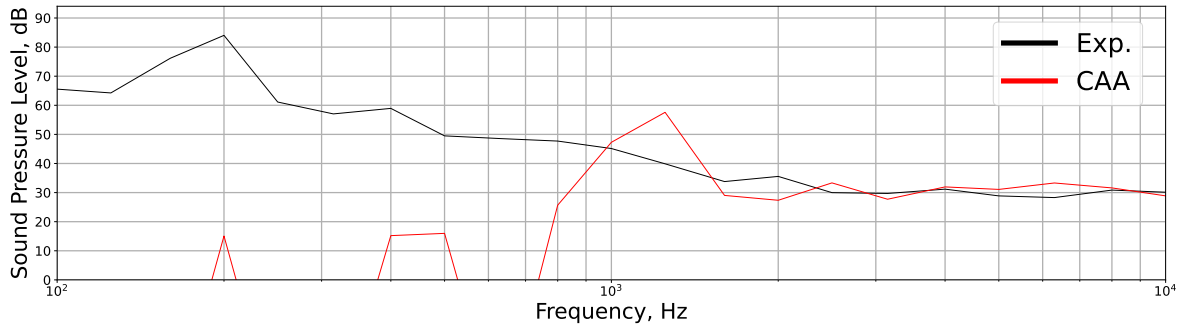



Figure 90: Comparison of CAA results with experiments, third octave band plot, Three Propellers Phase 30°, Mic 90°, Suction Side mics, tonal + broadband components

### 4.3.3 Computational Cost of the Model

The computational cost of each simulation step is:

- 2D RANS for AD table creation: $128 Cores \cdot 15 BladeSections \cdot 3 Hours = 5760 CoreHours$
- 3D AD RANS to generate background meanflow and AD solution for CAA: $1280 Cores \cdot 8 Hours = 10240 CoreHours$
- 3D CAA tonal noise prediction: $2048 Cores \cdot 1 Hour = 2048 CoreHours$
- 2D CFD-CAA trailing edge broadband noise prediction: $128 Cores \cdot 15 BladeSections \cdot 18 Hours = 34560 CoreHours$
- Analytical Lowson model for leading edge broadband noise prediction: $1 Cores \cdot 15 BladeSections \cdot 40 seconds = 0.166 CoreHours$
- Total Core Hours = $51072.166 CoreHours$

# 5 Conclusions

An advanced CAA method for the prediction of the sound generated from installed rotors has been developed, based on AD RANS simulations that would provide the background flow solution for the acoustics approach proposed. The CAA method includes regularised line-distributed sources of strengths derived from the AD surface loads obtained from the RANS calculation, or line sources prescribed based on BET. The rotor noise source model proposed is applied in combination with the LEE system of perturbation equations. The aim of the method introduced in this work is to reduce the computational cost of CFD-CAA tool-chains for installation noise predictions of unconventional rotor configurations, at an acceptable level of accuracy. The test cases considered confirm the model capability of adequately predicting the different sound response of the configurations investigated. Further validation of the approach proposed with available experimental data will be considered in the future.

.

# References


Akkermans, R., Bernicke, P., Ewert, R., and Dierke, J. (2018). Zonal overset-les with stochastic volume forcing. *International Journal of Heat and Fluid Flow*, 70:336 – 347. http://doi.org/10.1016/j.ijheatfluidflow.2017.11.005.

Ananthan, V. B., Dierke, J., Ewert, R., and Kreuzinger, J. (2022). Wall-modelled les on hierarchical cartesian mesh for trailing edge noise prediction. *28th AIAA/CEAS Aeroacoustics 2022 Conference*. https://doi.org/10.2514/6.2022-2801.

Appel, C. (2023). Caa based noise prediction for wind energy turbines. *AIAA 2023-3739. AIAA AVIATION 2023 Forum*. https://doi.org/10.2514/6.2023-3739.

Bassetti, A. (2009). A statistical jet-noise model based on the acoustic analogy and a rans solution. *University of Southampton, Institute of Sound and Vibration Research*. http://eprints.soton.ac.uk/id/eprint/64784.

Batchelor, G. (1960). The theory of homogeneous turbulence. *Cambridge University Press*. https://doi.org/10.2307/3609796.

Bauer, M., Dierke, J., and Ewert, R. (2009). Application of a discontinuous galerkin method to predict airframe noise. *15th AIAA/CEAS Aeroacoustics Conference, Miami, Florida, USA*. https://doi.org/10.2514/6.2009-3175.

Careta, A., Sagués, F., and Sancho, J. M. (1993). Stochastic generation of homogeneous isotropic turbulence with well-defined spectra. *Physical Review E*. https://doi.org/10.1103/PhysRevE.48.2279.

Cooper, A. J. and Peake, N. (2001). Propagation of unsteady disturbances in a slowly varying duct with mean swirling flow. *Journal of Fluid Mechanics*. https://doi.org/10.1017/S0022112001005559.

Dantinne, G., Jeanmart, H., Winckelmans, G., Legat, V., and Carati, D. (1998). Hyperviscosity and vorticity-based models for subgrid scale modeling. *Applied Scientific Research*, 59:409–420. https://doi.org/10.1023/A:1001179014517.

Dieste, M. and Gabal, G. (2009). Synthetic turbulence applied to broadband interaction noise. *15th AIAA/CEAS Aeroacoustics Conference, Miami, Florida, USA*. https://doi.org/10.2514/6.2009-3267.

Dieste, M. and Gabard, G. (2012). Random particle methods applied to broadband fan interaction noise. *Journal of Computational Physics*. https://doi.org/10.1016/j.jcp.2012.07.044.

do Nascimento Monteiro, F., Ragni, D., Sinnige, T., and Avallone, F. (2023). H2020 enodise: Tud experimental database configuration b1 (v1.0) [data set]. *Zenodo*. https://doi.org/10.5281/zenodo.8307371.

Ehlert, J. (2022). Erprobung eines numerischen simulationsansatzes für das umströmungsgeräusch von flugzeugfahrwerken. *DLR AS-TEA & Technische Universität Braunschweig, Study project report*.

ENODISE (2020-2024). https://www.vki.ac.be/index.php/about-enodise.

Ewert, R. (2006). Slat noise trend predictions using caa with stochastic sources from a random particle mesh method (rpm). *12th AIAA/CEAS Aeroacoustics Conference (27th AIAA Aeroacoustics Conference)*. https://doi.org/10.2514/6.2006-2667.

Ewert, R. (2007). Rpm - the fast random particle-mesh method to realize unsteady turbulent sound sources and velocity fields for caa applications. *13th AIAA/CEAS Aeroacoustics Conference (28th AIAA Aeroacoustics Conference)*. https://doi.org/10.2514/6.2007-3506.

Ewert, R. (2008). Broadband slat noise prediction based on caa and stochastic sound sources from a fast random particle-mesh (rpm) method. *Computers & Fluids*. https://doi.org/10.1016/j.compfluid.2007.02.003.

Ewert, R. (2016). Canonical stochastic realization of turbulent sound sources via forced linear advection-diffusion-dissipation equation. *22nd AIAA/CEAS Aeroacoustics Conference*. https://doi.org/10.2514/6.2016-2965.

Ewert, R., Dierke, J., Appel, C., and Herr, M. (2009). Rans/caa based prediction of naca 0012 broadband trailing edge noise and experimental validation. *15th AIAA/CEAS Aeroacoustics Conference, Miami, Florida, USA*. https://doi.org/10.2514/6.2009-3269.

Ewert, R., Dierke, J., Neifeld, A., and Alavi Moghadam, S. (2014). Linear and nonlinear perturbation equations with relaxation source terms for forced eddy simulation of aeroacoustic sound generation. *20th AIAA/CEAS Aeroacoustics Conference*. https://doi.org/10.2514/6.2014-3053.

Ewert, R., Dierke, J., Siebert, J., Neifeld, A., Siefert, M., and Kornow, O. (2011). Caa broadband noise prediction for aeroacoustic design. *Journal of Sound and Vibration*. https://doi.org/10.1016/j.jsv.2011.04.014.

Ewert, R. and Edmunds, R. (2005). Caa slat noise studies applying stochastic sound sources based on solenoidal digital filters. *11th AIAA/CEAS Aeroacoustics Conference*. https://doi.org/10.2514/6.2005-2862.

Ewert, R. and Kreuzinger, J. (2021). Hydrodynamic/acoustic splitting approach with flow-acoustic feedback for universal subsonic noise computation. *Journal of Computational Physics*. https://doi.org/10.1016/j.jcp.2021.110548.

Ewert, R., Neifeld, A., and Boenke, D. (2017). Simulation of cold jet installation noise using a stochastic backscatter model. *23rd AIAA/CEAS Aeroacoustics Conference*. https://doi.org/10.2514/6.2017-3017.

Ewert, R., Neifeld, A., and Wohlbrandt, A. (2012). A three-parameter langevin model for hot jet mixing noise prediction. *AIAA 2012-2238*. https://doi.org/10.2514/6.2012-2238.

Ewert, R. and Schroeder, W. (2003). Acoustic perturbation equations based on flow decomposition via source filtering. *Journal of Computational Physics*, 188:365–398. https://doi.org/10.1016/S0021-9991(03)00168-2.

Franco, A., Ewert, R., Moessner, M., and Delfs, J. W. (2021). Towards a fast non-empiric source model for installed rotor noise. *AIAA 2021-2240. AIAA AVIATION 2021 FORUM*. https://doi.org/10.2514/6.2021-2240.

Franco, A., Moessner, M., Ewert, R., and Delfs, J. (2022). Fast non-empiric tonal noise prediction model for installed propulsors. *28th AIAA/CEAS Aeroacoustics 2022 Conference*. https://doi.org/10.2514/6.2022-2961.

Gerhold, T. (2005). Overview of the hybrid rans code tau. *Notes on Numerical Fluid Mechanics and Multidisciplinary Design, vol 89. Springer*. https://doi.org/10.1007/3-540-32382-1_5.

Gohardani, A. S., Doulgeris, G., and Singh, R. (2011). Challenges of future aircraft propulsion: A review of distributed propulsion technology and its potential application for the all electric commercial aircraft. *Progress in Aerospace Sciences*, 47:369–391. https://doi.org/10.1016/j.paerosci.2010.09.001.

Goldstein, M. E. (1978). Unsteady vortical and entropic disturbances of potential flows round arbitrary obstacles. *Journal of Fluid Mechanics*. https://doi.org/10.1017/S0022112078002682.

Goldstein, M. E. (2003). A generalized acoustic analogy. *J. Fluid Mech.*, 488:315–333. https://doi.org/10.1017/S0022112003004890.

Golubev, V. V. and Atassi, H. M. (1998). Acoustic-vorticity waves in swirling flows. *Journal of Sound and Vibration*. https://doi.org/10.1006/jsvi.1997.1049.

Gutin, L. (1948). On the sound field of a rotating propeller. *NACA TM-1195*.

Hanson, D. B. (1980). Influence of propeller design parameters on far-field harmonic noise in forward flight. *AIAA Journal*, 18:1313–1319. https://doi.org/10.2514/3.50887.

Herr, M., Ewert, R., Faßmann, B., Rautmann, C., Martens, S., Rohardt, C., and Suryadi, A. (2018). Noise reduction technologies for wind turbines. *New Results in Numerical and Experimental Fluid Mechanics XI*, pages 611–621. https://doi.org/10.1007/978-3-319-64519-3_55.

Kloeden, P. E. and Platen, E. (2013). Numerical solution of stochastic differential equations. *Springer Berlin, Heidelberg*. https://doi.org/10.1007/978-3-662-12616-5.

Lewy, S. (2010). Semi-empirical prediction of tone noise due to counter-rotating open rotors. *Proceedings of 20th International Congress on Acoustics*. https://www.acoustics.asn.au/conference_proceedings/ICA2010/cdrom-ICA2010/papers/p113.pdf.

Lighthill, M. J. (1952). On sound generated aerodynamically: I. General theory. *Proc. R. Soc. London Ser. A*. https://doi.org/10.1098/rspa.1952.0060.

Lim, S., Garbo, A., Bekemeyer, P., Appel, C., Ewert, R., and Delfs, J. (2022). High-fidelity aerodynamic and aeroacoustic multi-objective bayesian optimization. *AIAA AVIATION 2022 Forum*. https://doi.org/10.2514/6.2022-3354.

Lowson, M. (1993). Assessment and prediction of wind turbine noise. *Energy Technology Support Unit*.

Lowson, M. V. and Lighthill, M. J. (1965). The sound field for singularities in motion. *Proceedings of the Royal Society of London*, 286:559–572. https://doi.org/10.1098/rspa.1965.0164.

Morris, P. and Boluriaan, S. (2004). The prediction of jet noise from cfd data. *AIAA Pap. 2004-2977*. https://doi.org/10.2514/6.2004-2977.

Mühlbauer, B., Ewert, R., Kornow, O., and Noll, B. (2010). Evaluation of the rpm approach for the simulation of broadband combustion noise. *AIAA Journal*. https://doi.org/10.2514/1.45535.

Neifeld, A. and Ewert, R. (2018). Towards forced eddy simulation of airframe induced noise radiation from coherent hydrodynamic structures of jet flow. *2018 AIAA/CEAS Aeroacoustics Conference*. https://doi.org/10.2514/6.2018-3463.

Neifeld, A., Ewert, R., Steger, M., and Rose, M. (2013). Prediction of hot jet mixing noise using extended stochastic source correlations. *AIAA 2013-2040*. https://doi.org/10.2514/6.2013-2040.

Peake, N. and Crighton, D. (1991). An asymptotic theory of near-field propeller acoustics. *Journal of Fluid Mechanics*, 232:285–301. https://doi.org/10.1017/S0022112091003695.

Pope, S. (2000). Turbulent flows. *Cambridge University Press*. https://doi.org/10.1017/CBO9780511840531.

Reiche, N., Ewert, R., and Delfs, J. (2016). Realization of arbitrary vorticity spectra using generic stochastic turbulence. *22nd AIAA/CEAS Aeroacoustics Conference*. https://doi.org/10.2514/6.2016-2964.

Romani, G., Ye, Q., Avallone, F., Ragni, D., and D., C. (2020). Numerical analysis of fan noise for the nova boundary-layer ingestion configuration. *Aerospace Science and Technology*, 96. https://doi.org/10.1016/j.ast.2019.105532.

Shivashankara, B., Johnson, D., and R., C. (1990). Installation effects on counter rotating propeller noise. *13th Aeroacoustics Conference, AIAA*. https://doi.org/10.2514/6.1990-4023.

Siefert, M. and Ewert, R. (2009). Sweeping sound generation in jets realized with a random particle-mesh method. *AIAA Pap. 2009-3369*. https://doi.org/10.2514/6.2009-3369.

Sinnige, T., Ragni, D., Eitelberg, G., and M., V. L. L. (2017). Mitigation of pusher-propeller installation effects by pylon trailing-edge blowing. *Journal of Aircraft*, 54:292–300. https://doi.org/10.2514/1.C034000.

Smith, M. (1981). A prediction procedure for propeller aircraft flyover noise based on empirical data. *SAE Technical Paper 810604*. https://doi.org/10.4271/810604.

Tam, C. and Auriault, L. (1999). Jet mixing noise from fine-scale turbulence. *AIAA Journal*. https://doi.org/10.2514/2.691.

Tam, C. and Webb, J. (1993). Dispersion-relation-preserving finite difference schemes for computational acoustics. *Journal of Computational Physics*. https://doi.org/10.1006/jcph.1993.1142.

Tam, C. K. W. (2004). Computational aeroacoustics: An overview of computational challenges and applications. *International Journal of Computational Fluid Dynamics*, 18:547–567. https://doi.org/10.1080/10618560410001673551.

Tanna, H. K., Burrin, R. H., and Plumblee, H. E. (1981). Installation effects on propeller noise. *Journal of Aircraft*, 18:303–309. https://doi.org/10.2514/3.44703.

Thompson, K. W. (1987). Time-dependent boundary conditions for hyperbolic systems. *J. Comp. Phys. 68, 1-24*. https://doi.org/10.1016/0021-9991(87)90041-6.

Thompson, K. W. (1990). Time-dependent boundary conditions for hyperbolic systems, ii. *J. Comp. Phys. 89, 439-461*. https://doi.org/10.1016/0021-9991(90)90152-Q.

Uhl, P., Schell, A., Ewert, R., and Delfs, J. (2023). Validation of the fast random particle-mesh method for broadband caa of a forward facing step and its prediction sensitivity for geometrical modifications. *2023 AIAA Aviation and Aeronautics Forum and Exposition*. https://doi.org/10.2514/6.2023-3499.

Wall, T. J. and Meyer, R. T. (2017). A survey of hybrid electric propulsion for aircraft. *53rd AIAA/SAE/ASEE Joint Propulsion Conference*. https://doi.org/10.2514/6.2017-4700.

Wohlbrandt, A., Hu, N., Guérin, S., and Ewert, R. (2016). Analytical reconstruction of isotropic turbulence spectra based on the gaussian transform. *Computers & Fluids*, 132:46–50. https://doi.org/10.1016/j.compfluid.2016.03.023.

Zaman, I., Zang, B., Azarpeyvand, M., and Falsi, M. (2023a). H2020 enodise: Ubri experimental aeroacoustic database bli configuration a (v1.2.1) [data set]. *Zenodo*. https://doi.org/10.5281/zenodo.10118963.

Zaman, I., Zang, B., Azarpeyvand, M., and Falsi, M. (2023b). H2020 enodise: Ubri experimental aeroacoustic database bli configuration a (v1.2.1) [data set]. *Zenodo*. https://doi.org/10.5281/zenodo.10118963.

# A Appendix

## A.1 Fast Random Particle-Mesh Method

### A.1.1 Theoretical background

Analytically, a fluctuating component $\psi_i$ is obtained through the convolution of spatial white-noise $\mathcal{U}_i$ with a filter kernel,

$$\psi_i(\boldsymbol{x},t) = \int_{V_S^n} \hat{A} G(\boldsymbol{x}-\boldsymbol{x}') \mathcal{U}_i(\boldsymbol{x}',t)\, \mathrm{d}^n x'. \tag{98}$$

In this expression $G$ is a spatial filter kernel, $n$ indicates the dimension of the problem, and $V_S^n$ is the considered source region (usually a sub domain of the resolved acoustic domain). The scaling function $\hat{A}$ realizes the desired variance of $\psi_i$. Here it is assumed to be a function of either $\boldsymbol{x}$ or $\boldsymbol{x}'$. The number of components realized depends on the kind of source application. For example, for the generation of velocity fields in 2-D one scalar field is used ($m = 1$), in 3-D three fields must be chosen ($m = 3$).

To realize frozen turbulence $m$ mutually uncorrelated spatiotemporal white-noise fields $\mathcal{U}_i(\boldsymbol{x},t)$ have to be used, which are defined by

$$\langle \mathcal{U}_i(\boldsymbol{x},t)\rangle = 0 \tag{99}$$

$$\langle \mathcal{U}_i(\boldsymbol{x},t)\mathcal{U}_j(\boldsymbol{x}+\boldsymbol{r},t)\rangle = \rho_0(\boldsymbol{x})^{-1}\delta_{ij}\delta(\boldsymbol{r}) \tag{100}$$

$$\frac{D_0\mathcal{U}_i}{Dt} = 0. \tag{101}$$

The brackets in Eqs. (99-101) denote an ensemble average, $D_0/Dt = \partial/\partial t + \boldsymbol{u}_0 \cdot \boldsymbol{\nabla}$ denotes a substantial derivative based on a convection velocity field $\boldsymbol{u}_0$, $\delta(\boldsymbol{r})$ is the Dirac delta function, and $\delta_{ij}$ the Kronecker symbol. The steady velocity field $\boldsymbol{u}_0$ usually is associated to the RANS mean-flow, but could also be chosen differently (e.g. in the Tam & Auriault jet noise model it is taken as $\boldsymbol{u}_0 = (\bar{u},0,0)^T$, with $\bar{u} = u_{jet}$). The density $\rho_0$ is defined by

$$\boldsymbol{\nabla} \cdot (\rho_0 \boldsymbol{u}_0) = 0. \tag{102}$$

The novelty of this approach rests upon the introduction of the concept of 'convective white-noise'. Eq. (101) is a hyperbolic convection equation based on the convection operator $D_0/Dt$ such that a solution of $\mathcal{U}_i$ is completely specified in the computational source domain by the initial conditions posed at the inflow boundary. If $\mathcal{U}_i$ satisfies Eq. (100) at the inflow boundary, it is not for granted that Eq. (100) still holds in the rest of the computational domain. A proof showing that Eqs. (100) and (101) can be realized simultaneously was given in Ewert (2007); Mühlbauer et al. (2010).

The substantial or material derivative in Eq. (101) specifies the property of $\mathcal{U}_i$ to remain locally frozen for an observer comoving at speed $\boldsymbol{u}_0$. For small two-point separations $\boldsymbol{r}$ the Eqs. (100) and (101) can be written more compactly as

$$\langle \mathcal{U}_i(\boldsymbol{x},t)\mathcal{U}_j(\boldsymbol{x}+\boldsymbol{r},t+\tau)\rangle = \rho_0(\boldsymbol{x})^{-1}\delta(\boldsymbol{r}-\boldsymbol{u}_0\tau)\,\delta_{ij}. \tag{103}$$

An exponential temporal correlation mechanism can be achieved if each spatial white noise field $\mathcal{U}_i$ is generated with a Langevin equation Pope (2000) in a Lagrangian frame,

i.e.

$$\frac{D_0}{Dt}\mathcal{U}_i = -\frac{1}{\tau_s}\mathcal{U}_i + \sqrt{\frac{2}{\tau_s}}\xi_i. \tag{104}$$

A source term $\xi_i(\boldsymbol{x},t)$ on the right-hand side is associated to each realized field $\mathcal{U}_i$. The source is defined by the properties

$$\langle \xi_i(\boldsymbol{x},t)\rangle = 0, \tag{105}$$

$$\langle \xi_i(\boldsymbol{x},t)\xi_j(\boldsymbol{x}+\boldsymbol{r},t+\tau)\rangle = \rho_0(\boldsymbol{x})^{-1}\delta(\boldsymbol{r}-\boldsymbol{u}_0\tau)\delta(\tau)\delta_{ij}. \tag{106}$$

For sufficiently small spatial and temporal separation $\boldsymbol{r}$ and $\tau$, respectively, the equation analogous to Eq. (103) that follows as a solution of Eq. (104) with source statistic Eq. (106) is

$$\langle \mathcal{U}_i(\boldsymbol{x},t)\,\mathcal{U}_j(\boldsymbol{x}+\boldsymbol{r},t+\tau)\rangle = \rho_0(\boldsymbol{x})^{-1}\delta(\boldsymbol{r}-\boldsymbol{u}_0\tau)\exp(-|\tau|/\tau_s)\,\delta_{ij}, \tag{107}$$

i.e. it incorporates an exponential temporal correlation.

A further temporal correlation model was introduced in Siefert and Ewert (2009), where Eq. (101) was replaced by

$$\frac{D\mathcal{U}_i}{Dt} = 0. \tag{108}$$

The velocity field in this convection operator is the sum of the steady RANS mean-flow plus the perturbation velocities generated by the synthetic turbulence model itself. These extra velocities introduce diffusion into the model, which effectively causes a temporal decorrelation exhibiting the sweeping similarity law of turbulence (Siefert and Ewert (2009))

With the help of Eq. (98) the cross-covariance of quantity $\psi_i$ is inferred as

$$\begin{aligned}\mathcal{R}_{ij}(\boldsymbol{x},\boldsymbol{r},\tau) &= \langle \psi_i(\boldsymbol{x},t)\psi_j(\boldsymbol{x}+\boldsymbol{r},t+\tau)\rangle = \hat{A}(\boldsymbol{x})\hat{A}(\boldsymbol{x}+\boldsymbol{r})\iint G(\boldsymbol{x}-\boldsymbol{x}')\,G(\boldsymbol{x}+\boldsymbol{r}-\boldsymbol{x}'')\\ &\quad\times\langle \mathcal{U}_i(\boldsymbol{x}',t)\mathcal{U}_j(\boldsymbol{x}'',t+\tau)\rangle\;\mathrm{d}^n x'\,d^n x''.\end{aligned} \tag{109}$$

Introducing Eq. (100) into Eq. (109), choosing a Gaussian filter kernel

$$G(\boldsymbol{x}-\boldsymbol{x}') = \exp\left(-\frac{\pi}{2}\frac{|\boldsymbol{x}-\boldsymbol{x}'|^2}{l_\mathrm{s}^2}\right), \tag{110}$$

and assuming an incompressible convection field, $\boldsymbol{\nabla}\cdot\rho_0\boldsymbol{u}_0 = 0$ with $\rho_0 = const.$, together with a constant time and length scale, $\tau_s$ and $l_\mathrm{s}$, respectively, the cross-covariance realized reads

$$\mathcal{R}_{ij}(\boldsymbol{x},\boldsymbol{r},\tau) = \frac{\hat{A}(\boldsymbol{x})\hat{A}(\boldsymbol{x}+\boldsymbol{r})}{\rho_0}{l_\mathrm{s}}^n\exp\left(-\frac{|\tau|}{\tau_s}-\frac{\pi|\boldsymbol{r}-\boldsymbol{u}_0\tau|^2}{4l_\mathrm{s}^2}\right)\delta_{ij}, \tag{111}$$

i.e. the fluctuating components $\psi_i$ are mutually uncorrelated. Eq. (111) is exact under the assumptions given. For inhomogeneous turbulence $\tau_\mathrm{s}$, $l_\mathrm{s}$, and $\rho_0$ depend on position $\boldsymbol{x}$. Then Eq. (111) is still a very good approximation to the actually achieved cross-covariance if the fields are not varying too fast on a spatial scale defined by the local turbulent length scale $l_s$. This constraint perhaps could be deemed automatically satisfied by any RANS solution as a condition mandatory for self-consistent turbulent statistics. The variance of the fluctuations is inferred as

$$\hat{R} = \left\langle \psi_i(\boldsymbol{x},t)^2\right\rangle = \mathcal{R}_{ij}(\boldsymbol{x},0,0) = \frac{\hat{A}(\boldsymbol{x})^2 l_\mathrm{s}^n}{\rho_0}. \tag{112}$$

Hence, to achieve a certain source variance $\hat{R}$ the parameter $\hat{A}$ must be

$$\hat{A} = \sqrt{\frac{\rho_0 \hat{R}}{l_s^n}}. \tag{113}$$

Eq. (113) defines the scaling of amplitude $\hat{A}$ as a function of position $\boldsymbol{x}$. However, it is also applied, if the amplitude in Eq. (98) is defined as a function $\hat{A}(\boldsymbol{x}')$. For the latter case it can be shown that the realized variance not exactly follows the target variance $\hat{R}$, rather an effective variance is achieved, which is the target variance smoothed out with a normalized Gaussian filter based on the local length scale $l_s$.

The cross-correlation of a component $\psi_i$ is defined by

$$R = \frac{\langle \psi_i(\boldsymbol{x}, t)\psi_i(\boldsymbol{x}+\boldsymbol{r}, t+\tau)\rangle}{\sqrt{\langle \psi_i(\boldsymbol{x}, t)^2\rangle \langle \psi_i(\boldsymbol{x}+\boldsymbol{r}, t+\tau)^2\rangle}}, \tag{114}$$

and for slowly varying $l_s$ and $\rho_0$, i.e. $l_s(\boldsymbol{x}+\boldsymbol{r}) \simeq l_s(\boldsymbol{x})$, $\rho_0(\boldsymbol{x}+\boldsymbol{r}) \simeq \rho_0(\boldsymbol{x})$ it becomes

$$R(\boldsymbol{x}, \boldsymbol{r}, \tau) = \exp\left(-\frac{|\tau|}{\tau_s} - \frac{\pi|\boldsymbol{r} - \boldsymbol{u}_0\tau|^2}{4l_s^2}\right). \tag{115}$$

The exponential temporal correlation function is entirely specified by the convective white-noise definition, i.e. Eq. (107). The spatial correlation function $R(\boldsymbol{x}, \boldsymbol{r}, 0)$, on the contrary, is defined by the shape of the spatial filter kernel. More precisely,

$$R(\boldsymbol{x}, \boldsymbol{r}, 0) = \alpha^{-1} \int G(\boldsymbol{x} - \boldsymbol{x}')G(\boldsymbol{x} + \boldsymbol{r} - \boldsymbol{x}')\mathrm{d}^n\boldsymbol{x}' = \alpha^{-1} G \star G,$$

where $\alpha = \int G(\boldsymbol{y})^2 \mathrm{d}^n\boldsymbol{y}$. That is, the spatial correlation function results from the self-convolution of the filter kernel function. Based on the filter kernel Eq. (110) with fixed length scale parameter $l_s$ the spatial correlation function is isotropic and depends only on radial distance $r$. The integral length scale of the spatial correlation function is given by

$$L_i = \int_0^\infty R(r, 0)\mathrm{d}r.$$

For the spatial correlation function $R = G \star G$ the integral length scale is defined by the length scale parameter, i.e. $L_i = l_s$.

### A.1.2 Random particle concept

Two different numerical methods have been introduced in previous work for the discretization of the (F)RPM approach. Both approaches represent the convecting white noise field by convecting particles, which carry random values. The concept of random particles emerges if the computational source domain is divided into $N$ non-overlapping control volumes (CV) $\delta V_k$. The boundary of each CV represents a liquid line that floats with the mean-flow field such that each CV encompasses an invariant fluid mass

$$\delta m_k = \int_{\delta V_k(t)} \rho_0 \, \mathrm{d}^n x \tag{116}$$

and the position of its center of mass (CM)

$$\boldsymbol{x}_k^c(t) = \frac{1}{\delta m_k} \int_{\delta V_k(t)} \rho_0 \boldsymbol{x} \, \mathrm{d}^n x \tag{117}$$

is in motion. For sufficiently small CVs the CM drift velocity corresponds to the mean-flow velocity at the CM position Ewert (2008), refer to the Appendix.

The numerical quadrature of Eq. (98) is realized by the weighted sum over all $N$ control volumes Ewert (2008), i.e.

$$\psi_i(\boldsymbol{x}, t) \simeq \hat{A}(\boldsymbol{x}) \sum_{k=1}^{N} G\left(\boldsymbol{x} - \boldsymbol{x}_k^c(t)\right) \frac{r_{ik}(t)}{\rho_0(\boldsymbol{x}_k^c)}. \tag{118}$$

Here $m \times N$ new variables $r_{ik}$ are defined by the integration of the $i = 1 \ldots m$ white noise fields over each control volume, i.e.

$$r_{ik}(t) := \int_{\delta V_k(t)} \rho_0(\boldsymbol{x}') \, \mathcal{U}_i(\boldsymbol{x}', t) \, \mathrm{d}^n x'. \tag{119}$$

The properties of the random variables $r_{ik}$ are derived subequently as a consequence of the definitions given by Eqs. (99-101).

### A.1.3 Derivation of particle velocity

The position of a specific point $\boldsymbol{x}$ inside a specific control volume (CV), say $\delta V_k$, at time level $t$ is associated to a drifted location $\boldsymbol{x}'$ at time level $t + \Delta t$ through a function $\boldsymbol{x}'(\boldsymbol{x})$, which can be approximated via

$$\boldsymbol{x}' = \boldsymbol{x} + \boldsymbol{u}_0(\boldsymbol{x}, t)\Delta t + \mathcal{O}\left(\Delta t^2\right). \tag{120}$$

Taylor expansion of the mean velocity around the center of the CV yields

$$\boldsymbol{u}_0(\boldsymbol{x}, t) = \boldsymbol{u}_0^c + \boldsymbol{\nabla} \boldsymbol{u}_0^c \left(\boldsymbol{x} - \boldsymbol{x}_k^c(t)\right) + \mathcal{O}\left(\Delta x^2\right), \tag{121}$$

where $\Delta x$ is a measure of the size of the CV. The CM position at time-level $t + \Delta t$ can be expressed via

$$\boldsymbol{x}_k^c(t + \Delta t) = \frac{1}{\delta m_k} \int_{\delta V_k(t)} \rho_0 \boldsymbol{x}'(\boldsymbol{x}) \, \mathrm{d}^n x. \tag{122}$$

Introducing the approximation to the mapping function $\boldsymbol{x}'(\boldsymbol{x})$ yields

$$\boldsymbol{x}_k^c(t+\Delta t) = \frac{1}{\delta m_k} \int_{\delta V_k(t)} \rho_0 \left[\boldsymbol{x} + \boldsymbol{u}_0^c \Delta t + \boldsymbol{\nabla} \boldsymbol{u}_0^c \left(\boldsymbol{x} - \boldsymbol{x}_k^c(t)\right) \Delta t + \mathcal{O}\left(\Delta x^2\right) \Delta t + \mathcal{O}\left(\Delta t^2\right)\right] \, \mathrm{d}^n x. \tag{123}$$

With the help of definitions Eqs. (116,117) the integral can be solved term wise, yielding

$$\boldsymbol{x}_k^c(t + \Delta t) = \boldsymbol{x}_k^c(t) + \boldsymbol{u}_0^c \Delta t + \boldsymbol{\nabla} \boldsymbol{u}_0^c \boldsymbol{x}_k^c(t) - \boldsymbol{\nabla} \boldsymbol{u}_0^c \boldsymbol{x}_k^c(t) + \mathcal{O}\left(\Delta x^2\right) \Delta t + \mathcal{O}\left(\Delta t^2\right). \tag{124}$$

From this relationship the velocity of the CM of the CV becomes in the limit $\Delta t \to 0$

$$\dot{\boldsymbol{x}}_k^c(t) = \boldsymbol{u}_0^c + \mathcal{O}\left(\Delta x^2\right). \tag{125}$$

### A.1.4 Frozen turbulence

In total $m \times N$ new variables $r_{ik}$ are defined by the integration of the $i = 1 \ldots m$ white noise fields over each control volume, i.e.

$$r_{ik}(t) := \int_{\delta V_k(t)} \rho_0(\boldsymbol{x}\,') \, \mathcal{U}_i\,(\boldsymbol{x}\,', t)\, \mathrm{d}^n x'. \tag{126}$$

Using the properties of the white noise field as defined by Eqs. (99-101) the essential properties of $r_{ik}$ can be established. With the help of Eq. (99) it is readily shown that the ensemble average of $r_{ik}$ vanishes, i.e.

$$\langle r_{ik}(t) \rangle = \int_{\delta V_k(t)} \rho_0(\boldsymbol{x}\,') \;\langle \mathcal{U}_i\,(\boldsymbol{x}\,', t) \rangle \, \mathrm{d}^n x' = 0. \tag{127}$$

With the help of Eq. (100) the variance of $r_{ik}$ can be evaluated:

$$\langle r_{ik}(t) r_{jl}(t) \rangle = \int_{\delta V_k(t)} \int_{\delta V_l(t)} \rho_0(\boldsymbol{x}\,') \rho_0(\boldsymbol{x}\,'') \, \langle \mathcal{U}_i(\boldsymbol{x}\,', t) \mathcal{U}_j(\boldsymbol{x}\,'', t) \rangle \, \mathrm{d}^n x\,' \mathrm{d}^n x\,'' = \delta_{ij} \delta_{kl} \delta m_k. \tag{128}$$

The explicit result on the right-hand side of Eq. (128) follows by utilizing Eq. (100) and taking into account Eq. (116). The change of variable $r_{ik}$ over time follows by differentiating Eq. (119), i.e.

$$\dot{r}_{ik} = \frac{\mathrm{d}}{\mathrm{d}t} \int_{\delta V_k(t)} \rho_0(\boldsymbol{x}\,') \, \mathcal{U}_i\,(\boldsymbol{x}\,', t)\, \mathrm{d}^n x'. \tag{129}$$

By means of the Reynolds transport theorem the integration can be solved yielding together with $\boldsymbol{\nabla} \cdot (\rho_0 \boldsymbol{u}_0) = 0$

$$\dot{r}_{ik} = \int_{\delta V_k(t)} \rho_0(\boldsymbol{x}\,') \frac{D_0}{Dt} \mathcal{U}_i\,(\boldsymbol{x}\,', t)\, \mathrm{d}^n x' = 0. \tag{130}$$

Due to Eq. (101) the substantial time derivative is zero, hence the whole integral equals zero. Altogether the properties of $r_{ik}$ are

$$\begin{aligned}
\langle r_{ik}(t) \rangle &= 0 && (131)\\
\langle r_{ik}(t) r_{jl}(t) \rangle &= \delta_{ij}\delta_{kl}\; \delta m_k && (132)\\
\dot{r}_{ik} &= 0 && (133)\\
\dot{\boldsymbol{x}}_k^c &= \boldsymbol{u}_0\,(\boldsymbol{x}\,_k^c)\,. && (134)
\end{aligned}$$

To summarize the result, the $r_{ik}$ can be deemed to represent mutually un-correlated random variables with vanishing mean, Eq. (131), and a constant variance proportional to $\delta m_k$, Eq. (132). A set of random variables is associated to a 'particle' at position $x_k^c$ that drifts at the local mean flow velocity, Eq. (134). The random values remains constant over time, Eq. (133). The filter integral of the (F)RPM approach, Eq. (98), becomes a discrete sum over all drifting particles evenly distributed over the source domain. section

### A.1.5 Exponential time de-correlation

For frozen turbulence the random values remain constant. In case of an exponential decay as prescribed by Eq. (104) the properties of the random variable $r_{ik}$ are modified. Using Eq. (130) the substantial time derivative inside the integral can be replaced by the right-hand side of Eq. (104). This yields

$$\dot{r}_{ik} = -\int_{\delta V_k(t)} \rho_0(\boldsymbol{x}\,')\frac{1}{\tau_s}\mathcal{U}_i \mathrm{d}^n x' + \int_{\delta V_k(t)} \rho_0(\boldsymbol{x}\,')\sqrt{\frac{2}{\tau_s}}\xi_i \mathrm{d}^n x'. \tag{135}$$

Assuming the time scale $\tau_s$ not to vary too rapidly over space so that its spatial distribution is well approximated using a constant averaged value over a CV, the first integral equals the definition of $r_{ik}$, Eq. (119), divided by the time scale $\tau_s$. If a second random variable $s_i$ is introduced via

$$s_{ik}(t) = \int_{\delta V_k(t)} \rho_0(\boldsymbol{x}\,')\ \xi_i\left(\boldsymbol{x}\,', t\right) \mathrm{d}^n x' = 0, \tag{136}$$

a Langevin equation for the random variable $r_{ik}$ is obtained:

$$\dot{r}_{ik} = -\frac{1}{\tau_s} r_{ik} + \sqrt{\frac{2}{\tau_s}} s_{ik}. \tag{137}$$

The properties of random variable $s_{ik}$ can be directly inferred from Eqs. (105) and (106), i.e.

$$\langle s_{ik}(t)\rangle = \int_{\delta V_k(t)} \rho_0(\boldsymbol{x}\,')\ \langle \xi_i\left(\boldsymbol{x}\,', t\right)\rangle \mathrm{d}^n x' = 0 \tag{138}$$

$$\langle s_{ik}(t) s_{jk}(t+\tau)\rangle = \int_{\delta V_k(t)} \mathrm{d}^n x\,' \int_{\delta V_k(t+\tau)} \mathrm{d}^n x\,''\ \rho_0(\boldsymbol{x}\,')\rho_0(\boldsymbol{x}\,'')\ \langle \xi_{ik}(\boldsymbol{x}\,', t)\xi_{jk}(\boldsymbol{x}\,'', t+\tau)\rangle \tag{139}$$

In the last integral the integration over $\delta V_k(t+\tau)$ can be transformed into an integration over $\delta V_k(t)$ using the relation $\boldsymbol{x}\,'' = \boldsymbol{x}\,''' + \boldsymbol{u}_0(x'')\tau$, which maps a point $x'''$ of $\delta V_k(t)$ at time level $t$ to its drifted position on $\delta V_k(t+\tau)$ at time level $t+\tau$. The Jacobian of this transformation is defined by $J := \left|\frac{\partial \boldsymbol{x}\,''}{\partial \boldsymbol{x}\,'''}\right|$. Due to mass conservation the Jacobian must satisfy $J = \frac{d\delta V_k(\boldsymbol{x}\,'')}{d\delta V_k(\boldsymbol{x}\,''')} = \frac{\rho_0(\boldsymbol{x}\,''')}{\rho_0(\boldsymbol{x}\,'')}$. Furthermore, with the help of Eq. (106) the integral becomes

$$\begin{aligned}\langle s_{ik}(t) s_{jk}(t+\tau)\rangle = \int_{\delta V_k(t)} \mathrm{d}^n x\,' \int_{\delta V_k(t)} \mathrm{d}^n x\,'''\ \rho_0(\boldsymbol{x}\,')\rho_0(\boldsymbol{x}\,'')\frac{\delta(\tau)}{\rho_0(\boldsymbol{x}\,')} \\ \cdots \times \delta\left(\boldsymbol{x}\,''' + \boldsymbol{u}_0\tau - \boldsymbol{x}\,' - \boldsymbol{u}_0\tau\right)\delta_{ij}\frac{\rho_0(\boldsymbol{x}\,''')}{\rho_0(\boldsymbol{x}\,'')},\end{aligned}$$

respectively

$$\langle s_{ik}(t) s_{jk}(t+\tau)\rangle = \int_{\delta V_k(t)} \mathrm{d}^n x\,' \int_{\delta V_k(t)} \mathrm{d}^n x\,'''\ \rho_0(\boldsymbol{x}\,''')\delta(\tau)\delta\left(\boldsymbol{x}\,''' - \boldsymbol{x}\,'\right)\delta_{ij}. \tag{140}$$

The integrations can be readily carried out. Furthermore, the result obtained can be easily extended including the case of non-coinciding control volumes $\delta V_l \neq \delta V_k$, since the CVs are non-overlapping and mutually un-correlated, yielding

$$\langle s_{ik}(t) s_{jl}(t+\tau)\rangle = \delta m_k \delta(\tau)\delta_{ij}\delta_{kl}. \tag{141}$$

In other words, $s_{ik}$ represents (temporal) white-noise scaled with a factor of magnitude $\delta m_k$. The solution of the Langevin equation (137) with a source having correlation Eq. (141) yields a correlation of variable $r_{ik}$

$$\langle r_{ik}(t) r_{jl}(t+\tau)\rangle = \delta m_k \delta_{ij}\delta_{kl} \exp\left(-\frac{|\tau|}{\tau_s}\right). \tag{142}$$

For frozen turbulence, i.e. in the limit $\tau_s \to \infty$, the previous result yields in a consistent manner the variance already obtained in Eq. (132) for the same case.

### A.1.6 Two point correlations of homogeneous isotropic turbulence

The two-point velocity cross-correlation between points $\boldsymbol{r}_1$ and $\boldsymbol{r}_2$ and time levels $t_1$ and $t_2$ reads

$$\mathcal{R}_{ij} = \left\langle v_i'(\boldsymbol{r}_1, t_1) v_j'(\boldsymbol{r}_2, t_2)\right\rangle \tag{143}$$

For homogeneous isotropic turbulence, the two-point cross-correlation tensor can be prescribed via

$$\mathcal{R}_{ij}(\boldsymbol{r}, 0) = \overline{v_1'^2}\left\{[f(r) - g(r)]\,\frac{r_i r_j}{r^2} + g(r)\delta_{ij}\right\}, \tag{144}$$

where $\boldsymbol{r} = |\boldsymbol{r}_1 - \boldsymbol{r}_2|$ and $r = |\boldsymbol{r}|$. The variance of the one-component of fluctuating velocity is related to the turbulence kinetic energy budget. For 2-D isotropic turbulence with $k = \overline{v_1'^2 + v_2'^2}/2$ and $\overline{v_1'^2} = \overline{v_2'^2}$ this is $\overline{v_1'^2} = k$.[4]

The functions $f(r)$ and $g(r)$ denote the lateral and longitudinal correlation functions, respectively. For 2-D homogeneous isotropic turbulence they are related via

$$g(r) = f(r) + r\frac{\mathrm{d}f(r)}{\mathrm{d}r}. \tag{145}$$

For 3-D homogeneous istropic trubulence the velocity correlation tensor is also prescribed by Eq. (144). However, longitudinal and lateral correlation function are linked in 3-D by means of

$$g(r) = f(r) + \frac{r}{2}\frac{\mathrm{d}f(r)}{\mathrm{d}r}. \tag{146}$$

### A.1.7 Derivation of 2-D velocities

As shown by Careta et al. (1993) and demonstrated subsequently, 2-D homogeneous isotropic turbulence is obtained from a scalar vector potential (stream function) generated by means of a homogeneous, isotropic, and stationary Gaussian stochastic process.

We start from fluctuating 2-D velocity components inferred from the derivative of a stream function $\psi$, i.e.

$$v_i' = \epsilon_{ij}\frac{\partial \psi}{\partial x_j}. \tag{147}$$

[4]The turbulence kinetic energy provided by a 2-D RANS solution (e.g. an airfoil section of a wing of infinite wing span) would contain contributions of velocity fluctuations of all three spatial directions.

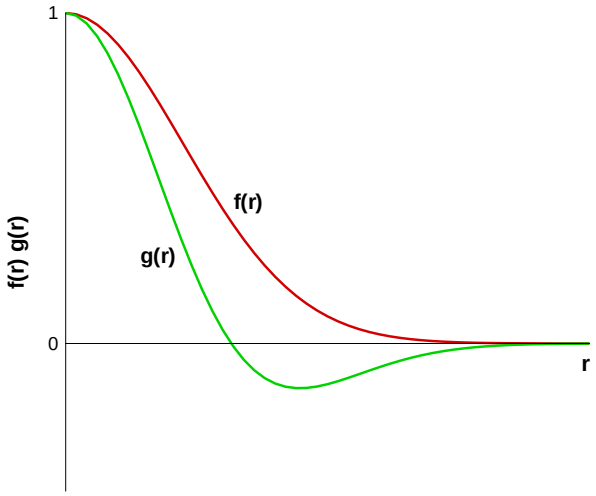



Figure 91: Gaussian longitudinal and lateral correlation functions $f(r)$ and $g(r)$.

The definition ensures divergence-free (solenoidal) 2-D synthetic turbulence, since (summation convention applied to components with similar indices and indices running from 1 to 2)

$$\frac{\partial v_i'}{\partial x_i} = 0. \tag{148}$$

The space-time correlations of the stream function is under the assumption of stationarity and homogeneity of the field a function of $\tau = t_1 - t_2$ and relative separation $\boldsymbol{r} = \boldsymbol{r}_1 - \boldsymbol{r}_2$,

$$\mathcal{C}(\boldsymbol{r}, \tau) = \langle \psi(\boldsymbol{r}_1, t_1)\psi(\boldsymbol{r}_2, t_2)\rangle \,. \tag{149}$$

The velocity correlations Eq. (143) are connected via Eq. (147) with the correlations Eq. (149). Since averaging and differentiation can be exchanged, the relationship is

$$\mathcal{R}_{ij} = \epsilon_{ik}\epsilon_{jl}\frac{\partial^2 \mathcal{C}}{\partial r_{1k}\partial r_{2l}}, \tag{150}$$

where $r_{1k}$ and $r_{2l}$ denote the components $k$ and $l$ of vectors $\boldsymbol{r}_1$ and $\boldsymbol{r}_2$, respectively. Now, isotropy implies that the correlation Eq. (149) for $\tau = 0$ becomes an ordinary function of radial distance, i.e.

$$\mathcal{C}(\boldsymbol{r}, 0) = \mathcal{C}(r), \quad r = |\boldsymbol{r}| = |\boldsymbol{r}_1 - \boldsymbol{r}_2|. \tag{151}$$

Since the radial distance between two points is $r = \sqrt{r_i r_i}$, where the components satisfy the relationship $r_i = r_{1i} - r_{2i}$, the first order derivative with respect to $r_{2j}$ and second order derivatives with respect to $r_{1i}$ and $r_{2j}$ are given by

$$\frac{\partial \mathcal{C}}{\partial r_{2j}} = \frac{\mathrm{d}\mathcal{C}}{\mathrm{d}r}\frac{\partial r}{\partial r_j}\frac{\partial r_j}{\partial r_{2j}} = -\mathcal{C}'\frac{r_j}{r}, \tag{152}$$

respectively

$$\frac{\partial^2 \mathcal{C}}{\partial r_{1i} \partial r_{2j}} = \left( \frac{\mathcal{C}'}{r} - \mathcal{C}'' \right) \frac{r_i r_j}{r^2} - \frac{\mathcal{C}'}{r} \delta_{ij}, \tag{153}$$

where $\mathcal{C}^{n\prime}(r) = \mathrm{d}^n \mathcal{C}(r)/\mathrm{d}r^n$. Then by inserting Eq. (153) in Eq. (150) the velocity cross-correlations in terms of the correlation function $\mathcal{C}(r)$ become

$$\mathcal{R}_{ij} = -\mathcal{C}_0'' \left\{ \left[ \frac{1}{\mathcal{C}_0''} \frac{\mathcal{C}'(r)}{r} - \frac{\mathcal{C}''(r)}{\mathcal{C}_0''} \right] \frac{r_i r_j}{r^2} + \frac{\mathcal{C}''(r)}{\mathcal{C}_0''} \hat{\delta}_{ij} \right\}, \tag{154}$$

where the abbreviation $\mathcal{C}_0'' := \mathcal{C}''(0)$ has been used. The shape of Eq. (154) can be verified to agree formally with Eq. (144). Furthermore, by inspection of Eq. (154) the longitudinal and lateral correlation functions $f(r)$ and $g(r)$ can be identified to be related to the scalar field $C(r)$ via

$$f(r) = \frac{1}{\mathcal{C}_0''} \frac{\mathcal{C}'(r)}{r}, \quad g(r) = \frac{\mathcal{C}''(r)}{\mathcal{C}_0''}. \tag{155}$$

The scaling with $\mathcal{C}_0''$ is introduced in Eq. (154) such that the resulting correlation functions $f(r)$ and $g(r)$ in Eq. (155) are normalized, i.e. $f(0) = g(0) = 1$. Note that $\mathcal{C}''(0)$ also normalizes $f(r)$ by means of l'Hospitals rule, which yields

$$lim_{r \to 0} \frac{\mathcal{C}'(r)}{r} = \mathcal{C}''(0) = \mathcal{C}_0''.$$

Finally, for a complete realization of HIT (in 2-D) the correlation functions $f(r)$ and $g(r)$ have to satisfy the relation Eq. (145). It is easy to prove that Eq. (145) is satisfied when inserting expressions (155) into it: using the definition of $f(r)$ as given by the first equations of Eq. (155), the evaluation of Eq. (145) yields

$$f + r f' = \frac{\mathcal{C}''}{\mathcal{C}_0''}, \tag{156}$$

which corresponds to the definition of $g(r)$ as given in Eq. (155).

To summarize this result, the two-point correlation tensor of homogeneous isotropic turbulence in 2-D is achieved from a scalar stream function, generated by means of a homogeneous, isotropic, and stationary Gaussian stochastic process. The FRPM procedure is well suited to generate an according stream function. In the homogeneous case, where the parameters in are position independent constants, the cross-correlation function of FRPM becomes for $\tau \to 0$

$$\mathcal{R}(\boldsymbol{r}, 0) = \mathcal{C}(r) = \hat{R} \exp\left( -\frac{\pi r^2}{4 l_s^2} \right). \tag{157}$$

The remaining task is to scale the amplitude $\hat{R}$ such that the pre-factor $2/3\overline{k}$ in Eq. (144) is achieved. The velocity correlation Eq. (154) becomes for $r \to 0$ $\mathcal{R}_{ij} = -\mathcal{C}_0'' \hat{\delta}_{ij}$. With the function $\mathcal{C}(r)$ from Eq. (157) the value $\mathcal{C}_0'' = \mathcal{C}''(r = 0) = -\pi/2 l_s^2 \hat{R}$ follows explicitly. Resolving for $\hat{R}$ yields an amplitude value of

$$\hat{R} = \frac{4 l_s^2 \overline{k}}{3\pi}. \tag{158}$$

The resulting longitudinal correlation function that follows from Eqs. (155) and (157) is a Gaussian,

$$f(r) = \exp\left(-\frac{\pi}{4}\frac{r^2}{l_\mathrm{s}^2}\right), \tag{159}$$

with an integral length scale directly determined by the parameter $l_s$,

$$L = \int_0^\infty f(r)\mathrm{d}r = l_\mathrm{s}.$$

Hence, the parameters $\hat{R}$ and $l_s$ are directly linked via Eqs. (158) and (159) to the turbulence kinetic energy $\bar{k}$ and length scale $L$.

### A.1.8 Derivation of 3-D velocities

As was shown in Ewert (2008) 3-D homogeneous isotropic turbulence can be generated in an extension of the 2-D procedure using a vector potential with components defined by three mutually uncorrelated homogeneous, isotropic, and stationary Gaussian processes. To be precise, fluctuating velocities are generated taking the curl of a vector potential $\psi_i$,

$$v_i' = \epsilon_{ijk}\frac{\partial \psi_k}{\partial x_j}. \tag{160}$$

The definition ensures divergence-free (solenoidal) 3-D synthetic turbulence, since (summation convention applied to components with similar indices and indices running from 1 to 3)

$$\frac{\partial v_i'}{\partial x_i} = 0. \tag{161}$$

Then, based on the assumed features of the components of the vector potential, their correlations must satisfy the relationship

$$\mathcal{C}_{ij}(\boldsymbol{r}, \tau = 0) = \langle \psi_i(\boldsymbol{r}_1, t_1)\psi_j(\boldsymbol{r}_2, t_2)\rangle = \delta_{ij}\mathcal{C}(r), \quad r = |\boldsymbol{r}_1 - \boldsymbol{r}_2|. \tag{162}$$

That is, homogeneity and stationarity imply that the two-point correlation is a mere function of relative spatial separation $\boldsymbol{r}$ and time separation $\tau$. Furthermore, isotropy implies that the spatial separation comes into picture only with its relative distance $r = |\boldsymbol{r}|$. Finally, the two-points correlations between equal components are all described through the same function $\mathcal{C}(r)$, but different components are mutually uncorrelated as indicated by the Kronecker delta on the right-hand side of the previous equation.

The velocity cross-correlations Eq. (143) are related to the cross-correlations of the vector stream function components $\mathcal{C}_{ij} = \delta_{ij}C(r)$, i.e., by using Eq. (160),

$$\mathcal{R}_{ij} = \epsilon_{ikl}\epsilon_{jmn}\delta_{ln}\frac{\partial^2 \mathcal{C}(r)}{\partial r_{1k}\partial r_{2m}}. \tag{163}$$

Explicitly written subscripts stand for sampling locations (i.e. either position 1 or position 2), alphanumerical subsrcipts indicate components. The derivatives of function

$\mathcal{C}(r)$ can be computed similar to the 2-D case by utilizing Eq. (152), and the velocity correlation tensor derives as

$$\mathcal{R}_{ij} = -2\mathcal{C}_0'' \left\{ \left[ \frac{\mathcal{C}'/r}{\mathcal{C}_0''} - \frac{\mathcal{C}'' + \mathcal{C}'/r}{2\mathcal{C}_0''} \right] \frac{r_i r_j}{r^2} + \frac{\mathcal{C}'' + \mathcal{C}'/r}{2\mathcal{C}_0''} \hat{\delta}_{ij} \right\}. \tag{164}$$

From Eq. (164) it becomes evident that the formal shape of Eq. (144) can be realized in 3D as well, using a fluctuating vector stream function with statistically independent components. The longitudinal and lateral correlation functions are related in the 3D case to the correlation function of the stream function components $\mathcal{C}(r)$ by

$$f(r) = \frac{1}{\mathcal{C}_0''} \frac{\mathcal{C}'}{r}, \quad g(r) = \frac{\mathcal{C}'' + \mathcal{C}'/r}{2\mathcal{C}_0''}. \tag{165}$$

These expressions differ slightly from their 2-D counterpart, Eq. (155). Note, however, that in 3D the relationship between the longitudinal and lateral correlation function changes from Eq. (145) to Eq. (146), e.g. refer to Batchelor (1960) and Pope (2000).

This relation between the longitudinal and lateral correlation function in 3D is satisfied, which can be shown by inserting the expressions (165) into Eq. (146), i.e.

$$f + \frac{r}{2} f' = \frac{\mathcal{C}'' + \mathcal{C}'/r}{2\mathcal{C}_0''} = g. \tag{166}$$

Hence, fluctuating 3-D velocity fields as derived from the vector potential Eq. (160) in conjunction with three mutually uncorrelated fluctuating stream functions realize the correlation tensor of HIT in 3-D. In comparison with the 2-D results, the additional term for $g(r)$ in Eq. (165) causes the 3-D lateral correlation function to have a less pronounced negative dip compared to the 2-D case, Eq. (155). In 3-D the variance of Eq. (164) has to match the prefactor of Eq. (144), i.e. $-2\mathcal{C}_0'' = 2/3\overline{k} =$. With $\mathcal{C}(r)$ from Eq. (157) and with $\mathcal{C}_0'' = \mathcal{C}''(r=0) = -\pi/2l_s^2\hat{R}$, the amplitude $\hat{R}$ is specified by

$$\hat{R} = \frac{2l_s^2\overline{k}}{3\pi}. \tag{167}$$

The typical shape of the Gaussian longitudinal correlation function $f(r)$ and its associated lateral correlation function $g(r)$ is shown in Fig. 91.

## A.2 Analytical solution FRPM test case

### A.2.1 Far-field spectrum 3-D

Next we will derive an anlytical expression for the far-field spectrum generated by the cross-correlation model

$$\langle q_s(\boldsymbol{x}_1, t_1) q_s(\boldsymbol{x}_1 + \boldsymbol{r}, t_1 + \tau) \rangle = \hat{R} \times \exp\left\{ -\frac{|\tau|}{\tau_s} - \frac{\ln(2)}{l_s^2} \left[ (r_1 - \bar{u}\tau)^2 + r_2^2 + r_3^2 \right] \right\}. \tag{168}$$

Here $\hat{R}$ denotes the variance of the fluctuating source $q_s$. Let $F(\boldsymbol{x}_1, \boldsymbol{r}, \tau)$ denote the two-point cross-correlation of the source between points $\boldsymbol{x}_1$ and $\boldsymbol{x}_2 = \boldsymbol{x}_1 + \boldsymbol{r}$ and at time difference $\tau = t_2 - t_1$ is

$$F(\boldsymbol{x}_1, \boldsymbol{r}, \tau) := \langle q_s(\boldsymbol{x}_1, t_1) q_s(\boldsymbol{x}_1 + \boldsymbol{r}, t_1 + \tau) \rangle. \tag{169}$$

The wave-number frequency spectrum $\hat{H}(\boldsymbol{x}_1, \boldsymbol{\alpha}, \omega)$ related to the two-point cross-correlation is defined through

$$F(\boldsymbol{x}_1, \boldsymbol{r}, \tau) = \frac{1}{2\pi} \iint_{-\infty}^{\infty} \hat{H}(\boldsymbol{x}_1, \boldsymbol{\alpha}, \omega) \exp\left[-i(\omega\tau - \boldsymbol{\alpha}\boldsymbol{r})\right] \mathrm{d}\omega \mathrm{d}^{\mathrm{n}}\boldsymbol{\alpha}. \tag{170}$$

Its back transformation reads

$$\hat{H}(\boldsymbol{x}_1, \boldsymbol{\alpha}, \omega) = \frac{1}{(2\pi)^n} \iint_{-\infty}^{\infty} F(\boldsymbol{x}_1, \boldsymbol{r}, \tau) \exp\left[i(\omega\tau - \boldsymbol{\alpha}\boldsymbol{r})\right] \mathrm{d}\tau \mathrm{d}^{\mathrm{n}}\boldsymbol{r}. \tag{171}$$

Based on these definitions, the spectrum Eq. (32) can be rewritten as

$$\hat{S}(\boldsymbol{x}, \omega) = \iint_{V_s} \int_{-\infty}^{\infty} \hat{p}_a^*(\boldsymbol{x}_1, \boldsymbol{x}, \omega) \hat{p}_a(\boldsymbol{x}_2, \boldsymbol{x}, \omega) \;\; F(\boldsymbol{x}_1, \boldsymbol{r}, \tau) \exp\left[i\omega\tau\right] \;\mathrm{d}\tau \;\mathrm{d}^n\boldsymbol{x}_1 \;\mathrm{d}^n\boldsymbol{r}. \tag{172}$$

Next, the right-hand side of Eq. (169) for $F(\boldsymbol{x}_1, \boldsymbol{r}, \tau)$ is substituted and the ansatz introduced by Morris and Boluriaan (2004) is applied to approximately express the Green's function at position $\boldsymbol{x}_2$ through its value at position $\boldsymbol{x}_1$,

$$\hat{p}_a(\boldsymbol{x}_2, \boldsymbol{x}, \omega) = \hat{p}_a(\boldsymbol{x}_1, \boldsymbol{x}, \omega) \exp\left[-i\frac{\omega\boldsymbol{x}\cdot\boldsymbol{r}}{c_0|\boldsymbol{x}|}\right]. \tag{173}$$

This is effectively a far-field approximation, taking into account only the phase difference due to a shift of the source coordinates.[5] Then the far-field spectrum becomes

$$\begin{aligned} \hat{S}(\boldsymbol{x}, \omega) \;\; &= \;\; \frac{1}{2\pi} \iint_{V_s} \int_{-\infty}^{\infty} \iint_{-\infty}^{\infty} |\hat{p}_a(\boldsymbol{x}_1, \boldsymbol{x}, \omega)|^2 \; \hat{H}(\boldsymbol{x}_1, \boldsymbol{\alpha}, \omega^*) \\ &\quad \times \exp\left[i(\omega - \omega^*)\tau\right] \exp\left[i\left(\boldsymbol{\alpha} - \frac{\omega\boldsymbol{x}}{c_0|\boldsymbol{x}|}\right)\boldsymbol{r}\right] \;\mathrm{d}\tau \;\mathrm{d}\omega^* \mathrm{d}\boldsymbol{r} \;\mathrm{d}^{\mathrm{n}}\boldsymbol{\alpha} \mathrm{d}^n\boldsymbol{x}_1. \end{aligned} \tag{174}$$

Integrations with respect to $\tau$ and $\boldsymbol{r}$ yield $2\pi\delta(\omega - \omega^*)$ and $(2\pi)^n\delta(\boldsymbol{\alpha} - \omega\boldsymbol{x}/c_0|\boldsymbol{x}|)$, respectively. Subsequently the integration with respect to $\omega^*$ and $\alpha$ can be performed, which yields

$$\hat{S}(\boldsymbol{x}, \omega) = (2\pi)^n \int_{V_s} |\hat{p}_a(\boldsymbol{x}_1, \boldsymbol{x}, \omega)|^2 \; \hat{H}\left(\boldsymbol{x}_1, \frac{\omega\boldsymbol{x}}{c_0|\boldsymbol{x}|}, \omega\right) \mathrm{d}\boldsymbol{x}_1 \tag{175}$$

This result corresponds to Eq. (17) in Morris and Boluriaan (2004).

The wavenumber-frequency spectrum is determined by

$$\hat{H}(\boldsymbol{x}_1, \boldsymbol{\alpha}, \omega) = \frac{1}{(2\pi)^n} \iint_{-\infty}^{\infty} \hat{R} \; \exp\left[-\frac{|\tau|}{\tau_s} - \frac{\ln(2)}{l_s^2}\left((r_1 - \bar{u}\tau)^2 + r_2^2 + r_3^2\right)\right] \exp\left[i(\omega\tau - \boldsymbol{\alpha}\boldsymbol{r})\right] \mathrm{d}\tau \mathrm{d}^{\mathrm{n}}\boldsymbol{r}. \tag{176}$$

Integration with respect to $\boldsymbol{r}$ and $\tau$ yields

$$\hat{H}(\boldsymbol{x}_1, \boldsymbol{\alpha}, \omega) = \frac{2}{(2\pi)^n} \left(\frac{\pi}{\ln(2)}\right)^{\frac{3}{2}} \hat{R}\tau_s \; \frac{\exp\left[-\frac{l_s^2|\boldsymbol{\alpha}|^2}{4\ln(2)}\right]}{1 + \omega^2\tau_s^2\left(1 - \alpha_1\frac{\bar{u}}{\omega}\right)^2} \tag{177}$$

[5] A minor difference occurs here to the approximative phase difference used by Tam Auriault, since they use $\omega x_1 \boldsymbol{e}_1/c_0|\boldsymbol{x}|$ instead of $\omega\boldsymbol{x}/c_0|\boldsymbol{x}|$., where $\boldsymbol{e}_1$ indicates the main jet convection direction.

The acoustic spectrum can be deduced from Eq. (175) using Eq. (177) with $\boldsymbol{\alpha} = \omega\boldsymbol{x}/c_0|\boldsymbol{x}|$, $|\boldsymbol{\alpha}| = \omega/c_0$, and $\alpha_1 = \omega/c_0\cos\theta$, where $\theta$ indicates the angle between the source-oberver vector and the $x$-axis. This yields

$$\hat{S}(\boldsymbol{x},\omega) = 2\left(\frac{\pi}{\ln(2)}\right)^{\frac{3}{2}}\int_{V_s}\hat{R}\tau_s l_s^3\,|\hat{p}_a(\boldsymbol{x}_1,\boldsymbol{x},\omega)|^2\,\frac{\exp\left[-\frac{\omega^2 l_s^2}{4\ln(2)c_0^2}\right]}{1+\omega^2\tau_s^2\left(1-M_0\cos\theta\right)^2}\mathrm{d}^n\boldsymbol{x}_1, \tag{178}$$

which agrees with the spectrum given by Morris and Boluriaan (2004). This result gives the far-field spectrum as an integral over the sources, i.e. the product of the squared Green function weighted with an effective sources variance times an $\omega$ dependent part, which is associated to the elementary sound spectrum radiated by each infinitesimal source volume. Note, the effective source variance is given by the factor $\hat{R}\tau_s l_s^3$, which indicates a dependence on the correlation volume $l_s^3$, refer to the discussion in the Introduction.

### A.2.2 Far-field spectrum 2-D

If the sound generation process is studied in 2-D based on a 2-D cross-correlation model

$$\langle q_s(\boldsymbol{x}_1,t_1)q_s(\boldsymbol{x}_1+\boldsymbol{r},t_1+\tau)\rangle = \hat{R}\times\exp\left\{-\frac{|\tau|}{\tau_s}-\frac{\ln(2)}{l_s^2}\left[(r_1-\bar{u}\tau)^2+r_2^2\right]\right\} \tag{179}$$

the wavenumber-frequency spectrum is determined from

$$\hat{H}(\boldsymbol{x}_1,\boldsymbol{\alpha},\omega) = \frac{1}{(2\pi)^2}\iint_{-\infty}^{\infty}\hat{R}\exp\left[-\frac{|\tau|}{\tau_s}-\frac{\ln(2)}{l_s^2}\left((r_1-\bar{u}\tau)^2+r_2^2\right)\right]\exp\left[i(\omega\tau-\boldsymbol{\alpha}\boldsymbol{r})\right]\mathrm{d}\tau\mathrm{d}^2\boldsymbol{r} \tag{180}$$

with $\boldsymbol{\alpha}\boldsymbol{r} = \alpha_1 r_1 + \alpha_2 r_2$. As a slight modification to the 3-D result derived previously, the 2-D wavenumber-frequency spectrum becomes

$$\hat{H}(\boldsymbol{x}_1,\boldsymbol{\alpha},\omega) = \frac{2}{(2\pi)^2}\frac{\pi}{\ln(2)}\hat{R}\tau_s l_s^2\,\frac{\exp\left[-\frac{l_s^2|\boldsymbol{\alpha}|^2}{4\ln(2)}\right]}{1+\omega^2\tau_s^2\left(1-\alpha_1\frac{\bar{u}}{\omega}\right)^2}. \tag{181}$$

The acoustic spectrum can be deduced from Eq. (181) using $\boldsymbol{\alpha} = \omega/c_0\left(\cos\theta,\sin\theta\right)^T$, refer to discussion in the footnote above. This yields

$$\hat{S}(\boldsymbol{x},\omega) = 2\left(\frac{\pi}{\ln(2)}\right)\int_{V_s}\hat{R}\tau_s l_s^2\,|\hat{p}_a(\boldsymbol{x}_1,\boldsymbol{x},\omega)|^2\,\frac{\exp\left[-\frac{\omega^2 l_s^2}{4\ln(2)c_0^2}\right]}{1+\omega^2\tau_s^2\left(1-M_0\cos\theta\right)^2}\mathrm{d}^2\boldsymbol{x}_1. \tag{182}$$

Compared to the definition of the 3-D spectrum, this result is reduced by a factor

$$\sqrt{\frac{\pi}{\ln(2)}}l_s.$$

### A.2.3 Green's function 2-D

For sound propagation in 2-D the LEE become for a medium at rest and a source term $q_s$ on the right-hand side of the pressure equation

$$\frac{\partial\boldsymbol{u}'}{\partial t}+\frac{1}{\rho_0}\boldsymbol{\nabla}p' = 0 \tag{183}$$

$$\frac{\partial p'}{\partial t}+\gamma p_0\boldsymbol{\nabla}\cdot\boldsymbol{u}' = q_s. \tag{184}$$

For our test problem the cross-correlation of the right-hand side source term is given by Eq. (179). Note, for the considered test problem the source term still includes a source convection velocity $\bar{u} \neq 0$, while in the acoustic progagation part no mean-flow is considered to simplify the derivation of an analytical expression for the radiated spectrum.

With $c_0^2 := \gamma p_0/\rho_0$ the propagation model can be recast into the simple wave equation

$$\frac{1}{c_0^2}\frac{\partial^2 p'}{\partial t^2} - \boldsymbol{\nabla}^2 p' = \frac{1}{c_0^2}\frac{\partial q_s}{\partial t}. \tag{185}$$

Fourier transformation in time, with convention

$$\hat{p}(\boldsymbol{x},\omega) = \int_{-\infty}^{\infty} p(\boldsymbol{x},t)e^{i\omega t}\mathrm{d}t \qquad\qquad p(\boldsymbol{x},t) = \frac{1}{2\pi}\int_{-\infty}^{\infty} \hat{p}(\boldsymbol{x},\omega)e^{-i\omega t}d\omega, \tag{186}$$

yields the Helmholtz equation

$$\left(k^2 + \boldsymbol{\nabla}^2\right)\hat{p}'(\boldsymbol{x},\omega) = \frac{ik}{c_0}\hat{q}_s(\boldsymbol{x},\omega), \tag{187}$$

where $k = \omega/c_0$. The Green's function of the 2-D Helmholtz equation, which satisfies

$$\left(k^2 + \boldsymbol{\nabla}^2\right)\hat{G}(\boldsymbol{x}-\boldsymbol{x}_1,k) = \delta(\boldsymbol{x}-\boldsymbol{x}_1), \tag{188}$$

is

$$\hat{G}(\boldsymbol{x}-\boldsymbol{x}_1,k) = \frac{i}{4}H_0^{(1)}(k|\boldsymbol{x}-\boldsymbol{x}_1|). \tag{189}$$

With this the Fourier transform of fluctuating pressure becomes

$$\hat{p}'(\boldsymbol{x},\omega) = \int -\frac{k}{4c_0}H_0^{(1)}(k|\boldsymbol{x}-\boldsymbol{x}_1|)\hat{q}_s(\boldsymbol{x}_1,\omega)\mathrm{d}^2\boldsymbol{x}_1, \tag{190}$$

and its back-transformation into time reads

$$p'(\boldsymbol{x},t) = \frac{1}{2\pi}\int\int -\frac{k}{4c_0}H_0^{(1)}(k|\boldsymbol{x}-\boldsymbol{x}_1|)\hat{q}_s(\boldsymbol{x}_1,\omega)\exp\left(-i\omega t\right)\mathrm{d}^2\boldsymbol{x}_1\mathrm{d}\omega. \tag{191}$$

From Eq. (191) the Green's function for the 2-D case without flow infers as

$$\hat{p}_a(\boldsymbol{x}_1,\boldsymbol{x},\omega) = -\frac{\omega}{4c_0^2}H_0^{(1)}\left(\frac{\omega}{c_0}\left|\boldsymbol{x}-\boldsymbol{x}_1\right|\right). \tag{192}$$

Consequently,

$$\left|\hat{p}_a(\boldsymbol{x}_1,\boldsymbol{x},\omega)\right|^2 = \frac{\omega^2}{16c_0^4}\left[J_0^2\left(\frac{\omega}{c_0}\left|\boldsymbol{x}-\boldsymbol{x}_1\right|\right) + Y_0^2\left(\frac{\omega}{c_0}\left|\boldsymbol{x}-\boldsymbol{x}_1\right|\right)\right]. \tag{193}$$

Asymptotically this result becomes

$$\left|\hat{p}_a(\boldsymbol{x}_1,\boldsymbol{x},\omega)\right|^2 = \frac{\omega}{8\pi c_0^3|\boldsymbol{x}-\boldsymbol{x}_1|}. \tag{194}$$